Application of optimisation methods for quantum sensors and gravity surveys

Claudia Petrucci

Thesis submitted to the University of Nottingham
for the degree of Master of Philosophy, August 2017

Abstract

The aim of this study is the use of optimisation methods both for the design of the components of quantum gravity sensors and for the investigation of optimum gravity surveys to collect data for geophysical exploration. The first part of the thesis is focused on the optimisation of a gravity survey. An optimised acquisition scheme is designed using the content coming from the horizontal gravity gradients. The data acquired with this "optimised grid" and with a regular grid are inverted and the performances of the different schemes are analysed through the comparison of their model resolution matrices. It is proved that the"optimised grid" allows a higher resolution than the regular grid in the proximity of the gravity anomaly to detect. The second part of the thesis is dedicated to the design of a magnetic trap with Comsol Multiphysics software and to the numerical modeling of a magneto-optical trap. The parameters used to design the magnetic trap are inferred from an optimisation method specifically conceived to miniaturise the dimensions and diminish the power consumption of the device. The Comsol Multiphysics software is used to verify the magnetic field, the heating, stress, strain and temperature produced by such a device. Moreover, in order to integrate the magnetic trap with optical access to build an optimum Magneto-Optical Trap (MOT), a numerical model of a 3D MOT that takes into account realistic effects (e.g. multiple level of atoms, Gaussian profile of the beams) is tested. This represents the initial step of an optimisation method that could allow the realisation of optimum MOTs.

Acknowledgements

I would first like to thank my supervisor at the University of Nottingham Prof. Mark Fromhold, and my supervisors at the British Geological Survey Dr. Paul Wilkinson and Dr. Oliver Kuras who have supported, mentored and guided me throughout these years.
I would also like to thank the Geo Energy Research Centre (GERC) for giving me the opportunity to have this experience and the RSK for showing interest in my research.
Special thanks go to Dr. Nathan Welch for all the inspring discussions and clarifications, and to my colleagues, both at the UoN and the BGS: Chris, Rosy, Michael, Yijia, Jorge, Luke and Mihai for always providing chats and reassurances. Further thanks go to Cornelia who discussed with me about gravity and hosted me in Nottingham when I needed.
Finally, a very special thank to my family, the ones I have near me and the ones that, despite being far, always succeed in understanding and supporting me.

Contents

Introduction

The recent great advances in the field of cold matter have made possible the production of new gravity sensors based on quantum interference of cold atoms. These sensors promise higher sensitivity than the classical gravity instruments and unprecedented stability. Despite the recent efforts to make these instruments small enough to be portable and usable on the field (especially for Geophysical exploration), there is the need to further miniaturise these sensors. Optimisation methods can be really helpful both for the design of the components of the sensor and for the study of optimum gravity surveys that lead to the collection of data with high information content. This study focus on these two different aspects and, the thesis is organised in the following way:

the first three chapters describe the work done on the optimisation of a gravity survey, in particular

- In Chapter 1 a description of the gravity field is presented and how this is measured and processed. Therefore, after a section on the Newton potential theory, there follow sections on the gravity instruments historically used and on the corrections to perform in order to obtain a residual gravity field.
- In Chapter 2 the basic notions of the inverse problems are described together with a focus on the Tikhonov regularisation method and the definition of the model resolution matrix. These last two concepts are specifically related to the work done on the optimisation of a gravity survey and presented in the Chapter 3.
- In Chapter 3 the work done on the optimisation of a gravity survey is presented. In particular it is described how an alternate grid scheme can be designed, how the inversion of the gravity data has been performed through the GRAV3D software and how the model resolution matrix can be used to appraise the different grid schemes. Moreover, the results obtained with this study and the possible future applications are shown.

The last three chapters describe the work done on the miniaturisation of components of a quantum sensor, in particular

- In Chapter 4 the theory beneath the working principle of a magnetic trap is presented together with some examples of common magnetic trap configurations. Also, in order to understand how a magneto-optical trap works, it is described what happens to an atom when it interacts with lasers. This chapter includes all the theory necessary in order to understand the work done in Chapter 5 and Chapter 6.

- In Chapter 5 the work done on the design of a magnetic trap with the Comsol Multiphysics software is described. The Chapter describes how the geometric parameters used to build the device are inferred by an optimisation method, and then it focuses on the results obtained in terms of magnetic field profile, heating, stress, strain and temperature produced by the device.

- In Chapter 6 it is presented how a realistic magneto-optical trap can be modelled if the atoms are subject to a more complicated expression of the force.This Chapter lays the foundation for an optimisation method to be implemented in the MOT.

Chapter 1

Gravity theory

The gravity method is an established geophysical technique that is used to characterize density variations in the crust and upper mantle, traditionally, through the measurement of the vertical component of the gravitational attraction g_z.

This method can be used to detect a wide range of gravity anomalies at different distances from the surface, from deep tectonic structures for regional studies to shallow buried bodies or voids of interest in urban engineering. At an intermediate distance, it is possible to detect sedimentary basins, rifts, faults and other interesting geological structures. Therefore, the accuracy required for the survey is evidently determined by the object to detect and it is dependent not only on the precision of the gravity reading, but also on the acccuracy with which the location and the height of the measurement position are recorded. For example, in mineral prospecting, an anomaly of 10μGal (1Gal = 1cms^{-2}) can indicate the presence of an ore body of interest, thus an accuracy of 5μGal is required [1]. This accuracy needs to be further increased in urban engineering gravity surveys, which are becoming, in recent years, extremely detailed and of interest for the detection of small conduits or pipelines. To give an idea, current gravimetric instruments are able to detect bodies of a diameter to depth ratio of approximately unity, while the recent interest is in increasing the sensitivity of these instruments and decreasing the ratio to less than unity [2]. This is the reason for the recent drive to the development of portable quantum gravity sensors based on atom interferometry (described in the following sections) that are characterised by a greater accuracy and could represent good candidates for the new generation of extremely precise gravity gravimeters and gradiometers.

Together with the data acquisition, it is necessary to discuss the inevitable initial step in the analysis of gravity data: the separation of the field caused by the object to detect (residual field) from the field produced by the surrounding geological environment or other sources.

Therefore, in order to understand the nature of the gravity field and how this is measured and processed, the following sections present a description of the Newtonian potential theory [3], the gravity instruments that have historically been developed [4, 5] and the necessary corrections to obtain a residual gravity field [3].

1.1 Gravitational potential

Our understanding of the force of gravity began in 1687 with the publication of the Newton's *Philosophiae Principia Mathematica* and the law of universal gravitation

$$F = \gamma \frac{Mm}{r^2}, \tag{1.1}$$

which, in Cartesian coordinates, represents the mutual force between a mass M centered at a point $Q = (x_0, y_0, z_0)$ and a mass m centered at a point $P = (x, y, z)$ at a distance $r = \sqrt{(x - x_0)^2 + (y - y_0)^2 + (z - z_0)^2}$ and where $\gamma = 6.67{\times}10^{-11}\mathrm{m}^3\mathrm{kg}^{-1}\mathrm{s}^{-2}$ is Newton's gravitational constant. If m is considered to be a test mass with unit magnitude, then, dividing the gravity force by the test mass, it is possible to obtain the gravitational field

$$\mathbf{g} = \gamma \frac{M}{r^2}\ \hat{\mathbf{r}}. \tag{1.2}$$

The gravitational field is measured in ms^{-2} in SI units and in Gal (or mGal) in the cgs system. Since the gravitational field is conservative, it can be espressed as the gradient of a scalar potential

$$\mathbf{g} = -\nabla U. \tag{1.3}$$

The function U is known as gravitational potential and $U = -\gamma \frac{M}{r}$. The gravitational potential follows the principle of superposition, which states that the total potential of a collection of masses can be expressed as the sum of the gravitational potentials of the singular masses. This principle is extremely useful when one wants to find the gravitational attraction of a continuous distribution of matter; in the limit of infinitesimally small masses dm the summation becomes an integral and the superposition principal can be expressed as

$$U = -\gamma \int_V \frac{dm}{r}\ , \tag{1.4}$$

where the integration is performed over the volume V occupied by the mass distribution. If the infinitesimal masses are expressed as $dm = \rho(x, y, z)dv$, where $\rho(x, y, z)$ is the local mass density, substituting this in the previous equation leads to

$$U = -\gamma \int_V \frac{\rho(x, y, z)}{r} dv\ . \tag{1.5}$$

Partial differentiation of the integral with respect to x, y and z gives the gravitational field as described in equation 1.3. Since in this work only the vertical component of the gravity field will be used, the partial derivative of U with respect to z, for an observation point outside the distribution of mass, is specifically stated:

$$g_z = -\frac{\partial U}{\partial z} = \gamma \int_V \frac{(z - z_0)}{r^3} \rho(x, y, z) dv\ . \tag{1.6}$$

Although it is theoretically possible to measure the components g_x and g_y, this is usually a complicated task, given the fact that these are much smaller than the g_z component, and, for this reason, not routinely performed. Moreover, if Gauss' s law is applied to the gravity field, it is possible to prove that the vertical component of gravity, once integrated over an infinite plane, is proportional to the whole anomaly

mass buried below the plane [3]. Therefore, the vertical component is sufficient if the gravity survey is conducted on an area that can be approximately taken to be infinite (that means that the limits of the survey area needs to be set beyond the localised anomaly mass of interest).

The second order derivatives can be derived in a similar way again for the x, y and z components. It is simple to prove that adding the three components of the second order derivatives yields

$$\nabla^2 U = \frac{\partial^2 U}{\partial x^2} + \frac{\partial^2 U}{\partial y^2} + \frac{\partial^2 U}{\partial z^2} = 0, \tag{1.7}$$

this relation is known as Laplace's equation and shows that, at all the points located outside the distribution of mass, the gravitational potential is harmonic.

The Laplace equation is extremely important in this case because it shows the inherent source of non-uniqueness of the gravitational field. In fact, on the basis of Green's third identity it is possible to prove that there are infinitely many surface density distributions with the same gravitational potential as a given three-dimensional density distribution (this is the Green's equivalent layer theorem, which demonstrates that there is no depth-to-source information inherent in the gravitational field).

This lack of information can't be resolved mathematically and it is addressed in different ways depending on the particular route of interpretation chosen and the inversion performed. The approach used in this work will be specifically presented in the following chapters.

1.2 Gravity instruments

Since the gravity method is a relatively old technique in geophysical exploration, different gravity instruments have been proposed and manufactured over the years, tailored to the dimensions of the mass to detect and to the particular environment of the survey (land, marine, borehole, airborne surveys).

All the gravity sensors used so far fall into two main categories: absolute gravimeters or relative gravimeters. As the names may suggest, an absolute gravimeter measures the local value of gravity at a specific location, while a relative one measures the difference in gravity values between two locations. A subcategory of gravity sensors are gravity gradiometers that measure the horizontal and vertical gravity gradients. This can be derived from the value of gravity at two points separated by a small horizontal or vertical distance.

Among the numerous designs proposed over the years (both for absolute and relative sensors), four general types of classical gravimeter and gravity gradiometer have been extensively used in the context of land geophysical exploration. These include the pendulum, the torsion-balance gravity gradiometer, the spring gravimeter and the free-fall gravimeter.

1.2.1 Pendulum

Galileo Galilei was the first to study the properties of a pendulum at the beginning of the 17th century discovering the isochronism and the independence of the period of the pendulum from the mass of the bob.

These discoveries were used by Christian Huygens who developed, in 1656, the first pendulum clock showing that it could also be used, as an absolute instrument, to measure the absolute value of gravity, g [6]. In order to be used as an absolute gravimeter, however, it was necessary to know with the same precision the length L of the pendulum, the moment of inertia I and the period T of the oscillation.

Since, at that time, it was impossible to know either I or L with great precision, the pendulum was mostly used as relative gravimeter throughout the 18th and 19th centuries.

The difficulties of measuring the pendulum length L and I were overcome in 1817 with the invention of the reversible pendulum by Henry Kater that was able to reach a precision of about 10 mgal ($10^{-4}\frac{m}{s^2}$) on absolute gravity measurements [7]. This is because, thanks to the reversible pendulum, the measure of g became limited to the measurements of intervals of time and equivalent lengths. By the end of the century, after substantial improvements, the pendulum reached a precision of 1 mgal ($10^{-5}\frac{m}{s^2}$) [4].

1.2.2 Torsion-balance gravity gradiometer

Gravity gradiometers have been used extensively in recent decades in airborne and ship-based surveys, but, the ability to measure gravity gradients has been possible since the construction of the torsion balance developed by Baron Roland von Eotvos in the late 1890s. In fact, experiments with torsion balances date back to the late 1700s with Henry Cavendish. It was only in 1896 that Eotvos succeeded in building a working torsion balance. This device was extensively used in the early 1900s in the oil and gas exploration given its great accuracy (a few Eotvos units, $1E = 10^{-9}\mathrm{s}^{-2}$) and became out-of-date when the first spring gravimeters were produced.

1.2.3 Spring gravimeters

Spring gravimeters are relative sensors that measure the change in the gravity field between two different stations by means of the change of the force on a proof mass attached to a spring. The measurements can be usually performed in different ways: measuring the magnitude of a restoring force, measuring the change of the equilibrium position or measuring the change in the force necessary to maintain the equilibrium position.

Although John Ershel suggested using a spring balance to measure gravity in 1833, the underlying theory had been known since the formulation of the law of elasticity by Robert Hooke in 1678. But it was only in the 1930s that the growing interest in the oil exploration and in the production of materials led to the production of a functional spring gravimeter [4].

Currently the LaCoste & Romberg (L & R) G-meters, the Worden meter and the Scintrex meter are the most widely used gravimeters. For instance, the L&R gravimeters can reach an accuracy of $1 - 5\mu$Gal in the field if care is taken to not change the range and the system is corrected for changes in temperature and pressure, the drift of the sensor and vibration [4].

1.2.4 Free fall gravimeters

The absolute value of gravity can be measured directly by noting the times it takes for an object to fall a given distance. As found by Galileo, the distance of the fall of any object, initially at rest, is proportional to the square of the time required for its fall with the proportionality constant being the acceleration of gravity g. Although this seems conceptually the easiest way to perform an absolute gravity measurement, it requires a short time period to be measured with great precision. The accuracy needed was achieved only with the use of the quartz clock, introduced in the 1950s [4].

The first free fall gravimeters had a resolution greater than 1 mGal and used, together with the above mentioned quartz clock, a white-light Michelson interferometer, a 1 m-long rod made of quartz, steel, or invar as falling body, and a photographic system to record the falls. The sensitivity was further improved in 1963 with the use of a corner-cube mirror as falling body, a laser interferometer and an atomic clock. In this prototype, the reference was represented by a fixed second corner cube. With these further improvements these devices reached precisions from 0.01 to 0.05 mGal in the 1970s, eventually replacing pendulums for the measurements of absolute gravity [4]. Despite, over time, the reduction in the falling distance (currently about 20 cm) and increase in the number of possible drops, free-fall gravimeters are still very large, slow and expensive. For instance, the FG5 gravimeter produced by Micro-g Solutions Inc., and having a resolution of about 1 μGal, has a total shipping weight of 150 kg and a total volume of 1.5m^3 [8]. In recent years a new kind of free fall gravimeter, based on atom interferometry, has been proposed (and tested) to reach further sensitivity in the measurements. In classical gravimeters the mass used is a macroscopic object that is read out optically, whereas, in atom interferometers the test mass is replaced by a cloud of cooled atoms whose change in position is monitored by their interaction with a stationary Raman laser waves[9].

Quantum gravimeters

The quantum gravimeter is the latest and most sensitive kind of free fall gravimeters ever tested [9]. These gravimeters are based on the characteristics of atomic (or matter-wave) interferometers, which were first realized and demonstrated at Stanford University in 1991, to be sensitive to the Earth's gravity field [10]. The current schemes use atoms in an atomic fountain configuration and stimulated Raman transitions between hyperfine ground states to implement beam splitters and mirrors. Depending on the different sequences of Raman pulse used, cold atom interferometers fall in two main categories : Ramsey-Borde (R-B) interferometers and Mach-Zender (M-Z) interferometers. The latter scheme, which optically consists of a

pair of beam splitters and mirrors to guide the light, is extensively used in metrology and its matter-wave analogue is based on a $\frac{\pi}{2}$-π-$\frac{\pi}{2}$ Raman pulse sequence.

In the Raman process, an atom with two hyperfine ground states 1> and 2> is irradiated by the light coming from two counter propagating laser beams whose frequency difference $\omega_1 - \omega_2$ is nearly equal to the frequency of the $1> \rightarrow 2>$ transition. Therefore, an atom that undergoes a stimulated Raman transition, absorbs a photon of frequency ω_1 and emits another photon of frequency ω_2 [11, 12]. Because both photons carry momentum and because of the law of conservation of the total momentum, the atom receives a recoil momentum kick equal to $\mathbf{p} = \hbar(\mathbf{k}_1 - \mathbf{k}_2)$ and at the same time change its internal state [9, 13].

Figure 1.1 shows how such a $\frac{\pi}{2}$- π-$\frac{\pi}{2}$ Raman pulse sequence is applied for splitting, reflecting, and recombining an atom and changing its internal state. At the end of the sequence the fraction of atoms in one of the states is measured, which results in a total phase difference between the two paths.

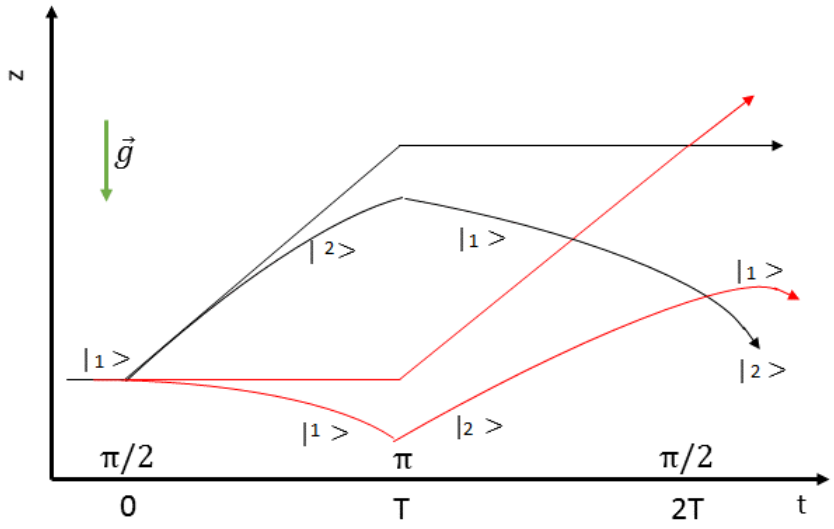

Figure 1.1: Mach Zender scheme (the straight lines represents the trajectories in the absence of gravity, while the curves represents the trajectories in the presence of gravity). Modified from [9].

The phase shift given by the gravitational acceleration is

$$\Delta\phi = k_{eff} g T^2, \tag{1.8}$$

where $k_{eff} = k_1 - k_2$ is the effective wave number of the two counter propagating laser beams the atom is illuminated by, while T is the interrogation time. By varying and increasing the interrogation time it is possible to determine the fringe spacing and calculate gravity.

These kinds of instruments are usually set up in an atomic fountain configuration composed of a magneto optical trap for the trapping and the cooling of the atoms that are susequently launched, and a laser system to generate the Raman pulses and implement the interferometry. The precision of such atomic gravimeters has reached 3μGal with 60 s of interrogation time or 0.1μGal with 2 days of interrogation time

[13]. If two identical atom interferometers are placed one above the other, the vertical gravity gradient can be measured and a quantum gravity gradiometer can be realized.

1.3 Gravity corrections

Once the measurements have been collected, the observed gravity value in one location will be the mutual effect of the density variations in the crust or upple mantle and the field produced by other effects:

$$g_{obs} = g_0 + g_{FA} + g_{Bouguer} + g_{Terrain} + g_{tidal} + g_{Eotvos} + g_{anomaly}, \tag{1.9}$$

where g_0 represents the attraction of the reference ellipsoid, g_{FA} is known as free air correction, g_{tidal} is the tidal variation, $g_{Eotovos}$ is the contribution given by the Eotvos effect and $g_{Bouguer}$ and $g_{Terrain}$ take into account the effect of the masses above the sea level. Since the final objective of a gravity survey for geophysical exploration is to characterize the density variations given by anomalous bodies in the crust or upple mantle, a series of corrections need to be performed to isolate the anomalous field $g_{anomaly}$ from all the other terms.

It is important to theoretically treat the corrections, since the grid optimisation method of gravity surveys presented in this work in Chapter 3 is assuming that observed gravity values have already been corrected and, therefore, they represent only the density variations given by the anomalous mass. Only the corrections related to the contributions of other gravity fields are treated, while the possible corrections related to the instrumentation are not taken into account.

1.3.1 Attraction of the "Normal" Earth

The first term to subtract from the observed gravity measurement is the attraction given by the Earth.

It has been previously stated that the gravity acceleration can be expressed as the gradient of a scalar potential known as the Gravitational potential. The gravitational equipotential surface is called the *geoid* and corresponds to the sea level surface when the effects of currents, tides and weather are neglected. Because the geoid follows the irregularities of the crust, it is not possible to represent it with a mathematical equation. Therefore, by international agreement, the geoid is approximated by an ellipsoid called the *reference ellipsoid*, which can be described by the equatorial radius a and the polar radius c, or by the flattening parameter $f = \frac{a-c}{c}$ alone. Moreover, the resultant gravity force has two components: the gravitational attraction and the centrifugal force related to the earth's rotation. Therefore, the value internationally accepted for the *theoretical gravity* or *"normal" gravity* on the reference ellipsoid is

$$g_0 = 9.7803267714 \frac{1 + 0.00193185138639 \sin^2 \lambda}{\sqrt{1 - 0.00669437999013 \sin^2 \lambda}}, \tag{1.10}$$

where λ is the latitude of the specific location considered. Details of how to derive this term can be found in [3].

Despite the actual difference between the geoid and the reference ellipsoid, the dissimilarities are usually ignored and g_0 is referred to as the theoretical gravity on the geoid.

1.3.2 Free-Air Correction

Most gravity surveys are conducted above or below the sea level and this effect needs to be considered and corrected, since all the measurements need to be referred to the geoid. The free air correction, if the observation point is at height h above the geoid, is given by

$$g_{FA} = -0.3086 \times 10^{-5} h. \tag{1.11}$$

This correction is intrinsecally negative and it is valid only in the case where there are no masses between the geoid and the observation point, otherwise the terms related to the Bouguer correction and the terrain correction also need to be subtracted.

1.3.3 Bouguer correction and terrain correction

In the case where there are additional masses between the point on the geoid and the observation point, the mass can be approximated by an infinite slab of thickness equal to h (height of the observation point above sea level). The attraction of an infinite slab can be calculated and is given by

$$g_{Bouguer} = 2\pi\gamma\rho h, \tag{1.12}$$

with γ the gravitational constant, and ρ the density of the slab. If the slab corresponds with the crust, the typical value of 2670kg/m^3 can be used and the Bouguer corrections becomes

$$g_{Bouguer} = 0.1119 \times 10^{-5} h. \tag{1.13}$$

It is usually unlikely that a gravity survey is conducted in a completely flat area that can be modelled by a slab. In presence of a more complicated topography, the terrain correction g_t needs to be subtracted as well.

In the past, the terrain correction was performed manually by the "Hammer method" in which the gravitational attractions of circular zones surrounding the observation point were estimated. Currently this is done through a digital model of the terrain. The terrain is then usually divided into volumes of prisms (or different shapes) for which the gravitational attraction is known [14].

The push to the development of more sensitive gravity sensors (such as the quantum gravimeter or the quantum gravity gradiometer) requires a more precise knowledge and modelling of the terrain, exactly because a more precise terrain correction term needs to be subtracted from the observed gravity [5].

1.3.4 Tidal correction

The earth-tides are caused by both the sun and the moon and they have an effect that can be detected by gravity instruments. Although this time-dependent and latitude-dependent effect is relatively small in respect to other corrections, it needs to be accounted for.

In high precision gravity surveys specific formulae for any location and time of day need to be used [15], while routinely, the tidal effect is assumed to be linear over periods of several hours. Because some gravity instruments present a linear drift in time during the survey, usually the two effects are corrected together.

1.3.5 Eotvos correction

When gravity surveys are not conducted on land but on moving platforms, such as ships or airplanes, the effect of the rotation of the earth needs to be considered. The angular velocity of an observer moving east during the survey, will be greater than the angular velocity experienced by an observer that remains stationary with respect to the rotation of the earth, and smaller for an observer moving west. Therefore, the apparent gravitational attraction is decreased or increased depending on the direction of the observer.

The Eotvos correction is dependent on the latitude λ and the velocity of the moving platform v taken in knots

$$g_{Eotvos} = 7.503v \cos\lambda \sin\alpha + 0.004154v^2. \tag{1.14}$$

This correction, if not accounted for, can be a limiting factor in the precision of shipborne and airborne surveys.

1.4 Summary

This chapter has described:

- The essential points of the theory of the gravity potential.
- The most important types of classical gravity sensors that have been used in gravity explorations, together with their sensitivities.
- The necessary corrections to perform on the measurements to isolate the residual field.

These elements are necessary for the interpretation of the gravity data, that, in this study is performed by inverting (i.e. fitting a model to) the data collected. In the following chapter there will be a focus on the concept of inherent non-uniqueness of the gravitational field which has consequences on the way the inversion is performed and the use of g_z as only component measured. It is also essential to understand the basic concepts on which different gravity instruments are built and the different

sensitivities they can reach, and what are the necessary corrections to perform once gravity data are collected. The last point has been exstensively discussed because all the interpretation methods (including the inversion presented in the next chapters) are performed on data that have already been corrected and represent only the residual gravity anomaly.

Chapter 2

Inversion theory

Once the gravity data have been collected and processed, isolating the residual field due to the anomalous mass, they need to be interpreted in order to obtain information about the gravity anomaly. Numerous interpretative approach are possible and have been developed over the years. They can be divided into three main categories: forward methods, inverse methods and data enhancement and display.

The forward methods require the construction of an initial source model through which the model's anomaly is calculated and compared with the observed anomaly, usually using gravity anomalies maps. The model parameters are adjusted in order to fit the observed anomaly by a process of trial and error usually left to the interpreter.

Inverse methods, on the other hand, allows the body parameters to be calculated directly from the observed anomaly. Some of these inverse methods aim to estimate the depth of the gravity source, assuming that the shape of the anomalous body is already known. For instance, the Euler Deconvolution method ([16], [17]) is based on Euler's homogeneity equation $\mathbf{r}\cdot\nabla g = -ng$, which relates different components of the gradient of the gravity field anomaly to the field itself multiplied by a structural index n which depends on the geometry of the source body. Selecting an appropriate n it is possible to solve for the body's position. In other inverse methods, instead, the 2D or 3D anomalous body can be divided into different cells of constant density and the inversion provides the value of density in each discretized cell.

The last category of data enhancement and display, instead, does not provide an estimation of model parameters, but it processes the anomaly to enhance some characteristics of the source. It is based on the Fourier analysis of gravity anomalies and the different content in the resulting frequencies. It is possible to apply different filters to attenuate several frequencies in order to diminish the noise on the data, or, also, to enhance anomalies caused by shallow sources (high- frequencies) at the expense of anomalies caused by deep sources (low-frequencies). Further details on these techinques can be found in [3].

The interpretation method used in this study is an inverse method based on the discretization of the anomaly into 3D cells each with constant density. Therefore in this chapter, the basic concepts of the inverse problem, intended as the process of obtaining from a set of measurements information about the source parameters, are discussed. Moreover, the inverse method applied to the gravity survey presented in

this work is based on the calculation of the resolution matrix, whose definition is strictly connected to the formulation of the specific inverse problem. For this reason particular relevance will be given to the Tikhonov regularization method (which is the regularization method used in this inversion) and to the concept of the resolution matrix of the model.

2.1 Inverse methods

If N measurements are taken in an experiment, they can be arranged as elements of a vector $\mathbf{d}$ of length N. Likewise, the model parameters can be represented by elements of a vector $\mathbf{m}$ of length M.

$$\mathbf{d} = [d_1, d_2, ..., d_N]^T, \tag{2.1}$$

$$\mathbf{m} = [m_1, m_2, ..., m_M]^T. \tag{2.2}$$

The basic idea of the inverse problem is that the data and the model parameters are related through a function G that incorporates the details of the survey design and the physical equations of the system

$$G(\mathbf{m}) = \mathbf{d}. \tag{2.3}$$

If the function G is linear, it can be expressed as a matrix equation

$$\mathbf{Gm} = \mathbf{d}, \tag{2.4}$$

where $\mathbf{G}$ is known as *data kernel* and, in most cases, can be an integral or a differential equation to be solved numerically.

The direct, or forward, problem consists of determining $\mathbf{d}$ knowing $\mathbf{m}$, while the inverse problem consists of obtaining the model parameters knowing the data. Since the gravity problem is a linear inverse problem, only the linear theory will be described. But, it is important to mention that, particularly in geophysics, it is typical to encounter non linear problems. They are usually solved by linearizing the equations and iterating the linear solution process.

2.1.1 Least squares solution

Obtaining an exact solution to an inverse problem is the final objective but is, in most cases, unrealistic, because such solution does not exist. This usually happens because of approximations in the numerical solutions of the physics of the problem or because of the presence of noise in the data. But, it is possible to find an approximate solution of the inverse problem by choosing a model $\mathbf{m}_{est}$ that minimizes some measure of the misfit between the observed data $\mathbf{d}_{obs}$ and the data predicted by $\mathbf{Gm}$.

The most common way of measuring this misfit is its L_2 norm

$$||\mathbf{Gm} - \mathbf{d}_{obs}||^2, \tag{2.5}$$

and the best model $\mathbf{m}_{est}$ that minimizes this norm is called the least square solution, which can be proved to be expressed as

$$\mathbf{m}_{est} = (\mathbf{G}^{\mathrm{T}}\mathbf{G})^{-1}\mathbf{G}^{\mathrm{T}}\mathbf{d}, \tag{2.6}$$

where T signifies transpose. This least squares approach is useful in overdetermined problems where there are more data than unknowns ($N > M$).

When the problem is underdetermined or, in other words, there are more unknowns than data ($N < M$) the formula expressed above for the least square solution fails. This happens because the concept of uniqueness fails: in fact, in such problems, there are an infinite number of solutions for which the misfit is sufficiently small. Therefore, the selection of a unique "best model" requires additional information. Moreover, as already explained in the Chapter 1, where the Laplace equation was presented, the gravity inverse problem is also inherently non-unique. Therefore, both of these sources of non-uniqueness need to be adressed.

Another typical characteristic of inverse problems is instability. This occurs when small variations in the measurements, for example when adding noise to the data, produces great changes in the estimated model. The inverse problems where this issue arises are called ill-conditioned. Inverse problems that are non-unique and unstable are ill-posed and a regularisation (in which additional information about the model is added) is required. This topic is illustrated in the next paragraph.

2.2 Tikhonov regularisation

For mixed- / under-determined inverse problems, the least squares solution does not provide enough information to obtain a unique estimated model. Further information, or apriori knowledge about the model, needs to be supplied in order to select only one of the infinite possibilities. The Tikhonov regularisation is one of the most used methods to regularise these kinds of ill-posed problems.

The basic idea of the Tikhonov regularisation is that, in case of multiple solutions, all those for which

$$||\mathbf{Gm} - \mathbf{d}_{obs}||^2 \leq \delta \tag{2.7}$$

can be selected and then the solution takes as the one having

$$min(||\mathbf{m}||^2). \tag{2.8}$$

In this way, the priori assumption added to regularize the problem, is that the solution is "simple" or, in other words, is small if measured under the L^2 norm. If the method of Lagrange multipliers is applied to this problem (further details on Lagrange multipliers can be found in [18]), the function to minimise is

$$\phi(\mathbf{m}) = ||\mathbf{Gm} - \mathbf{d}_{obs}||^2 + \beta||\mathbf{m}||^2, \tag{2.9}$$

which leads to the matrix equation

$$(\mathbf{G}^T\mathbf{G} + \beta\mathbf{I})\mathbf{m} = \mathbf{G}^T\mathbf{d}_{obs}, \tag{2.10}$$

from which the solution

$$\mathbf{m} = (\mathbf{G}^T\mathbf{G} + \beta\mathbf{I})^{-1}\mathbf{G}^T\mathbf{d}_{obs} \tag{2.11}$$

is obtained where β is a regularisation parameter.

To truly understand how the Tikhonov solution acts as a regularisation, it is useful to compare it with the solution obtained by singular value decomposition (SVD). The SVD method aims to solve the problem $\mathbf{Gm} = \mathbf{d}$ without regularisation. If the matrix $\mathbf{G}$, has dimensions $N \times M$ it can't be inverted, but it can always be decomposed into the product of three matrices:

$$\mathbf{G} = \mathbf{U}_p\mathbf{S}_p\mathbf{V}_p^T, \tag{2.12}$$

where $\mathbf{U}_p$ is an $N \times P$ matrix, $\mathbf{S}_p$ is a diagonal matrix having non zero positive elements in decreasing order $s_1 \geq s_2 \geq ... \geq s_p$ and $\mathbf{V}_p$ is an $M \times P$ matrix, P is the number of non-zero singular values s_i. With this decomposition the SVD solution of $\mathbf{Gm} = \mathbf{d}_{obs}$ is

$$\mathbf{m} = \mathbf{V}_p\mathbf{S}_p^{-1}\mathbf{U}^T\mathbf{d}_{obs}, \tag{2.13}$$

or in components

$$\mathbf{m} = \sum_{i=1}^{p} \frac{(u_i^T d_{obs})}{s_i} v_i. \tag{2.14}$$

Explaining why this pseudoinverse solution is mathematically acceptable is beyond the intention of this paragraph (a comprehensive dissertation can be found in [18]). Instead, we focus on the possible bias that can be introduced by such a solution. In fact if we consider realistic noise on the data

$$d_{obs} = d + \eta, \tag{2.15}$$

substituting this in equation 2.14 leads to

$$\mathbf{m} = \sum_{i=1}^{p} \frac{(u_i^T d)}{s_i} v_i + \sum_{i=1}^{p} \frac{(u_i^T \eta)}{s_i} v_i. \tag{2.16}$$

Therefore, even if the noise is small, the second term in equation 2.16 can be very large for small values of s_i. Thus small singular values can lead to great instability in the inverted model.

Instead, if the SVD decomposition of the matrix $\mathbf{G}$ is substituted in equation 2.11, the solution is

$$\mathbf{m} = (\mathbf{S}^2 + \beta\mathbf{I})^{-1}\mathbf{V}_p\mathbf{S}_p\mathbf{U}_p^T\mathbf{d}_{obs} = \mathbf{V}_p\mathbf{T}\mathbf{S}_p^{-1}\mathbf{U}^T\mathbf{d}_{obs}, \tag{2.17}$$

where the matrix $\mathbf{T}$ has components

$$t_i = \frac{s_i^2}{s_i^2 + \beta}. \tag{2.18}$$

From the above equation is possible to understand how the Tikhonov regularisation act as a filter. In fact for $s_i \gg \beta$, $t_i \approx 1$ while for $s_i \ll \beta$, $t_i \approx 0$ and t_i decreases when the singular values become smaller as is desirable for stability.

The Tikhonov regularisation can be implemented through the SVD decomposition when the dimension of the inverse problem to solve is small. In large-scale problems, such as the gravity problem discussed in the next chapter, the decomposition of the matrix is not possible and the matrix systems are solved using iterative techniques.

2.2.1 Choosing β

From the above considerations it is clear that choosing β is vital to achieve a reasonable inverse model. The two most popular techniques to do this are the Generalized Cross Validation (GCV) method and the L-curve method.

GCV method

The basic idea for the General Cross Validation method is that a good solution to the inverse problem is one that is not particularly sensitive to a specific datum; this leads to the concept of *leave-one-out*. In particular, a value of β is selected and a reduced data set $\mathbf{d}_{obs}^k$ is generated discarding a point k from the measurements. The inversion of this new dataset is performed by minimizing

$$\phi_k(\mathbf{m}) = ||\mathbf{G}\mathbf{m} - \mathbf{d}_{obs}^k||^2 + \beta||\mathbf{m}||^2. \tag{2.19}$$

Once the $\mathbf{m}_k(\beta)$ solution is obtained, the forward model is carried out to predict d_{pred}^k. The difference between the predicted and the observed datum is accumulated in a Cross Validation function (CV). If the procedure is repeated with the same β and for all the data points $k = 1...N$ it is possible to obtain

$$CV(\beta) = \sum_{k=1}^{N} (d_{pred}^k - d_{obs}^k)^2. \tag{2.20}$$

In order to build the CV as a function of β, the same sum of terms need to be computed for different values of β and the minimum of the CV function selects the best value of β to be used in the total inversion, where all the data are taken into account. This procedure is, in most cases, long and unfeasible. Instead it is possible to build a Generalized Cross Validation function (not to be confused with the General Cross Validation) where the function to minimise is:

$$GCV(\beta) = \frac{||\mathbf{d}(\beta) - \mathbf{d}_{obs}||^2}{(Tr(I - C(\beta)))^2}, \tag{2.21}$$

where $\mathbf{d}(\beta)$ is the predicted data obtained from inverting all the observation points from different values of β and $C(\beta) = \mathbf{G}(\mathbf{G}^T\mathbf{G} + \beta\mathbf{I})^{-1}\mathbf{G}^T$ [19]. Once this curve is plotted the β corresponding to the minimum of the curve is chosen as best regularization parameter.

L-curve method

When plotting in a log-log scale $||\mathbf{Gm} - \mathbf{d}||^2$ as a function of $||\mathbf{m}||^2$ for different value of β a typical L-curve is formed. This happens because $||\mathbf{Gm} - \mathbf{d}||^2$ increases with β (2.1), while $||\mathbf{m}||^2$ decreases as a function of β (2.2).

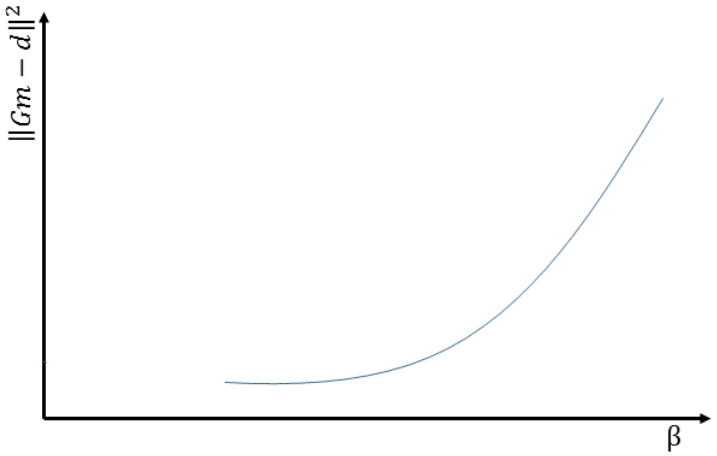

Figure 2.1: Schematic change of $||\mathbf{Gm} - \mathbf{d}||^2$ as a function of β

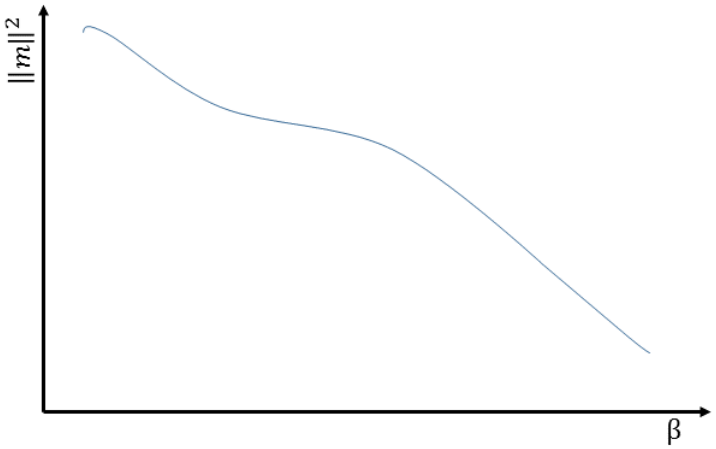

Figure 2.2: Schematic change of $||\mathbf{m}||^2$ as a function of β

The point of maximum curvature of L or "knee" of the curve is taken as the best value for β (2.3). In the inversion of gravity data presented in this work, where a Tikhonov regularisation is implemented, the L-curve method is used. In fact, while the GCV curve does not always present a definite minimum, the "knee" of the L-curve is easily identified.

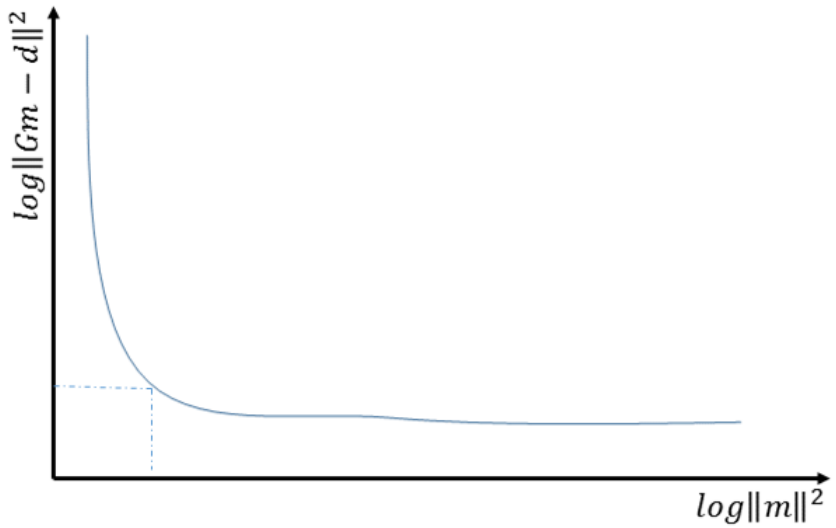

Figure 2.3: Schematic L-curve obtained via a log-log plot of $||\mathbf{Gm}-\mathbf{d}||^2$ as a function of $||\mathbf{m}||^2$. The dashed lines indicate the location of the best value for β.

2.3 Resolution matrix of the model

Once a generalised inverse $\mathbf{G}^{-g}$ has been found that solves the inverse problem $\mathbf{Gm} = \mathbf{d}$, it is interesting to characterize how well the model is resolved. In particular if there is a true, but unknown set of model parameters $\mathbf{m}_{true}$ that solves the problem

$$\mathbf{Gm}_{true} = \mathbf{d}_{obs}, \tag{2.22}$$

and an estimate of the model parameters given by the generalized inverse

$$\mathbf{m}_{est} = \mathbf{G}^{-g}\mathbf{d}_{obs}, \tag{2.23}$$

the interest is in determining how close $\mathbf{m}_{est}$ is to the true solution $\mathbf{m}_{true}$.

Substituting 2.22 in 2.23 yields

$$\mathbf{m}_{est} = \mathbf{G}^{-g}\mathbf{d}_{obs} = \mathbf{G}^{-g}[\mathbf{Gm}_{true}] = \mathbf{Rm}_{true}. \tag{2.24}$$

$\mathbf{R} = \mathbf{G}^{-g}\mathbf{G}$ is called the model resolution matrix and has some interesting characteristics.

The first immediate characteristic to notice is that, if the resolution matrix of the model is the identity matrix $\mathbf{R} = \mathbf{I}$, then each model parameter is perfectly resolved. The other interesting feature of the resolution matrix is that, by definition, it is a function of the only data kernel ($\mathbf{G}$) and the possible a priori information added to the problem. This means that the model resolution matrix does not depend on the particular model or the set of data collected but only on the survey design and the physics of the problem. Because of this, the study of the resolution matrix can be extremely useful in experimental design to determine an optimum way of collecting the measurements [20]. In this study, the examination of the model resolution matrix is intended to compare different proposed gravity surveys.

There are different ways of studying the model resolution matrix, one is examining the diagonal elements of the matrix and their deviation from the identity. Other possibilties are plotting the columns or the rows of the model resolution matrix.

There exists a conceptual difference between the columns and the rows of $\mathbf{R}$. If $\mathbf{R}$ is different from the identity matrix, the generic row i of the matrix represents the linear combination of the actual model parameters that forms the i_{th} estimated parameter. The rows of the model resolution matrix are usually referred to as the averaging function of Backus and Gilbert. The generic column k, on the other hand, represents how a delta function perturbation in the k_{th} parameter would propagate in the model. This is thie reason why the columns of the resolution matrix are named the point spread function (PSF) [21].

In the next Chapter, the concepts of Tikhonov regularisation and resolution matrix will be further extended and related to the specific study performed on the optimisation of the gravity survey.

Chapter 3

Study of the resolution matrix of optimised grids

As already mentioned, gravity surveys involve measuring the Earth's gravitational field on the Earth's surface. Sometimes, borehole gravity data can also be collected, but these measurements are expensive to perform. Data could also be collected at a range of heights above the surface, but since potential field continuation allows these to be calculated from the measured surface data, this is unnecessary in practice [3]. Therefore, gravity data are, usually, collected along bidimensional surface grids. The gravity measurements are usually taken on evenly spaced rectangular grids; this is an established standardized data-acquisition procedure and less attention has been paid to possible alternate acquisition schemes. In fact, despite survey design (described as the experimental procedures that can lead to higher quality data with less cost) is becoming an important tool in designing acquisition schemes in other geophysical exploration techniques, few studies have addressed this problem in gravity [22].

The main objective of this study, therefore, is to verify if possible alternate station grid schemes could lead to the acquisition of data that, once inverted, could better resolve the properties (in this case density) of the geophysical target. This kind of study, together with the availability of new quantum gravimeters with unprecedented sensitivity, could lead to new and more effective data acquisition procedures. This chapter will present the ideas underlying the building of novel grid schemes, and will describe the GRAV3D software used for the inversion of the collected data and the formulation and use of the model resolution matrix to appraise the merits of the different survey grids. Finally, the results from this simulation study will be presented and the possible applications of this method will be described.

3.1 Construction of non-regular grids

The main objective of a gravity survey is to detect a density contrast that can suggest the presence of an anomalous mass or void in the area. It is, indeed, necessary to select the most appropriate sampling scheme to be able to detect the anomaly. Usually, the sampling schemes adopted are rectangular grids where the appropriate data spacing is dictated by the sampling theorem. In particular, it is the depth at which the anomaly is expected to be, that imposes the station spacing. Studies

conducted through the analysis of the decay of wavenumbers with distance from the source [23, 24] found that, in case of noiseless data, with a station spacing approximately equal to the depth, it is possible to perfectly resolve the signal given by a point mass. It is obviously always suggested to oversample the area, given the presence of noise and the necessity of a higher signal-to-noise ratio. These apriori evaluations are applicable to this study that aims to investigate possible alternate acquisition schemes within the limits imposed by the sampling theorem.

In unusual cases, it could be possible to set the data spacing already knowing the expected depth of an anomaly that still needs to be detected or characterised. It is important to highlight, therefore, that usually several geophysical techniques are concurrently used to investigate an area and the information coming from previous explorations are used as apriori knowledge.

3.1.1 Forward modelling

The starting point of this investigation is the simulation of an anomaly mass and the solution of the forward problem. The GRAV3D software developed by the University of British Columbia has been used for the formulation of the forward problem and its inversion. The vertical component of a gravity field produced by a density $\rho(x, y, z)$ can be expressed, as previously seen, by equation 1.6. The forward modelling of gravity data is a linear problem and requires the evaluation of the integral in equation 1.6.

In the software GRAV3D, the region of interest is divided into a set of M 3D prismatic cells (each characterised by a constant density contrast) by using a 3D orthogonal mesh [25]. With such a discretization, the gravity field at the i_{th} location can be written as:

$$d_i = \sum_{j=0}^{M} \rho_j G_{ij}, \tag{3.1}$$

where $d_i \equiv g_z$ is the i_{th} datum, ρ_j is the anomalous density at the j_{th} location and

$$G_{ij} = \gamma \int_{\Delta V_j} \frac{(z - z_0)}{|r - r_{0i}|^3} dv \tag{3.2}$$

is the sensitivity (or data kernel) matrix which quantifies the contribution of the j_{th} cell to the i_{th} datum. A closed formulation for the solution of the integral in 3.2 for a rectangular prism exists, given by Haaz, that is used in the software [26]. Therefore, given the density contrast of cells in the model,

$$\boldsymbol{\rho} = (\rho_1, \rho_2, ..., \rho_M)^T, \tag{3.3}$$

through the sensitivity matrix G it is possible to obtain the gravity data at the N locations

$$\mathbf{d} = (d_1, d_2, ..., d_N)^T \tag{3.4}$$

as

$$\mathbf{d} = \mathbf{G}\boldsymbol{\rho}. \tag{3.5}$$

In particular, an anomalous mass buried at a depth of 10 m with respect to the surface and having an extent of 60 m in both the E-W and N-S directions and 10 m in the z direction, has been simulated. The mesh consists of $10 \times 10 \times 10$ cells. The cells have a width of 20 m both in the x and y direction, while they have a variable height in the z direction, in such a way that their heights increase moving from the surface to the bottom of the mesh. The mass has a density contrast of $0.5 \frac{g}{cm^3}$ with the surrounding rocks and a figure of the simulated model is shown in fig. 3.1.

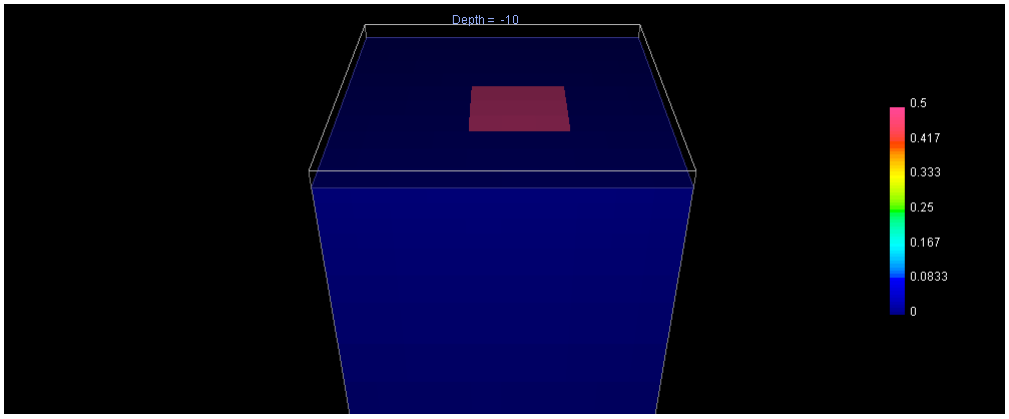

Figure 3.1: Simulated anomaly having dimension 60m $\times$ 60m $\times$ 10m and a density contrast of $0.5 \frac{g}{cm^3}$ with the surrounding rocks. The model has been cut at a depth of 10 m in order to show the anomaly (figure obtained with the MeshTool3D of GRAV3D).Color scale shows the value of density contrast.

An initial 19×19 rectangular grid of 361 measurements points was set, where the data spacing was equal to 10 m consistent with the expected depth of the anomaly. The gravity values obtained by running the forward problem on this initial rectangular grid and at an elevation of 1m from the surface are shown in fig. 3.2.

3.1.2 Horizontal gravity gradients

The idea behind the construction of a survey grid, not based on the classical rectangular spacing, comes from the possibility to use other information coming from the gravity measurements. In particular the horizontal gravity gradients are extremely useful, since high values imply lateral density contrasts and, therefore, the presence of the anomaly to detect [22].

Therefore, starting from the gravity values obtained on the initial regular grid, the horizontal gravity gradients in the x and in the y direction have been computed and a combined horizontal gradient value $\sqrt{(\frac{\partial g_z}{\partial x})^2 + (\frac{\partial g_z}{\partial y})^2}$ has been assigned to the middle point of each rectangle. The values have been normalised by the maximum value of the combined horizontal gradient obtained on the grid. The points where this ratio exceeded a threshold of 0.9 have been selected as extra measurement points with which to infill the initial regular grid.

In this way is possible to obtain an "optimised grid" given by the infilling of the initial regular grid with extra measurement points (selected by the magnitudes of the

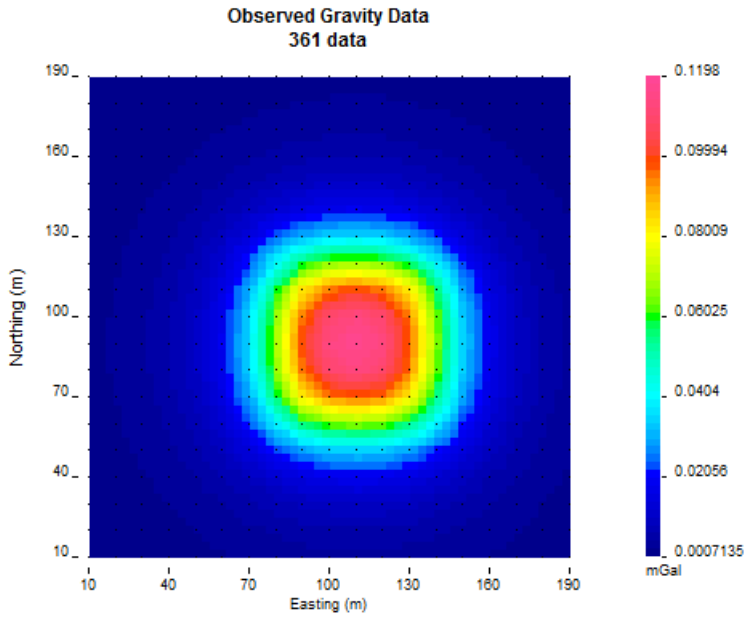

Figure 3.2: Gravity measurements obtained by the anomalous simulated mass. The values of gravity are reported in mGal (figure obtained with the gm-data-viewer of GRAV3D).

horizontal gravity gradients) that should, potentially, be located in the proximity of the boundaries of the anomaly.

The implementation of this algorithm on the initial regular grid of 361 measurement points, has selected 36 extra measurement points, giving an optimised grid of 397 points. The regular grid with the superimposed infilled points is shown in fig. 3.3.

The optimised grid of 397 points has, subsequently, been compared with a regular rectangular grid obtained selecting a data spacing of 9 m and a total number of $21 \times 21 = 441$ points.

If the optimised grid allows a better recovery of the model than a regular grid having a greater number of points, this would reduce the number of points necessary to detect and characterize the anomaly (in our case from 441 to 397) with a clear advantage on the time to spend in the field and the economy of the survey. The method of comparison of the two grids is based on the recovery of the model resolution matrix.

3.2 Recovery of the resolution matrix and model appraisal

As already mentioned in Chapter 2, the model resolution matrix can be used as a tool in the design of a survey, given its dependancy only on the sensitivity matrix of the problem and the possible apriori information added to the problem. It has also already been highlighted that the formulation of the resolution matrix depends on the particular inversion performed. For this reason, there follows a detailed

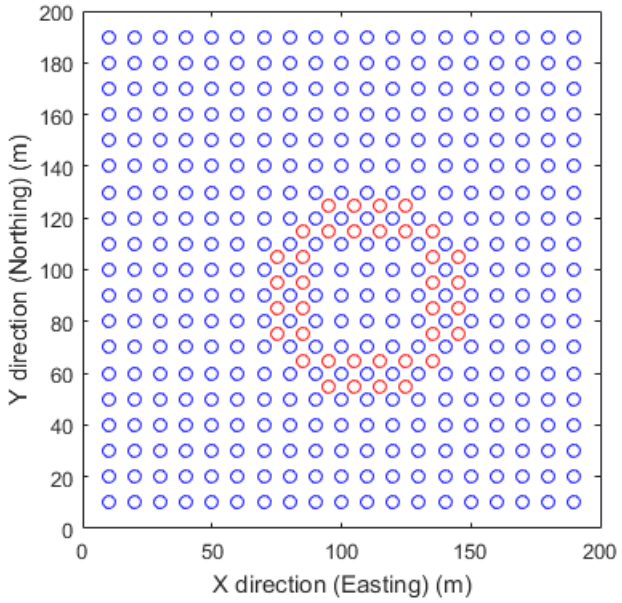

Figure 3.3: Regular grid (blue points) with superimposed infilled points (in red).

description of how the inversion is performed in the GRAV3D software utilized for this study and how it is possible to recover the resolution matrix of the model.

3.2.1 Inversion of gravity data

The data obtained from the optimised and regular grids have been inverted with the GRAV3D software in which the inverse problem is formulated as an optimisation problem where a global objective function

$$\phi = \phi_d + \beta\phi_m, \tag{3.6}$$

is minimized subject to constraints in the form of user-supplied lower and upper bounds on the density

$$\rho^l \leq \rho \leq \rho^u. \tag{3.7}$$

The first term to be discussed is the model objective function ϕ_m. As already explained in Chapter 2, in the case of ill-posed problems, it is necessary to add prior information available to select a unique solution. The model objective function represents the term in which the prior geological information is included and, in the GRAV3D case, is given by

$$\begin{aligned}\phi_m(\rho) = \alpha_s \int_V w_s\{w(\mathbf{r})[\rho(\mathbf{r}) - \rho_0]\}^2 dv \ + \alpha_x \int_V w_x\{\frac{\partial w(\mathbf{r})[\rho(\mathbf{r}) - \rho_0]}{\partial x}\}^2 dv \ + \\ \alpha_y \int_V w_y\{\frac{\partial w(\mathbf{r})[\rho(\mathbf{r}) - \rho_0]}{\partial y}\}^2 dv \ + \alpha_z \int_V w_z\{\frac{\partial w(\mathbf{r})[\rho(\mathbf{r}) - \rho_0]}{\partial z}\}^2 dv \ .\end{aligned} \tag{3.8}$$

The first term penalizes the discrepancies between the recovered model and a reference model ρ_0. The final three terms, on the other hand, help the model to be flat and smooth in the three spatial directions. The functions w_s, w_x, w_y and w_z are

spatially dependent and $w(\mathbf{r})$ is a generalized depth weighting function that helps the absence of depth resolution in gravity data, counteracting the kernel's natural decay and the concentration of the solution near the observation points [25]. In this study only the first term is used in the inversion, setting the coefficients $\alpha_s = 0.0001$ and $\alpha_x = \alpha_y = \alpha_z = 0$, meaning that the solution to the inverse problem will be a model that is as close as possible to ρ_0.

Numerically, the model objective function in 3.8 is discretised over the mesh and, taking into account only the term actually used in this research, this yelds

$$\begin{aligned} \phi_m(\boldsymbol{\rho}) &= (\boldsymbol{\rho} - \boldsymbol{\rho}_0)^T(\alpha_s \mathbf{W}_s^T \mathbf{W}_s)(\boldsymbol{\rho} - \boldsymbol{\rho}_0) \\ &\equiv (\boldsymbol{\rho} - \boldsymbol{\rho}_0)^T \mathbf{W}_m^T \mathbf{W}_m (\boldsymbol{\rho} - \boldsymbol{\rho}_0), \\ &= ||\mathbf{W}_m(\boldsymbol{\rho} - \boldsymbol{\rho}_0)||^2. \end{aligned} \tag{3.9}$$

Here, $\mathbf{W}_s = \mathbf{S}_s \mathbf{D}_s \mathbf{Z}$, where $\mathbf{S}_s$ is a diagonal matrix having elements $\sqrt{w_s}$ defined over each cell of the mesh, $\mathbf{D}_s$ has elements $\sqrt{\Delta x \Delta y \Delta z}$ on its diagonal (Δx, Δy and Δz are respectively the cell sizes in the three directions) and $\mathbf{Z}$ is a diagonal matrix representing the discretized form of the depth weighting function [27].

The first term of the global objective function is the data misfit

$$\phi_d = ||\mathbf{W}_d(\mathbf{G}\boldsymbol{\rho} - \mathbf{d})||^2, \tag{3.10}$$

where $\mathbf{W}_d$ is a diagonal matrix whose i^{th} element is given by $\frac{1}{\sigma_i}$ where σ_i is the standard deviation on the i^{th} datum. Weighting the misfit with a matrix of the standard deviations, gives the possibility to take into account the distribution of contaminating noise on the data. In particular, when the noise is assumed to be independent and Gaussian with zero mean, ϕ_d becomes a chi-squared distribution with N degrees of freedom (N being the number of data). Therefore, when

$$\phi_d = \phi_d^* = N, \tag{3.11}$$

an acceptable fit has been obtained.

The importance of one term with respect to the other in the global objective function ϕ is regulated by the trade off parameter β defined thorugh the L-curve criterion explained in Chapter 2.

The optimization problem with the imposed constraints, is solved with the projected gradients method [28]. This iterative method forces the gradient of the objective function to be zero if the proposed next step would make the model exceed the bound constraints [25], and so restricts the solution to the range given by equation 3.7.

3.2.2 Formulation of the model resolution matrix

If the inversion of gravity data was performed through a Tikhonov regularisation without further constraints the resolution matrix of the model would be:

$$\mathbf{R} = (\mathbf{G}^T \mathbf{W}_d^T \mathbf{W}_d \mathbf{G} + \beta \mathbf{W}_m^T \mathbf{W}_m)^{-1} \mathbf{G}^T \mathbf{W}_d^T \mathbf{W}_d \mathbf{G}, \tag{3.12}$$

where $\mathbf{G}^T\mathbf{W}_d^T\mathbf{W}_d\mathbf{G} + \beta\mathbf{W}_m^T\mathbf{W}_m = \mathbf{H}$ is the approximated Hessian matrix.

However, this study uses an inversion algorithm (projected gradients method) that also incorporates lower and upper constraints. As a result, there doesn't exist a closed formulation for the Resolution matrix, given the fact that there is no analytic explicit expression for $\mathbf{H}^{-1}$, which is defined implicitly by the specific inversion process that incorporates the bound-constraints.

In such cases, it is possible to numerically generate the resolution matrix column by column [24]. This numerical procedure originates from the observation of the expression of the recovered model for an unconstrained problem

$$\boldsymbol{\rho}_{est} = \mathbf{H}^{-1}\mathbf{G}^T\mathbf{W}_d^T\mathbf{W}_d\mathbf{d}_{obs}. \tag{3.13}$$

Substitution of the equation $\mathbf{G}\boldsymbol{\rho}_{true} = \mathbf{d}_{obs}$ into 3.13 leads to the definition of the Resolution matrix, as already seen in Chapter 2:

$$\boldsymbol{\rho}_{est} = \mathbf{H}^{-1}\mathbf{G}^T\mathbf{W}_d^T\mathbf{W}_d\mathbf{G}\boldsymbol{\rho}_{true} \equiv \mathbf{R}\boldsymbol{\rho}_{true}. \tag{3.14}$$

On the other hand, if the true model consists of only one cell corresponding to the j^{th} cell

$$\boldsymbol{\rho}_j = [\rho_1, \rho_2, ..., \rho_M]^T, \tag{3.15}$$

substituting this impulse perturbation in 3.13 yields the j^{th} column of the resolution matrix. The same column can, therefore, be obtained by inverting the data produced by the impulsive model ρ_j

$$\mathbf{d}_{obs}^j = \mathbf{G}\boldsymbol{\rho}_j. \tag{3.16}$$

If this procedure is repeated for all the cells of the model, it is possible to recover all the columns of the resolution matrix [29].

To summarise how to obtain one column of the resolution matrix, firstly an inversion of the observed data is conducted and the optimal regularization parameter β_{opt} is established. After, the same inverse operator (defined implicitly by the sensitivity matrix $\mathbf{G}$, the same bound constraints, the same data and model weighting matrices $\mathbf{W}_d$ and $\mathbf{W}_m$ and the same regularisation parameter β_{opt}) is used to invert the synthetic data generated by a model consisting of an impulse pertubation in a single cell of the mesh [24, 29].

Although this algorithm ensures the recovery of the resolution matrix, it is quite time consuming, giving the necessity to run M inversions in order to perturb each cell of the model. Therefore, it is worthwile to test if the definition of resolution matrix given in 3.12 could be a good approximation to the resolution matrix recovered using the above algorithm. In order to do this, for each survey grid (optimal or regular) different columns of the resolution matrices obtained with both methods have been compared.

To build the resolution matrix column by column, the GRAV3D software has been used in order to run the necessary inversions, while to build the resolution matrix, with the closed formulation, the Matlab software was used. In particular, since it was not possible obtain the sensitivity matrix $\mathbf{G}$ from the GRAV3D software, a code has been written to calculate the matrix, using the same closed formulation of the

gravitational attraction of the right rectangular prism used in the UBC software. Also, it is important to mention that the GRAV3D software performs a wavelet compression of the sensitivity matrix $\mathbf{G}$ to deal with the problem, frequently encountered in gravity, of storing and performing operations on large sparse matrices. To avoid differences in the calculation of $\mathbf{G}$ and enable comparison of the resulting resolution matrices, all the inversions with the GRAV3D have been performed without compressing the sensitivity matrix in the wavelet domain. The matrices $\mathbf{W}_m$ and $\mathbf{W}_d$ have been computed following the definitions presented in the previous paragraph.

In all the cases tested, it turned out that the two matrices were identical. This outcome would suggest that, in all the inversions performed, the estimated solution never reaches the boundaries. Therefore, in these specific cases, the information contained in the closed formulation of the resolution matrix without constraints is exactly the same as included in the resolution matrix with bound constraints.

Some examples of comparisons between the first columns and the last columns of the resolution matrices, obtained with the different procedures described, are shown in Fig. 3.4 and Fig. 3.5.

(a) Column 1 of $\mathbf{R}$ without constraints

(b) Column 1 of $\mathbf{R}$ with constraints

Figure 3.4: First columns of the two Resolution matrices without and with bound constraints. The column vectors have been reshaped to be plotted as grids.

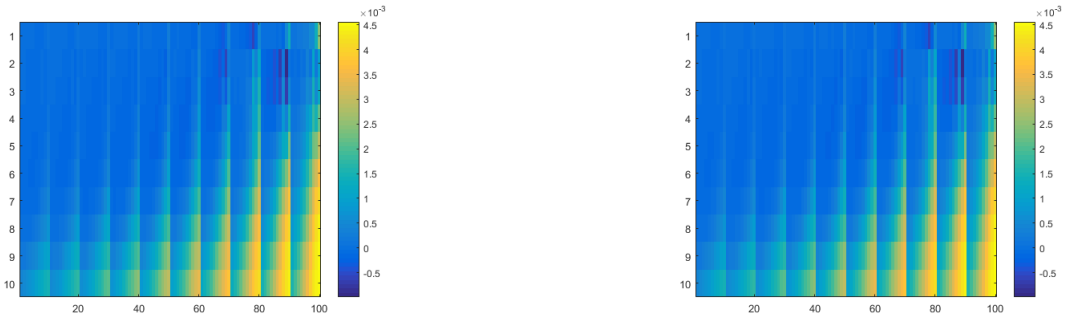

(a) Column 1000 of $\mathbf{R}$ without constraints

(b) Column 1000 of $\mathbf{R}$ with constraints

Figure 3.5: Last columns of the two Resolution matrices without and with bound constraints. The column vectors have been reshaped to be plotted as grids.

3.3 Application of the method and results

Once the different grids were obtained, both regular and infilled, and it was verified that the resolution matrices with and without bound constraints gave equal results, the latter being used for the model appraisal. In particular, each survey grid has been characterized by its model resolution matrix and the resolution matrices of different grids have been compared in order to select that which gave a better recovery of the model.

The data obtained from the solution of the forward problem on the initial regular grid of 361 points have been inverted, after a standard deviation equal to 5 % of the measurement plus 0.0001 mgal was added to the data. As already mentioned, only the first component of the objective function has been used by setting the coefficients to $\alpha_s = 0.0001$ and $\alpha_x = \alpha_y = \alpha_z = 0$ and the reference model was set to zero. The inversion, bounded between -1 and 1 gave an optimum value for the regularisation parameter β of 3.175×10^4. Using the same β, $\mathbf{W}_m$ and $\mathbf{W}_d$ the resolution matrices were calculated.

In order to compare the resolution matrices of different grids and take into account only the effect caused by the particular positioning of the measurement points, all the elements of the inversion, except for the sensitivity matrix $\mathbf{G}$ and the data weighting matrix $\mathbf{W}_d$ have been taken to be constant. Therefore, using the same β resulting from the inversion of the initial regular grid, the same $\mathbf{W}_m$ and boundary constraints, the data obtained from the optimised grid of 397 points and from the final regular grid of 441 points were both inverted. In these cases, since the β value has been imposed, the inversion does not use the L-curve criterion. Again, the resolution matrices for these grids were calculated.

It was decided to perform the analysis of the resolution matrices of the different grids by examining only the diagonal elements and their dissimilarity from unity (i.e. from perfect resolution). An example of the diagonal elements of the resolution matrix obtained from the inversion of the data of the 361 grid, plotted on their respective cells, is shown in Fig. 3.6.

Note that the values of the diagonal elements decrease with depth, but also that lower values occur right above the location where the anomaly is expected to be. This is not unexpected and is caused by the matrix $\mathbf{W}_d$ in the definition of the resolution matrix. In fact, recalling that the elements of the $\mathbf{W}_d$ matrix are defined as the inverse of the standard deviation, and noticing that the standard deviation is taken as a percentage of the measurement plus a fixed threshold, it is clear that in the proximity of the anomaly, where the values of gravity are higher and the standard deviations are higher, the inverse values will be lower. Therefore, these lower values weight the resolution matrix in such a way to decrease the diagonal elements in the proximity of the anomaly.

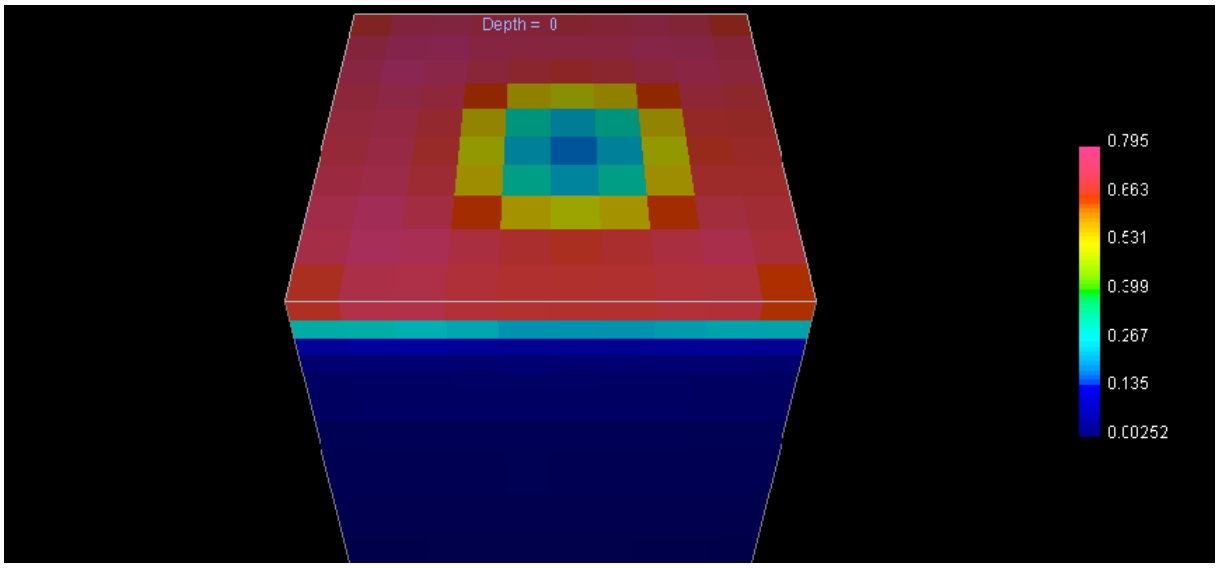

Figure 3.6: Resolution matrix of the model obtained from the inversion of the data collected on the initial regular grid of 361 measurement points

In order to obtain an immediate comparison between the different resolution matrices obtained by the optimised grid of 397 points and the regular grid of 441 points, the ratios between the diagonal elements of the two grids and the original grid of 361 points has been calculated

$$R1 = \frac{diag(\mathbf{R397})}{diag(\mathbf{R361})}, \tag{3.17}$$

$$R2 = \frac{diag(\mathbf{R441})}{diag(\mathbf{R361})}, \tag{3.18}$$

where **R361** represents the resolution matrix of the initial regular grid of 361 points, **R397** represents the resolution matrix of the optimised grid of 397 points and **R441** represents the resolution matrix of the regular grid of 441 points.

When $R1 = 1$ it means that the resolution obtained with the optimised grid is the same as that obtained with the initial regular grid. On the other hand, if $R1 > 1$ or $R1 < 1$ the resolution of the optimised grid is respectively greater or smaller than the resolution of the initial regular grid. The same logic applies to the interpretation of $R2$ regarding the resolution of the final regular grid.

More important for this analysis is the comparison between $R1$ and $R2$. This comparison, in fact, allows the evaluation of the ultimate aim of this study, or in other words, if there is a gain in resolution using the optimised grid.

In particular, if $R1 = R2$ the optimised grid and the regular grid of 441 measurement points lead to the same resolution, if $R1 < R2$ (i.e. $R1/R2 < 1$) then the 441 regular grid allows a better recovery of the model, while if $R1 > R2$ (i.e. $R1/R2 > 1$) the optimised grid resolves the cell better than the regular grid with more measurement points.

From a comparison between $R1$ and $R2$ we find out that, for most of the cells, $R2 > R1$ suggesting that the regular grid of 441 points allows a better resolution

than the optimised grid. This is expected since the 441 regular grid has a greater density of measurements in most regions of the grid. However, it is interesting to see that the opposite is true for cells near the location of the anomaly, that is $R1 > R2$. The values of the two ratios for different cells in the proximity of the anomaly are shown in the figures 3.7, 3.8 and 3.9, together with the values of the ratio $R1/R2$.

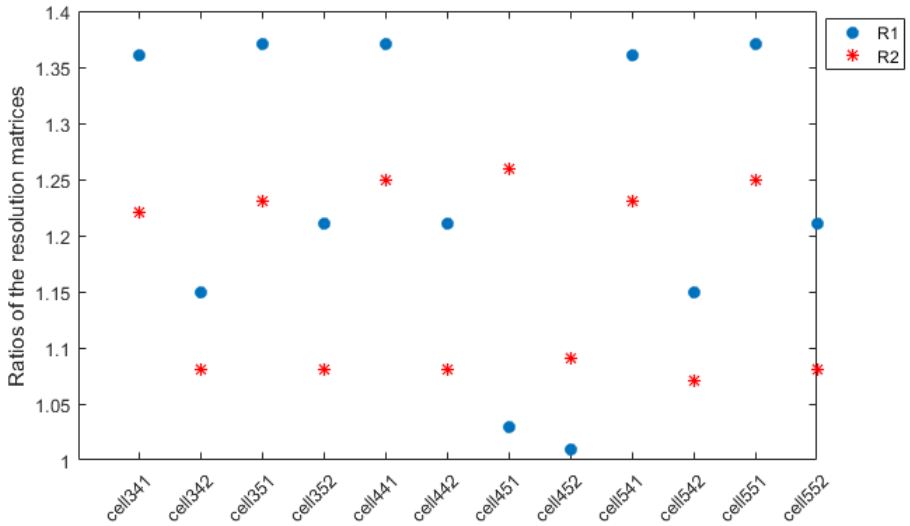

(a) R1 and R2 values for a number of cells in the proximity of the anomaly

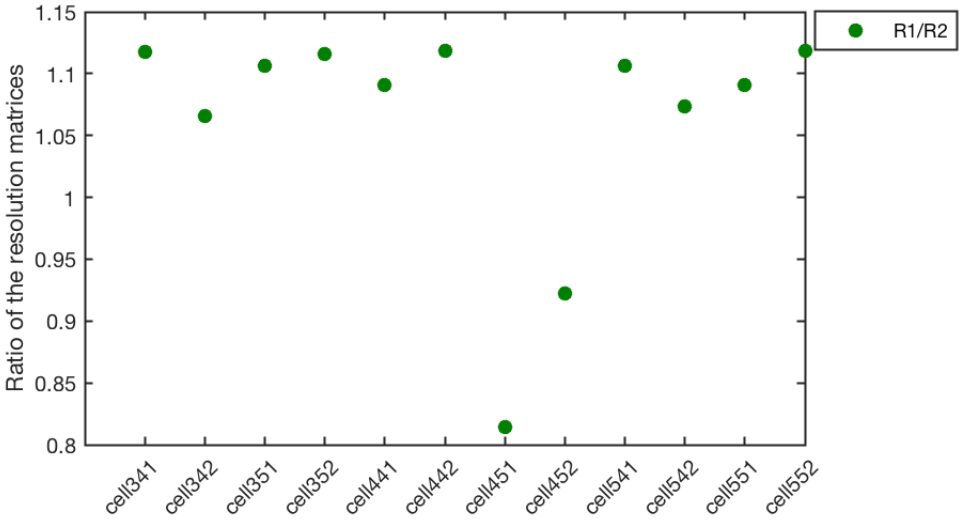

(b) R1/R2 values for a number of cells in the proximity of the anomaly

Figure 3.7: R1, R2 and $R1/R2$ values plotted on several cells in the proximity of the anomaly.

This is an important result for this investigation, because, if it is desirable to improve the detection and inversion of the anomaly, it is more important to gain resolution in the area in the proximity of the anomaly rather than in other areas of the survey. Therefore, it is clear that this gain of resolution is obtainable with the costruction of an optimised grid even when this is compared with a regular grid with 44 more measurement points.

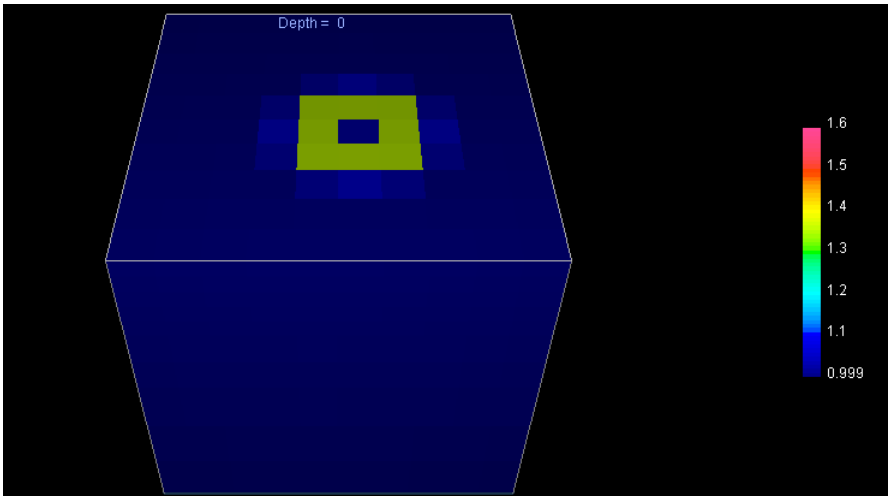

(a) R1 values plotted on the relative cell

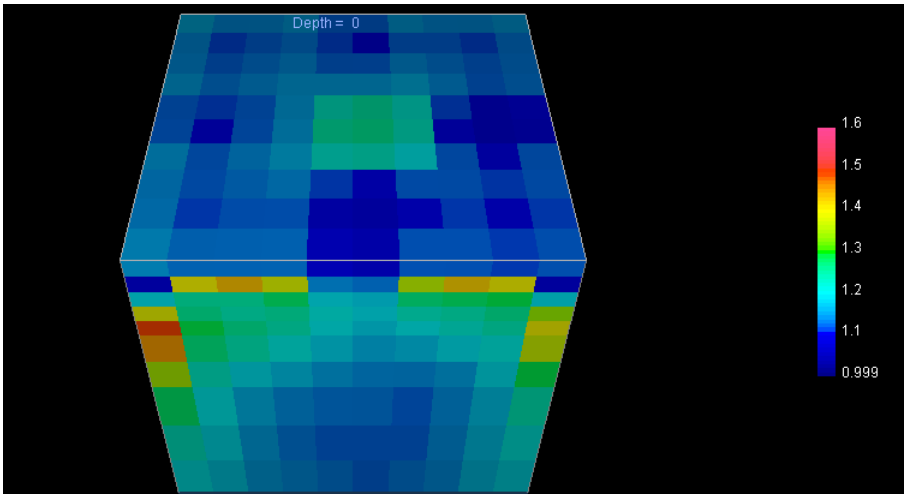

(b) R2 values plotted on the relative cell

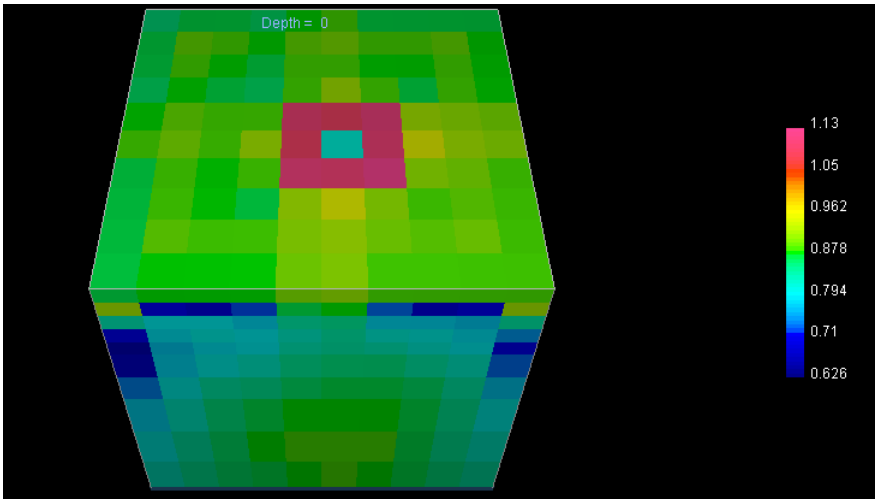

(c) R1/R2 values plotted on the relative cell

Figure 3.8: R1, R2 and $R1/R2$ values plotted on the relative cells.

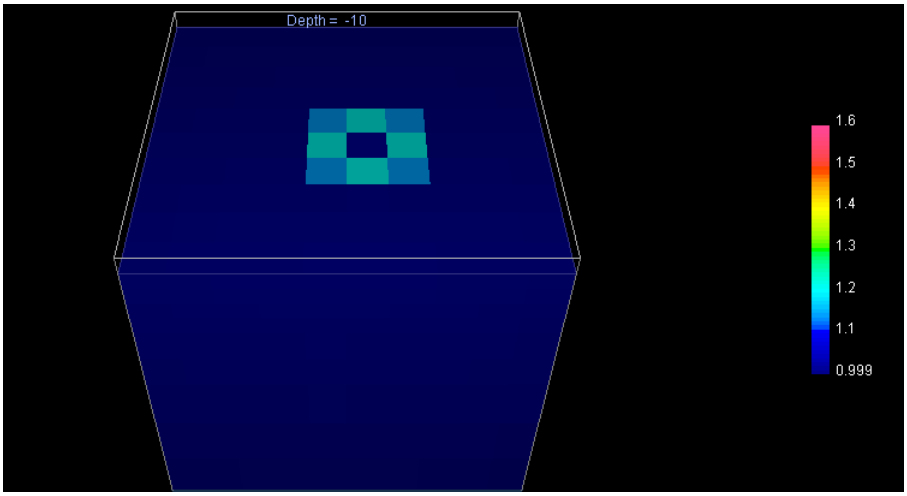

(a) R1 values plotted on the relative cell at 10 m of depth

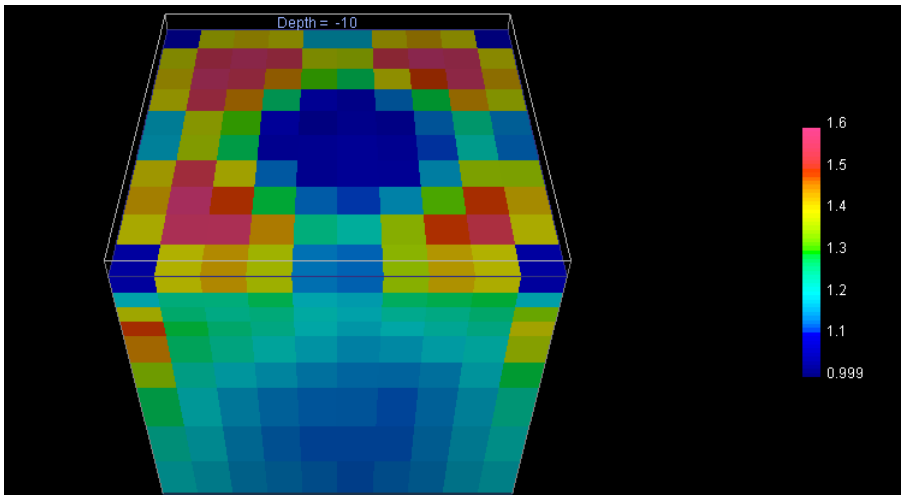

(b) R2 values plotted on the relative cell at 10 m of depth

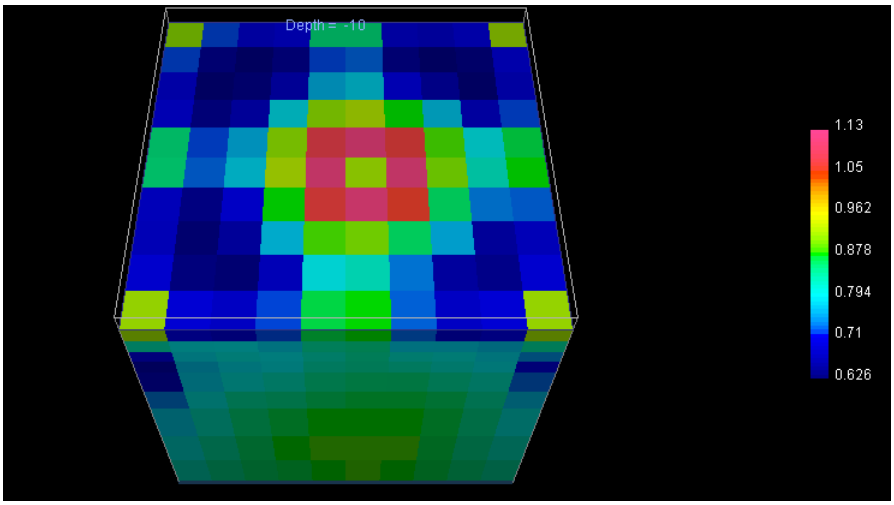

(c) R1/R2 values plottes on the relative cell at 10 m of depth

Figure 3.9: R1 ,R2 and $R1/R2$ values plotted on the relative cells at 10 m of depth.

3.4 Comparison between the true and inverted models

A comparison between the true model (shown in fig. 3.6) and the inverted models obtained with the 397 optimised grid and the 441 regular grid can be done in order to verify how well the anomaly is resolved with the two different grids. In particular an RMS value can be defined to evaluate a total deviation of the inverted model from the true model

$$\Delta\rho = \sqrt{\frac{1}{M}[(\rho_1^{true} - \rho_1^{inv})^2 + (\rho_2^{true} - \rho_2^{inv})^2 + ... + (\rho_M^{true} - \rho_M^{inv})^2]}, \tag{3.19}$$

where ρ_i^{true} is the value of the density contrast assigned to the i^{th} cell of the true model, ρ_i^{inv} is the density contrast obtained from the inversion for the i^{th} cell and M is the number of cells of the model.

If $\Delta\rho$ is calculated over all the M cells of the inverted models of the optimised ($\Delta\rho_{397}$) and the regular grid ($\Delta\rho_{441}$) , it should show, given the results obtained with the ratios of the diagonal elements of the resolution matrices, that $\Delta\rho_{441} < \Delta\rho_{397}$, or, in other words, that the regular grid, having a higher density of points, allows a better recovery of the model. But, if we define a localised $\Delta\rho$, considering in the RMS value only several cells of the model in the proximity of the anomaly, the inequality should be inverted and $\Delta\rho_{441} > \Delta\rho_{397}$.

In fact, first the $\Delta\rho$ over all the $M = 1000$ cells of the model is calculated, given $\Delta\rho_{441} = 0.045443$ and $\Delta\rho_{397} = 0.045648$. Instead, if only the cells of the model shown in fig.3.7 are used in the summation, $\Delta\rho_{441} = 0.288672$ and $\Delta\rho_{397} = 0.288557$. Therefore, again it is verified that the optimised grid allows a better recovery of the model with respect to the regular grid, in the proximity of the anomaly. Also, it is worth mention that, while the analysis of this chapter was performed for a positive density anomaly, the same results can be expected in case of a lower or even negative density anomaly since, in the resolution matrix, only the term $\mathbf{W}_d$ and its transpose would change.

3.5 Possible applications

From the results presented, it is clear that there are possible advantages offered in terms of gain of resolution and reduction of the time of the survey by the implementation of an optimised grid.

However, as presented, the method suggests the necessity of collecting the data on an initial rectangular grid to obtain the information of the gravity gradients. It is possible, though, to imagine an "on-field" implementation of the method once a quantum gravity sensor becomes available on the market. Currently, gravity measurements are collected along parallel lines in order to correct the inevitable drift of the sensor. The use of a quantum sensor, that won't experience any drift, could allow the implementation of collection schemes designed to obtain in "real-time" an estimate of the horizontal gravity gradients. The information from the horizontal

gravity gradients could, eventually, inform the design of the survey in real time, with infill points being measured depending on the magnitudes of the gravity gradients. An example of a possible scheme is presented in fig. 3.10.

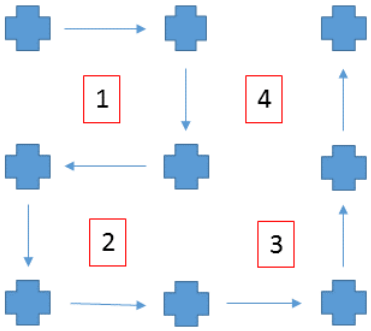

Figure 3.10: Example of a collection scheme to obtain the horizontal gravity gradients "on-field". The crosses indicate the measurement points, the arrows the direction of collection and the numbers indicate the progress of the values of gravity gradients made available by the measurements.

It is also important to underline that, if such "on-field" implementation were performed, the gravity data collected won't be already corrected for the presence of other gravity fields, as it is in the simulation presented in this research. This could lead to false interpretations of the values of the horizontal gravity gradients that could reflect not only the presence of a lateral density contrast due to the anomaly, but also the presence of a variation in the terrain. It would be necessary, therefore, also to address the study of a possible "on-field" terrain correction.

Moreover, this optimised grid method can also be implemented if a quantum gradiometer, which measures the vertical gradient of g_z, is used for the survey. In this case all the calculations of the horizontal gradients, the inversion and the resolution matrices vary accordingly.

3.6 Summary

This chapter has described:

- The main steps behind the construction of a non-regular optimised grid.
- The comparison of the performances of a regular and an optimised grid, through the use of their resolution matrices.
- The application of the method and the obtained results.
- The possible "on-field" applications of the method proposed.

The above elements, are necessary to describe the new proposed method to collect gravity measurements through an optimised grid. Therefore, the first section is

important to understand how an anomalous mass density was simulated, and how an optimised grid can be built using the information coming from the horizontal gravity gradients, once the forward problem is solved. When the regular and the optimised grids are available, together with the gravity measurements, it is described how the two model resolution matrices can be obtained, and how they can be used to compare the performances of the different grids. The application of the method is described in detail, as well as the results obtained. These, in particular, proved that better resolution is reached exactly where most needed (in the proximity of the anomaly) with the optimised grid, even when this has a lower number of measurement points than the regular one. Finally, the possible future implementation of an "on-field" version of the optimised grid is described, in conjuction with the use of the quantum gravity sensors.

Chapter 4

Trapping and cooling atoms

As already addressed in the introduction, the need to develop more sensitive and portable quantum gravity sensors leads inevitably to the field of integration and miniaturisation of experimental components. In particular, the miniaturization of electric and magnetic potentials and the integration of optical components is essential to build schemes to actively trap and cool neutral atoms. In this Chapter the theory of the magnetic trapping of neutral atoms is presented together with some examples of currently used magnetic trap configurations. Also, a theory of the forces acting on an atom in a laser field is discussed and the chapter concludes with a discussion of the integration of laser beams and spatially-varying magnetic fields to form a magneto-optical trap. This chapter lays the foundations of the work described in Chapter 5 using Comsol multiphysics software for the optimisation of purely magnetic traps and in Chapter 6 on the simulation of the forces acting on an atom in a MOT.

4.1 The Zeeman effect

Magnetic trapping of neutral atoms is due to the Zeeman effect, caused by the interaction of the magnetic moments of the electron and the nucleus with the magnetic field [30]. In order to understand this interaction it is useful to write and discuss the complete Hamiltonian of an atom.

In the absence of an external magnetic field the hyperfine interaction is responsible for the splitting of the atomic levels of the atoms. For this interaction the operator for the total quantum momentum needs to be considered:

$$\mathbf{F} = \mathbf{I} + \mathbf{J}, \tag{4.1}$$

where $\mathbf{I}$ represents the operator of the nuclear spin, while $\mathbf{J}$ is the operator for the electronic angular momentum. The Hamiltonian describing the only hyperfine interaction is given by

$$H_{HI} = A\mathbf{I} \cdot \mathbf{J}, \tag{4.2}$$

where only the magnetic dipole term is taken into account (A is the magnetic dipole constant). If the interaction with an external magnetic field $\mathbf{B}$ is considered, the total Hamiltonian becomes

$$H = H_{HI} + V_B, \tag{4.3}$$

where

$$V_B = -\boldsymbol{\mu} \cdot \mathbf{B} = -\frac{\mu_B}{\hbar} g_F \mathbf{F} \cdot \mathbf{B}, \tag{4.4}$$

$\boldsymbol{\mu} = g_F \frac{\mu_B}{\hbar} \mathbf{F}$ is the magnetic moment, g_F is the Landé factor of the atomic hyperfine state and μ_B is the Bohr magneton.

In most experiments on alkali atoms, the external magnetic field is weak enough to ensure that the interaction in eq. 4.4 is small compared with the hyperfine splitting. Therefore, to first order in the magnetic field, the Zeeman energy can be written as

$$E_{Zeem} = g_F \mu_B m_F B, \tag{4.5}$$

where m_F is the magnetic quantum number.

Further details on how to treat the cases of strong field and intermediate field strength can be found in [31].

From the orientation of μ with respect to the orientation of the magnetic field $\mathbf{B}$ two possible cases emerge. In the first case, μ is pointing in the same direction of $\mathbf{B}$ (or in other words, the magnetic moment μ is positive) and $V_B < 0$; the atom experiences a force that drives it towards regions of increasing field. Such atom are referred to as *high-field seekers*.

In the second case, μ has opposite direction relative to the magnetic field (meaning that μ is negative) and $V_B > 0$, producing a force that drives the atom towards regions of lower field. Atoms with a negative magnetic moment are, therefore, called *low-field seekers*.

Therefore, in order to build a magnetic trap, a magnetic field profile with either a local minimum or a local maximum is desired. Given the fact that it is impossible to have a local maximum in $|\mathbf{B}|$ in regions were there are no electrical currents [32], the only atomic states that can be trapped in a pure magnetic trap are low-field seekers.

There are different possible configurations of traps built with the objective of having a minimum in the magnetic field profile, but a main classification into two distinct types of trap is possible: ones where the minimum of the field is exactly zero, and those where it is non-zero. The most important traps developed are presented in the next paragraph.

4.2 Magnetic traps

Different schemes to trap atoms via magnetic fields and the use of the Zeeman effect alone have been proposed. Despite the difference in the details of traps that work with a zero as a minimum in the magnetic field and traps that work by trapping atoms with a non-zero minimum in the magnetic profile, the general design of the traps is quite similar and will now be described in turn. In addition it is important to note that the energy depth of the magnetic trap depends on the intensity of the magnetic field. Given the small field usually used, this energy depth, if converted to thermal energy, is usually less than 1 K. Therefore, in order to trap the atoms, they need to be previously cooled within a magnetic-optical trap.

4.2.1 The quadrupole trap

One classic magnetic field configuration in which the minimum vanishes at a certain location is the quadrupole trap. This is important in our investigation since, with such a trap, we obtain the same field profile as that produced by the Comsol coil simulation model and used in the simulation of the magneto optical trap. In this trap the magnetic field varies linearly in all directions and can be produced, for example, by a pair of opposed Helmoltz coils. If the field gradient and the components along the x and y directions are denoted by B', then along the z direction the gradient is $-2B'$ so that $\nabla \cdot \mathbf{B} = 0$. If the minimum is chosen to be at the origin of the coordinate system, the magnetic field is given by:

$$\mathbf{B} = B'(x, y, -2z) \tag{4.6}$$

and the magnitude of the field is

$$B = B'\sqrt{x^2 + y^2 + z^2}. \tag{4.7}$$

The magnetic field magnitude is, therefore, zero at the centre of the trap and varies linearly moving from the minimum but with different gradients in different spatial directions.

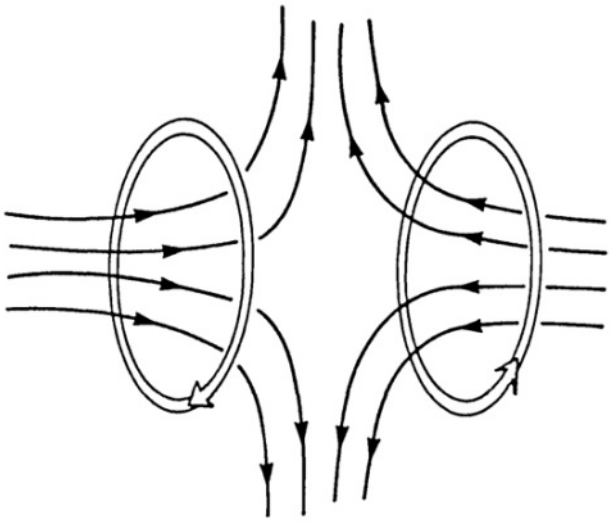

Figure 4.1: Currents through opposing Helmholtz coils (white arrows) and the resultant magnetic field lines (black arrows).

Despite the extensive use of this trap because of the simplicity of the design and the potential for optical access, there is one important disadvantage that needs to be faced. In fact the implicit assumption of the above considerations is that the atoms remain in the same quantum state. If this assumption can be considered true for a stationary atom, it is not necessarily true for moving atoms that are subject to a time-dependent magnetic field, which can induce transitions between different states.

It is intuitive that this effect can become serious if low-field-seeker atoms make the transitions to high-field-seekers and, instead of being trapped, are ejected from the

trap. This can happen quite frequently in the vicinity of the minimum of the field because the frequency of the time-dependent magnetic field becomes comparable with the frequency of the spin-flip transitions, $\mu_B B/\hbar$, which approaches zero when B=0 at the centre of the trap [30].

The presence of a "hole" in the quadrupole trap restricts its performance, resulting in a trap that can store atoms only for a limited amount of time. This limitation can be fixed with two different approches. The first simple approach is to work with magnetic field profiles that present a non-zero field at the minimum. The second approach is known as "plug the hole" and is obtained by adding an oscillating bias magnetic field (see next section).

4.2.2 The TOP trap

The disadvantages arising in the quadrupole trap are bypassed in a modified quadrupole trap called time-averaged orbiting potential or TOP. This trap is still underpinned by a quadrupole field, but has a rotating spatially uniform bias magnetic field superimposed, leading to the following instantaneous field:

$$\mathbf{B} = (B'x + B_0 \cos\omega t, B'y + B_0 \sin\omega t, -2B'z). \tag{4.8}$$

where the frequency of the bias field is chosen to be low compared with the typical frequencies of the sublevel hyperfine transitions.

With such a bias field, the position of the zero in the magnetic field is instantaneously moved, thus never allowing the atoms to change their quantum states and potentially escape from the trap. This field does not vanish at any point in space, and this can be proved by performing the time average of the magnitude of the magnetic field over a rotation period of the field $T = \frac{2\pi}{\omega}$. If the instantaneous intensity of the magnetic field is

$$B(t) = \sqrt{(B_0 \cos\omega t + B'x)^2 + (B_0 \sin\omega t + B'y)^2 + 4B'^2 z^2}, \tag{4.9}$$

then for $r = \sqrt{x^2 + y^2 + z^2} \ll r_0$ where $r_0 = |\frac{B_0}{B'}|$ is the radius onto which the origin of the quadrupole field is displaced, it can be approximated by

$$B(t) \simeq B_0 + B'(x\cos\omega t + y\sin\omega t) + \frac{B'^2}{2B_0}[x^2 + y^2 + 4z^2 - (x\cos\omega t + y\sin\omega t)^2]. \tag{4.10}$$

Performing the time average as $< B(t) >_t = \frac{1}{T}\int_0^T B(t)dt$, it is possible to obtain

$$< B >_t \simeq B_0 + \frac{B'^2}{4B_0}(x^2 + y^2 + 8z^2). \tag{4.11}$$

It is clear, then, from this result, that the time-averaged field does not present a "hole" at any location.

4.2.3 Ioffe trap

As mentioned previously, static magnetic traps having a zero minimum in the magnetic field are not the only possibility. In fact, an inhomogeneous magnetic field having a non-zero minimum may also be generated with two Helmholtz coils. In this case, unlike the quadrupole trap, the currents circulate in the two Helmholtz coils in the same directions.

If the midpoint on the symmetry axis passing through the two coils is taken as the origin of the coordinate system, z is the coordinate in the direction of the symmetry axis, and ρ is the distance from the axis, the magnetic potential can be expanded in terms of spherical harmonics and the resulting magnetic field has the following components

$$\begin{aligned} B_z &= -A_1 - 3A_3(z^2 - \frac{1}{2}\rho^2) \\ B_\rho &= 3A_3 z\rho \\ B_\phi &= 0, \end{aligned} \tag{4.12}$$

where ϕ is the azimuthal angle and A_1, and A_3 are the coefficients of the expansion of the potential (further details can be found in [30]). The magnitude of the magnetic field, if expressed to second order in z and ρ is

$$B = A_1 + 3A_3(z^2 - \frac{1}{2}\rho^2). \tag{4.13}$$

It is clear, therefore, that this magnetic field does not present a local minimum at the origin. Such a magnetic field is known as a "magnetic bottle" and it was Ioffe who suggested how to modify the configuration in order to obtain the minimum required. He suggested to add other currents carried by conductors parallel to the symmetry axis, in order to break the invariance along that direction, as required to create a minimum at the origin.

These "Ioffe-bars" carry the same current and are arranged as shown in Fig. 4.2.

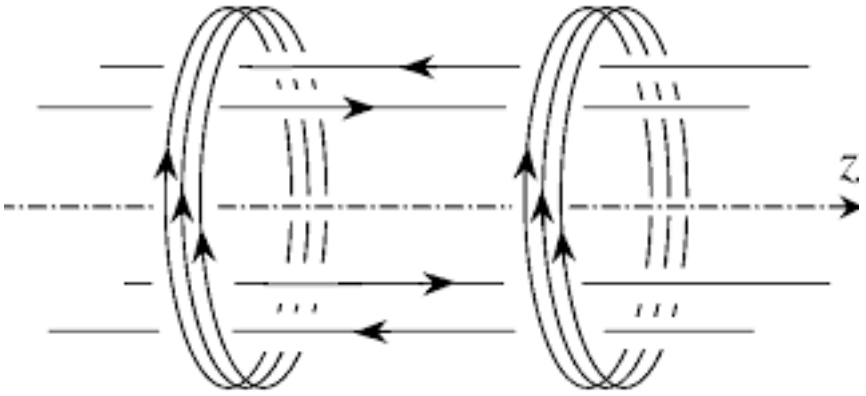

Figure 4.2: The currents of the Helmholtz coils and the added linear "Ioffe bars" that generate the Ioffe-trap magnetic field configuration.

Again, the potential given by the bars can be expanded in terms of spherical harmonics and the components of the magnetic field produced by the Ioffe bars alone are

$$\begin{aligned} B_x &= -Lx \\ B_y &= Ly \\ B_z &= 0, \end{aligned} \tag{4.14}$$

where L is a coefficient of expansion. Consequently, the magnitude of the total magnetic field to second order in the coordinates is:

$$B = A_1 + 3A_3(z^2 - \frac{1}{2}\rho^2) + \frac{L^2}{2A_1}\rho^2. \tag{4.15}$$

Equation 4.15 shows that this field has a local minimum at the origin of the axes if L is chosen to be $L^2 > 3A_1A_3$, which happens if a sufficiently strong current flows through the bars.

4.3 Forces on an atom in a laser field

In order to understand the working principle of the magneto-optical trap, it is necessary to introduce the forces exerted on an atom when it interacts with the electric field generated by lasers.

The response of an atom to an applied harmonic electric field is known as the *Rabi problem* which, if solved with a classical approach, can give some basic results but is not able to explain more complex phenomena. For this reason, it is necessary to solve the Rabi problem with a quantum mechanical approach, assuming that the system can be described as a two-level atom. In this approximation the atom is described by only two energy levels, the ground and excited states, while in the reality it is a multilevel system.

If the formalism of the density matrix is used, the Rabi two level system with a ground state $|g>$ and an excited state $|e>$ can be described by the density matrix (further details on the solution of the Rabi problem and the formalism of the density matrix can be found in [33]),

$$\rho = \begin{pmatrix} \rho_{ee} & \rho_{eg} \\ \rho_{ge} & \rho_{gg} \end{pmatrix}. \tag{4.16}$$

It can be proved that the time dependence of the density matrix is related to the Hamiltonian through

$$i\hbar\frac{d\rho}{dt} = [H, \rho]. \tag{4.17}$$

In this case, the Hamiltonian to be used is the one which describes the interaction between a two-level atom and a time dependent electric field

$$H'(t) = -e\vec{\mathcal{E}}(\vec{r}, t) \cdot \vec{r}. \tag{4.18}$$

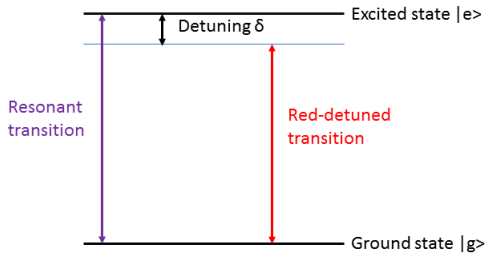

Figure 4.3: Schematic diagram of a Rabi two-level system with a ground state and an excited state and a transition that is red-detuned from the resonance frequency equals to $\hbar\omega$. Redrawn from [34].

If $H'(t)$ is treated as a perturbation to the field-free time independent Hamiltonian, H_0, and the spontaneous emission (the radiative process in which a photon is emitted via a transition from the excited state $|e>$ to the ground state $|g>$ with a scattering rate γ) are added independently, it is possible to obtain a system of four coupled differential equations called the Optical Bloch Equations (OBE).

Once obtained, the OBEs can be used to calculate the forces due to the light. In quantum mechanics the forces can be calculated as

$$F = \frac{d}{dt}\langle p \rangle = -\left\langle \frac{\partial H}{\partial z} \right\rangle, \tag{4.19}$$

further details can be found in [33].

Therefore, substituting the relevant part of the Hamiltonian of the system, $H'(t)$, given in Eq. 4.18, the force is

$$F = e\left\langle \frac{\partial}{\partial z}(\vec{\mathcal{E}}(\vec{r},t)\cdot\vec{r}) \right\rangle. \tag{4.20}$$

Since the expectation value of an operator $\langle A \rangle = Tr(\rho A)$, the force can be written as

$$F = \hbar(\frac{\partial \Omega}{\partial z}\rho^*_{eg} + \frac{\partial \Omega^*}{\partial z}\rho_{eg}), \tag{4.21}$$

where $\Omega = -e\frac{E_0}{\hbar}d_{eg}$ is the definition of the Rabi frequency, E_0 is the electric field amplitude, and d_{eg} is the dipole moment. Note that ρ_{eg} is an off-diagonal element of the density matrix given in Eq. 4.16.

4.3.1 Forces on a two level atom at rest

The force relation expressed in eq. 4.21 can be resolved by substituting the solution of the OBE for ρ_{eg}. For an atom at rest, solving the steady-state optical Bloch equations for ρ_{eg}, and substituting the solution to Eq. 4.21 leads to two different light forces:

- The scattering force originating from the absorption and the spontaneous emission of the photon, can be expressed as

$$F_s = \frac{\hbar k s_0 \gamma}{2(1 + s_0 + (2\delta/\gamma)^2}, \tag{4.22}$$

where k is the photon wave vector, $s_0 = \frac{I}{I_s}$ is the ratio between the light intensity I and the saturation intensity I_s, γ is the scattering rate and δ is the laser detuning from the atomic resonance frequency (fig. 4.3). This force is dissipative because, since it doesn't reverse the spontaneous emission, the action of the force can't be inverted.

- The dipole force which originates from the light shifts of the ground and the excited states, and depends on the strength of the optical elecric field, can be written as

$$F_{dip} = -\frac{\hbar\Omega}{2\delta}\frac{\partial\Omega}{\partial z}, \tag{4.23}$$

where Ω is the Rabi frequency and δ is the detuning. This force is conservative.

Therefore, on an atom at rest, two different kind of forces, having different origin, are exerted by a laser light field: the scattering force, which is dissipative and can be used to cool an atom, and the dipole force, conservative and used for trapping.

4.3.2 Scattering force on a moving atom

Laser cooling is produced by the effect of dissipative forces that are velocity dependent. Therefore, in order to understand the mechanism of laser cooling, atomic motion needs to be considered. It is in theory possible to include the velocity of the atoms in the OBE, but the equations become too complicated to be solved. Therefore, the velocity of the atoms is treated as a small perturbation to the solution of the OBE for an atom at rest [33].

If a single laser beam is considered, atoms moving with a velocity $\vec{v}$ toward or away from the laser source experience a Doppler shift $\omega_D = -\vec{k}\cdot\vec{v}$. Therefore they see a modified value of the total detuning $\delta_D = \delta + \omega_D = \delta - \vec{k}\cdot\vec{v}$. This leads to a velocity-dependent scattering force

$$F_S = \hbar k \gamma_p = \frac{\hbar k s_0 \gamma}{2(1 + s_0 + (2(\delta - kv)/\gamma)^2)}, \tag{4.24}$$

where γ_p is the effective scattering rate.

4.4 Optical molasses

In the previous paragraph the scattering force on atoms moving in a single laser beam was derived. If, instead, two laser beams of the same frequency, intensity and polarization are directed opposite to one another, the formulation of the force

changes producing a viscous damping and the two forces from the two light beams are

$$\vec{F}_{\pm} = \pm\frac{\hbar k\gamma}{2}\frac{s_0}{1+s_0+[2(\delta \mp kv)/\gamma]^2}. \tag{4.25}$$

The sum of the two forces simply provides the total force in the optical molasses, which, in the range of small velocities, can be approximated by a linear dependence

$$\vec{F}_{OM} = \vec{F}_{+} + \vec{F}_{-} \cong \frac{8\hbar k^2 \delta s_0 \vec{v}}{\gamma(1+s_0+(2\delta/\gamma)^2)^2} \equiv -\beta\vec{v}. \tag{4.26}$$

If the laser frequency is slightly red-detuned from the atomic resonance, an atom moving toward one beam will feel a Doppler shift closer to the resonance. In the direction parallel to the motion of the atoms, instead, the frequency of the laser will be shifted further away from resonance. Because of this effect, the atoms will interact more strongly with the laser beam moving in the opposite direction to their velocities, which leads to a total force that acts to slow the atoms (fig. 4.4).

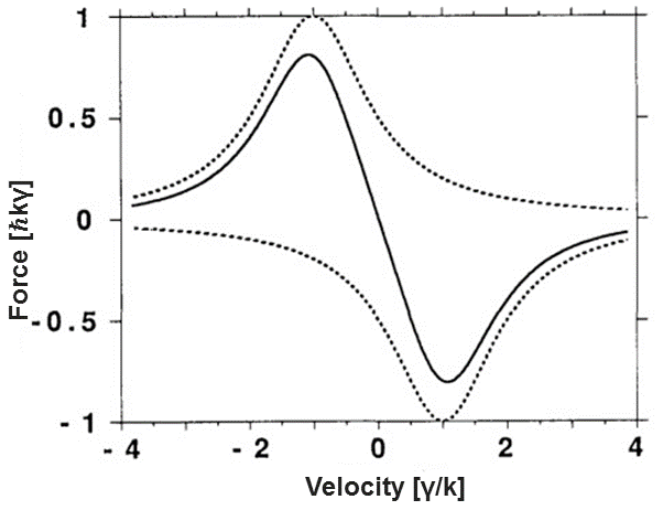

Figure 4.4: Optical damping forces as a function of the atomic velocity. The two dotted traces show the force from each laser beam, while the solid curve is the sum of the forces of the two beams. Taken from [33].

Optical molasses have been discussed above in one dimension but it is clear that this configuration can be extended to two and three dimensions with the intersection of two or three orthogonal pairs of opposing laser beams [35]. Over the years, suggestions were made about the possibility of both cooling and trapping atoms with the scattering force alone, but this is forbidden by the optical Earnshaw theorem [36]. This theorem shows that it is not possible to stably trap atoms using only the scattering force. Therefore, alternative schemes such as the magneto-optical trap have been proposed to actively trap and cool atoms.

4.5 The magneto-optical trap (MOT)

The concept of a magneto-optical trap, that could combine an optical molasses with a spatially inhomogeneous magnetic field, was first introduced in 1987 [37]. The

most common scheme of MOT uses a pair of anti-Helmholtz coils that produce a quadrupole magnetic field, which acts to shift the resonant frequency of the atoms due to the Zeeman effect as described in section 4.2. This creates a restoring force towards the trap centre.

The simplest MOT scheme is a 1D arrangement shown in figure 4.5 for a simple atomic transition $J_g = 0 \rightarrow J_e = 1$. Atoms with $J_g = 0$ (neglecting for simplicity the nuclear spin) are placed in a linearly inhomogeneous magnetic field $\mathbf{B} = \mathbf{B}(x) \equiv B'x$ where B' is a constant gradient as explained in section 4.2.1. Two red-detuned counterpropagating laser beams of opposite circular polarization σ^+ and σ^- are incident as shown in Fig. 4.5 and the magnetic substates of the excited states are labelled by the quantum number M_e. The magnetic field shifts the Zeeman sublevel of the $J_e = 1$ state, with a positive slope for $M_e = +1$ and a negative slope for M_e = -1. Therefore, when an atom moves away from the centre of the trap, it will always interact more strongly with the counterpropagating laser beam, because at a certain point x' the corresponding hyperfine level will be shifted closer to resonance, while the other transition will be shifted further out of resonance. This causes a force that always pushes the atom back to the centre of the trap. The situation is reversed on the other side of the trap, with the roles of $M_e = \pm 1$ inverted, but again the atoms will be driven towards the centre of the trap.

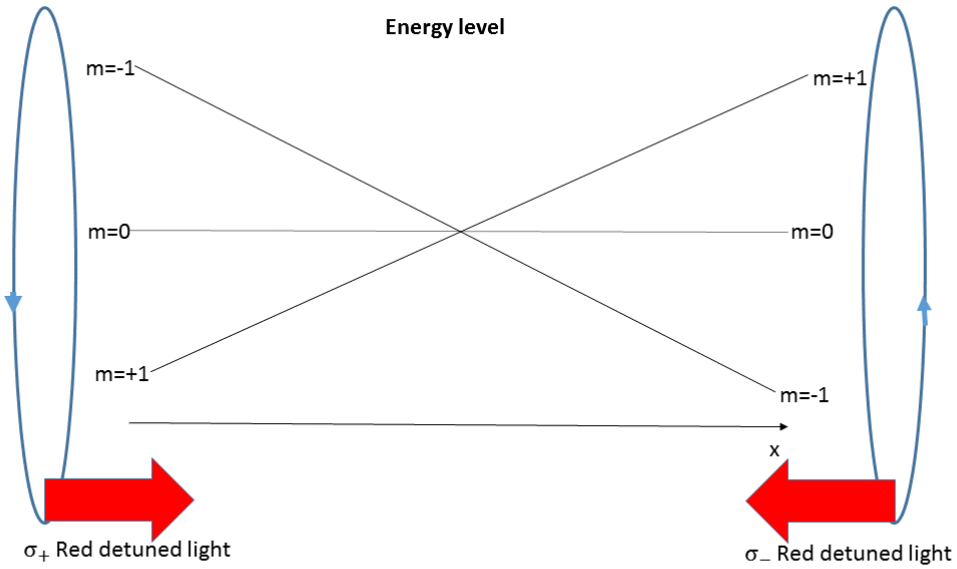

Figure 4.5: 1D model of the magneto-optical trap for atoms with a $J_e = 1$. The inhomogeneous magnetic field shifts the Zeeman sublevels of the excited hyperfine state causing a restoring light force towards the trap centre. Atoms moving to the right interact more strongly with the σ_- light beam moving to the left, and atoms moving to the left are pushed back by the σ_+ light approaching from the right. Redrawn from [33].

The situation is a perfect analogy of velocity damping in optical molasses described in the previous section. However, here the effect is in position space rather than in

velocity space. This gives rise to both a velocity and positional dependent force that can, at the same time, cool the atoms and compress the atom cloud at the centre of the trap.

4.5.1 Forces in an MOT

The magneto-optical force can be described by the same relation used for optical molasses in eq. 4.25 with a value of detuning modified by the presence of the Zeeman shift induced by the magnetic field. Therefore, the total force on the atom is given by $\vec{F} = \vec{F}_+ + \vec{F}_-$, where

$$\vec{F}_\pm = \pm \frac{\hbar \vec{k} \gamma}{2} \frac{s_0}{1 + s_0 + 2(\delta_\pm/\gamma)^2} \tag{4.27}$$

and the detuning for each laser beam is modified as

$$\delta_\pm = \delta \mp \vec{k} \cdot \vec{v} \pm \mu' B/\hbar, \tag{4.28}$$

in which μ' is the effective magnetic moment for the transition used and is given by

$$\mu' = (g_e M_e - g_g M_g)\mu_B, \tag{4.29}$$

where g_e, g_g are the Landé g factors for the excited and ground state respevtively and M_g and M_e are the magnetic quantum numbers. It is possible to see that when both the Doppler shift $\omega_D = -\vec{k} \cdot \vec{v}$, and the Zeeman shift, $\omega_Z = \mu' B/\hbar$, are small compared to the detuning, δ, the denominator of the force expressed in eq. 4.27 can be expanded. Then the force, for small velocities and around the MOT centre, becomes

$$\vec{F} \approx -\beta \vec{v} - \kappa \vec{r}, \tag{4.30}$$

where the damping coefficient β is defined in eq. 4.26, while κ is a spring constant given by

$$\kappa = \frac{\mu' B'}{\hbar k} \beta. \tag{4.31}$$

The force in 4.30 causes damped harmonic motion of the atoms with an oscillation frequency $\omega_{MOT} = \sqrt{\kappa/M}$ given by the spring constant and the mass of the atoms.

4.6 Summary

This chapter has described:

- The theory of the Zeeman effect.
- The most common types of magnetic traps.

- The different forces acting on an atom when this interacts with an electric field generated by lasers.
- The expression of the scattering force when two lasers beams are considered: the optical molasses.
- The scheme of a magneto-optical trap together with the forces exerted on an atom in the MOT.

These topics provide an insight into the theory behind the magnetic traps and the magneto-optical traps, to better understand the work presented in Chapter 5 and Chapter 6. In particular, the expression of the magnetic field of the quadrupole trap is useful to understand the work done on the concentric coil device with the Comsol multiphysics software, described in Chapter 5. Also, the extended discussion of the forces exerted on an atom in the MOT is necessary to appreciate how the expression of the force has been modified, in Chapter 6, to take into account more realistic effects.

Chapter 5

Comsol design of concentric coil devices

5.1 Prototypes of coil based devices

The magnetic trap, as explained in the previous chapter, is a fundamental component of all sensors based on cold atoms, including the quantum gravity sensors that are of interest in this research. Therefore, despite the different geometries proposed over the years, there is still interest in designing new prototypes of magnetic trap devices (i.e. magnetic field-producing structures) whose size, weight and power consumption are optimised for integration in quantum sensors. In this study, the geometry of a coil-based device has been considered as a first step for the construction of MOT allowing potentially easy access of optical components and maintaining a compact size of the device.

This chapter describes the work done with Comsol Multiphysics software to design a concentric coil with geometric properties inferred from an optimisation method developed by Dr. Nathan Welch at University of Nottingham. After a brief description of the optimisation method used to obtain the geometry of the device, the model will be described and a comparison made between the magnetic field determined from the Comsol numerical software and Dr. Welch's analytical expressions. Finally, a study of the heating, stress, strain, and temperature produced with such a device will be presented.

5.1.1 Concentric coil optimisation

The geometry of the magnetic trap has been considered in order to create a "quadupole field" that follows the general form:

$$\mathbf{B} = B'x\hat{\mathbf{x}} + B'y\hat{\mathbf{y}} - 2B'(z - z_0)\hat{\mathbf{z}}, \tag{5.1}$$

where B' represents the gradient of the field and z_0 is the height of the centre of the trap. The focus of the design was to create this quadrupole field with a device consisting of four concentric coils of conducting material having different radii and

thicknesses. If the coils lie in the x-y plane and the origin of the axis $(0, 0, 0)$ is taken as common centre of the coils, z_0 is located above the coils.

Since the four coils in the device are connected to each other, the outer radius of a certain coil will correspond with the inner radius of the next coil. Therefore, the device can be defined by 5 radial values r_1, r_2, r_3, r_4, r_5 and 4 values of thickness (extent of the coils in the z direction) for each coil z_1, z_2, z_3, z_4.

In order to obtain the desired quadrupole magnetic field, optimal radial values, and thicknesses and optimal current densities for each coil, J_1, J_2, J_3, J_4 need to be selected. To find these values an iterative point method is used to optimise the radii and thicknesses and, for each iteration of these dimensions, an inverse method is used to solve for the optimal current density in each coil. Every optimized configuration of radii, thickness and current densities, gives a magnetic field through the Biot-Savart law.

The performance of the device is defined as the root-mean-square relative difference between the desired magnetic field and the field created by the device plus the total power dissipated due to Joule heating. To quantify this performance a cost function is defined as

$$\Phi = \frac{1}{2}\left(\frac{RMS\,relative\,error}{desired\,error} + \frac{Power}{desired\,Power}\right). \tag{5.2}$$

This cost function, that the optimisation method tries to minimize, consists of two terms: the first one is the mean of the field error divided by a desired error and the second is the power of the device divided by some specified desired power. With this optimisation method both the dimensions of the coils and the currents flowing in each coils are optimised and contribute to the creation of an optimal device.

Some constraints are added to the minimisation problem. This is necessary to limit the total dimension of the device, therefore a constraint is set on the maximum value of the outer radius r_5 as well as on the possible thicknesses of the coils in z. Moreover, since the final objective is to build a magnetic trap that allows optical access through the centre of the device, a constraint on the minimum value of the inner radius r_1 is added as well.

The values of radii, thicknesses and currents selected from this optimisation method have been used to build the concentric coils model with Comsol Multiphysics software. This was done in order to validate the magnetic field profile obtained from the optimisation method and, also, to have insights about the temperature, heating and stress distribution in the device.

5.1.2 Comsol concentric coils model

Comsol Multiphysics is software developed to model and simulate physics-based problems in a finite-element modelling environment. Because of this software 'multiphysics capability' it is possible to simultaneously solve different physical equations for the same model geometry. Given the necessity in this study to model coils and obtain the magnetic profile as well as temperature, heating and stress, the AC-DC module of Comsol with a magnetic field user interface was used.

The model was built in 3D as 4 different concentric rings, each having a rectangular cross section. The values of inner and outer radius and of the thickness of each

coil were specified by the values obtained by the optimization method (table 5.1). The whole device was built on the $x - y$ plane with the axes origin corresponding to the common centre of the coils. In particular, each ring was built in a plane geometry and then extruded in the $z < 0$ direction to take into account the different thicknesses of each coil. The material used for the device was copper and, in the Comsol model, it was surrounded by a sphere of air having a much greater radius than the outer radius r_5 in order to make the boundaries not too close to the bulk of the copper wires. A top and a side view of the device without the surrounding air are shown in fig.5.1 and fig. 5.2.

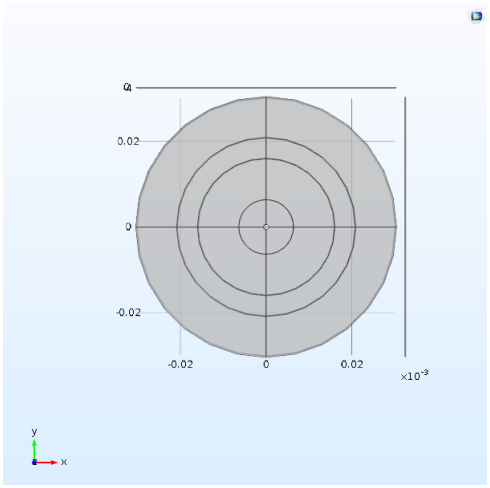

Figure 5.1: Top view of the geometry of the copper device, with inner and outer radii and thicknesses inferred from the optimisation method.The axes are in metres, and the air domain has been removed from the plot. Cross shows axes rather than a physical feature in the coils modelled.

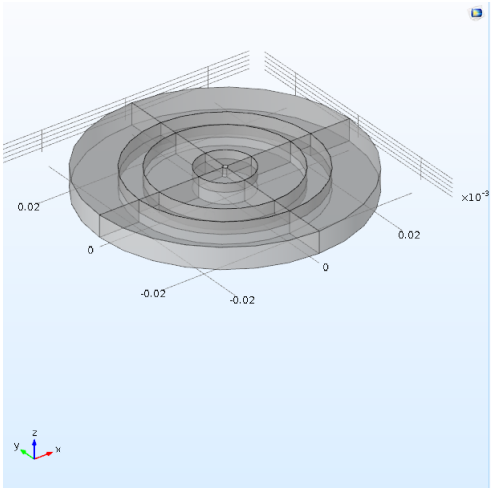

Figure 5.2: Side view of the geometry of the copper device, with inner and outer radii and thicknesses inferred from the optimisation method. The axes are in metres, air domain has been removed from the plot.

Once the geometry and the material properties were defined, the magnetic field interface was used in order to simulate the coils. Since the interest was in exciting

the coils with a direct current and simulating a homogeneous distribution of current density, each coil was modelled with a multi-turn coil node already available in the Comsol magnetic field interface. In fact, the multi-turn coil feature is tailored to simulate the presence of multiple windings and assumes that the current density is uniform throughout the coil's cross section and flows in a certain direction specified by the geometry (chirality) of the coil.

Since no information regarding the number of turns can be inferred from the optimisation method presented before, but the number of turns can modify the resistance of the device, the number of turns in each coil have been determined by setting the value of the applied voltage. Once the total voltage has been fixed, and considering the coils to be connected in series, through Ohm's law it is possible to determine the four values corresponding to the number of turns in each coil N_1, N_2, N_3, N_4 by trial and error (table 5.1). In a subsequent version of the optimisation method, the information about the optimal number of turns is integrated in the process by adding the information about the total voltage and minimizing for this additional term.

Since the Comsol Multiphysics software works in a finite element modelling environment, in order to obtain a solution for the magnetic field produced by this device, a mesh needs to be defined. Different studies have been conducted starting from a coarse mesh to a finer mesh, leading to the set of results that will be shown in the next section.

Geometry of the device				
Parameters	Coil 1	Coil2	Coil 3	Coil4
Inner radius (m)	0.0005821	0.0063	0.0158	0.0206
Outer radius (m)	0.0063	0.0158	0.0206	0.03
Thickness (m)	0.002	0.0047	0.0028	0.005
Current (A)	111.4858	-222.1667	-2.3392	171.4222
Turns, N	315	627	7	484

Table 5.1: Parameters used for the modelling of the device

5.2 Comparison of Comsol results for the magnetic field with analytical solutions

Once the device geometry, the boundary conditions and the mesh were fixed, a magnetic field prifle was obtained from Comsol. The next step in the analysis, therefore, was to compare the magnetic field obtained from Comsol with the analytical form of the magnetic field obtained by integrating over the thickness of each coil, through the Newton-Coles rules. The closed-form formulas for three Cartesian components of the magnetic induction of a circular loop carrying a static current can be written

in the form

$$
\begin{aligned}
B_x &= \frac{Cxz}{2\alpha^2\beta\rho^2}[(a^2+r^2)E(k^2)-\alpha^2K(k^2)] \\
B_y &= \frac{Cyz}{2\alpha^2\beta\rho^2}[(a^2+r^2)E(k^2)-\alpha^2K(k^2)] = \frac{y}{x}B_x \\
B_z &= \frac{C}{2\alpha^2\beta}[(a^2-r^2)E(k^2)+\alpha^2K(k^2)],
\end{aligned}
\tag{5.3}
$$

where $C = \frac{\mu_0 I}{\pi}$ (with I the current flowing in the loop), a is the radius of the current loop (which is in the $x-y$ plane), $r^2 = x^2+y^2+z^2$, $\rho^2 = x^2+y^2$, $\alpha^2 = a^2+r^2-2a\rho$, $\beta^2 = a^2+r^2+2a\rho$ and $k^2 = 1-\frac{\alpha^2}{\beta^2}$. These closed formulations are exact everywhere in space but they require numerical evaluation of the elliptic integrals of the first and second kind ($E(k^2)$ and $K(k^2)$) [38]. Once integrated over the dimensions of each coil, the different magnetic field contributions from the det of coils are added together to obtain the magnetic field of the whole device.

This is also the way in which the magnetic field is calculated and included in the objective function to minimise. Therefore, agreement between the magnetic field obtained by integration of these closed formulas and the magnetic field obtained by simulating the model in Comsol, validates the use of the former in the optimisation method.

In Figures 5.3- 5.8, comparison between the fields obtained from integrating the closed formulas and the magnetic field obtain with Comsol (setting both a coarse and a fine mesh) is presented. In each case red curves show the "analytic solution" while blue curves show the "Comsol solution".

It is clear from the plots, that the agreement between the solutions obtained with the use of the Comsol software and by integration of the analytic expressions (5.3) for the magnetic field of a circular current loop, improves when a finer mesh is used for the model. This is particularly visible by comparing figures 5.5 and 5.6 for the B_x component and figures 5.7 and 5.8 for B_y.

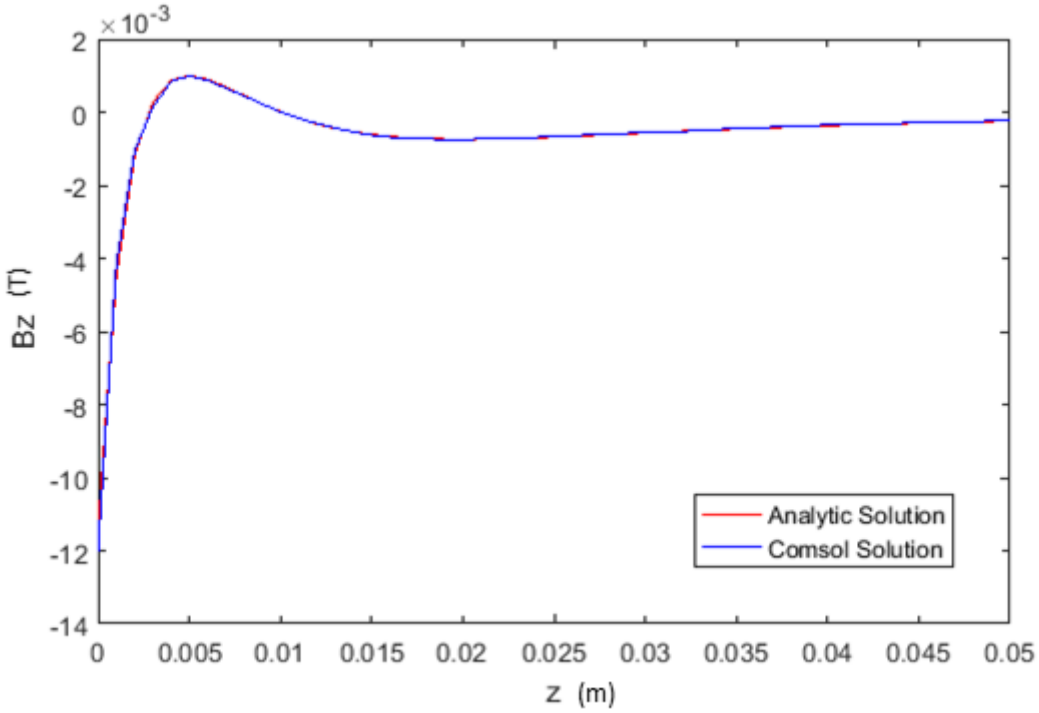

Figure 5.3: B_z calculated as a function of z with $x = y = 0$. Red curve shows the "Analytic solution" while the blue curve shows the "Comsol solution". The B_z component of the magnetic field has been obtained from the Comsol model setting a coarse mesh.

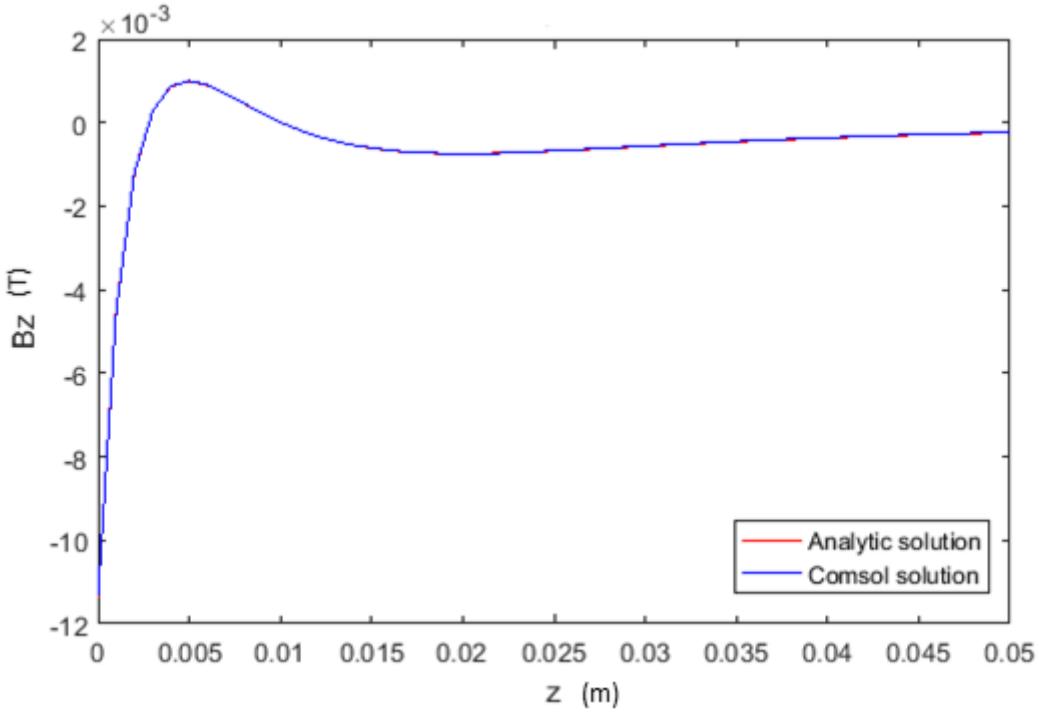

Figure 5.4: B_z calculated as a function of z with $x = y = 0$. Red curve shows the "Analytic solution" while the blue curve shows the "Comsol solution". The B_z component of the magnetic field has been obtained from the Comsol model setting a fine mesh.

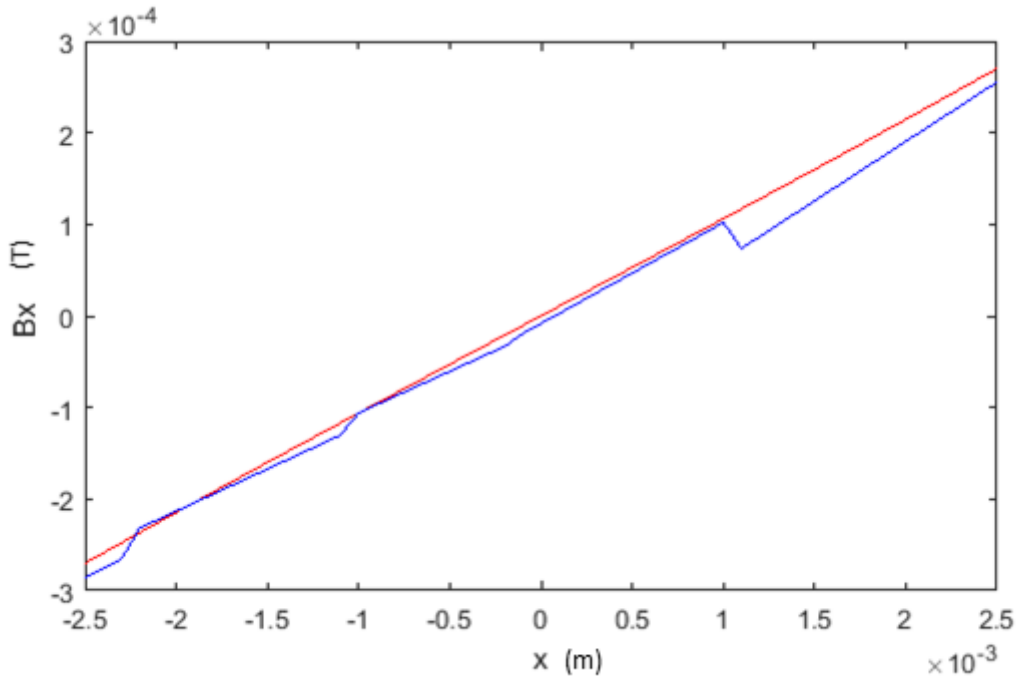

Figure 5.5: B_x calculated as a function of x with $y = 0$ and $z = z_{trap}$, where z_{trap} represents the z coordinate for which B_z vanishes. Red curve shows the "Analytic solution" while the blue curve shows the "Comsol solution". The B_x component of the magnetic field has been obtained from the Comsol model setting a coarse mesh.

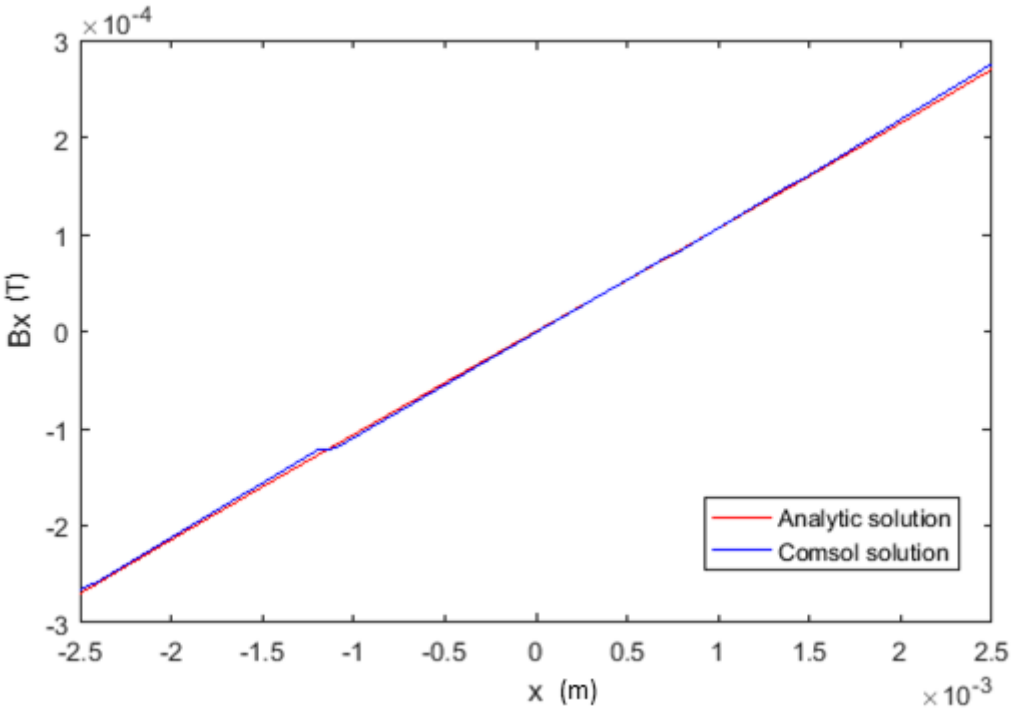

Figure 5.6: B_x calculated as a function of x with $y = 0$ and $z = z_{trap}$, where z_{trap} represents the z coordinate for which B_z vanishes. Red curve shows the "Analytic solution" while the blue curve shows the "Comsol solution". The B_x component of the magnetic field has been obtained from the Comsol model setting a fine mesh.

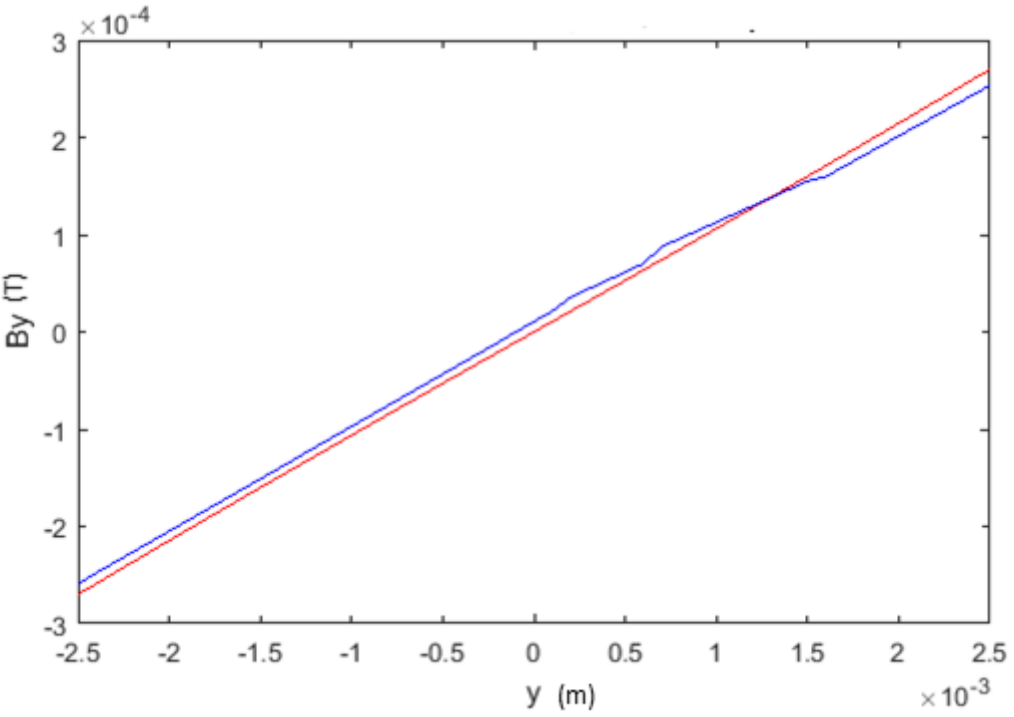

Figure 5.7: B_y calculated as a function of y with $x = 0$ and $z = z_{trap}$, where z_{trap} represents the z coordinate for which B_z vanishes. Red curve shows the "Analytic solution" while the blue curve shows the "Comsol solution". The B_x component of the magnetic field has been obtained from the Comsol model setting a coarse mesh.

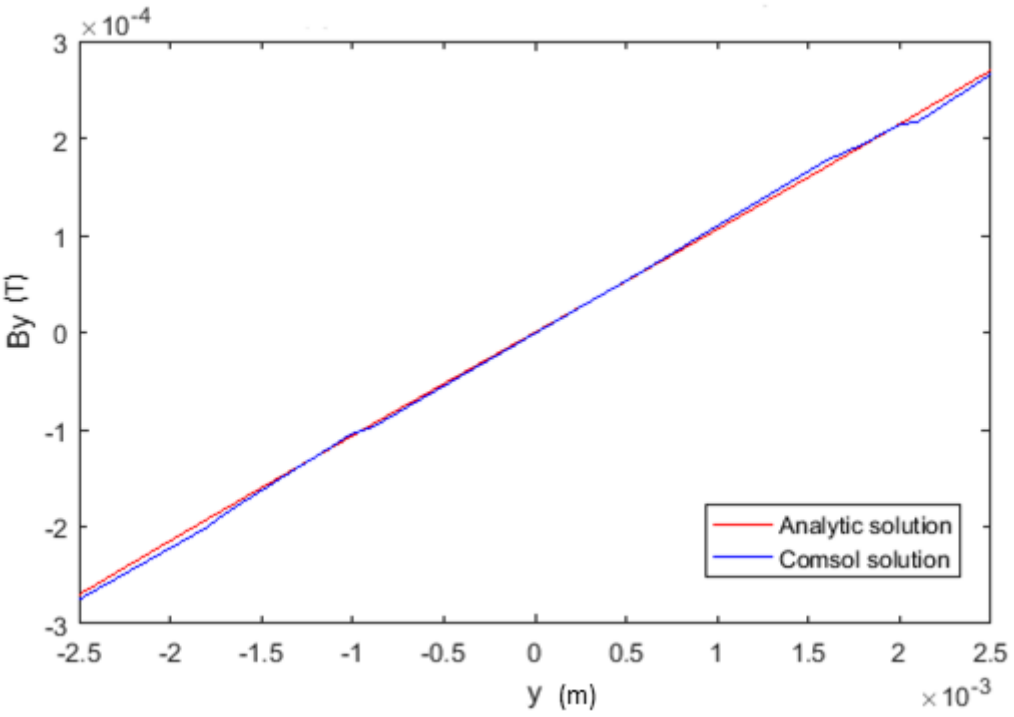

Figure 5.8: B_y calculated as a function of y with $x = 0$ and $z = z_{trap}$, where z_{trap} represents the z coordinate for which B_z vanishes. Red curve shows the "Analytic solution" while the blue curve shows the "Comsol solution". The B_x component of the magnetic field has been obtained from the Comsol model setting a fine mesh.

5.3 Study of heating, stress and temperature produced by the device

As already mentioned, the Comsol software is a multiphysics platform that allows different kinds of study on the same model geometry. This capability is extremely useful in this study, because no information about the possible heating, stress and temperature produced by the device is supplied by the optimisation method. However, it is important to obtain this information before manufacturing such a device. Therefore, once it was established that the magnetic field profile calculated from Comsol was comparable to what was expected from the analytical model, it was possible to compute the heating produced within the Comsol model. The heating is measured in $\frac{\mathrm{W}}{\mathrm{m}^3}$. Higher values of heating are found in the inner coil (fig.5.9) with a maximum of $1.6 \times 10^6 \frac{\mathrm{W}}{\mathrm{m}^3}$. The lowest value of heating is found in the third coil, because the current flowing in this coil is negligible compared with those flowing in other coils (see table 5.1). The electromagnetic heating generates an increment in the temperature of the device, which is analysed in a time dependent study described below.

At this point the Maxwell stress tensor is calculated. In the Comsol software, this is computed through the Lorentz forces produced by one loop on the other. All the force components are shown in figures 5.10, 5.11 and 5.12. Plots of the stress components are shown in fig 5.13, 5.14 and 5.15. Note that the alternating negative and positive regions are inverted in these images with respect to the relative Lorentz force components. This happens because of the convention chosen for the direction of the stress (positive values correspond to the normal direction to the surface).

Rather then commenting in detail the results obtained for the Lorentz forces and the stress, it is more useful to look at the overall strain generated in the device. The equations for the strain are not already available in Comsol, therefore, the different components have been calculated from the stress using the following equations:

$$\begin{aligned} \epsilon_{xx} &= \frac{1}{E}(\sigma_{xx} - \nu\sigma_{yy} - \nu\sigma_{zz}) \\ \epsilon_{yy} &= \frac{1}{E}(-\nu\sigma_{xx} - \nu\sigma_{zz} + \sigma_{yy}) \\ \epsilon_{zz} &= \frac{1}{E}(-\nu\sigma_{xx} - \nu\sigma_{yy} + \sigma_{zz}), \end{aligned} \tag{5.4}$$

where E is the *Young modulus* having a value of 117GPa for copper and ν is the *Poisson ratio* with a value of 0.355 for copper. Plots of the strain defined as the change in length ΔL per unit original length L are shown in figures 5.16, 5.17 and 5.18. These figures show that the device is subject to a tension when a positive stress is applied and to a compression if a negative stress is present. The strain is of the order of 10^{-9} for usual operating conditions, i.e. negligibly small.

In order to quantify the temperature of the coils in operation, a time dependent analysis was done considering the electromagnetic heating calculated in the stationary analysis as a heat source and an initial temperature of 293.15 K. The final time was set to 30 s, which could be considered a realistic working cycle for a magnetic

trap. Figure 5.19 shows that higher values of temperature are found in the inner coil with a maximum value of 295.63 K. It is important to stress that more realistic thermal simulations can be run in which the device is in thermal contact with a specific heat sink material and longer time cycles are considered; this is beyond the aim of this initial study where the device is surrounded by air and taken to be self standing.

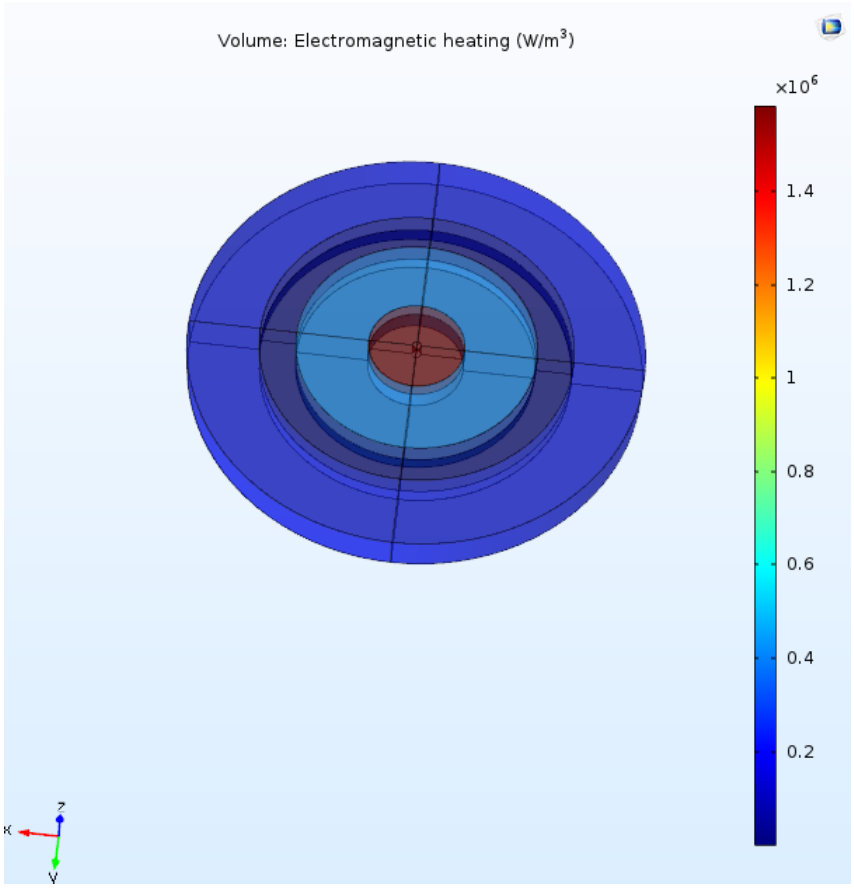

Figure 5.9: Heating profile of the device. Higher values of $1.6 \times 10^6 \frac{\mathrm{W}}{\mathrm{m}^3}$ can be found in the inner coil, while the third coil does not contribute because the current in this coil is negligible compared with those of the other coils (table 5.1).

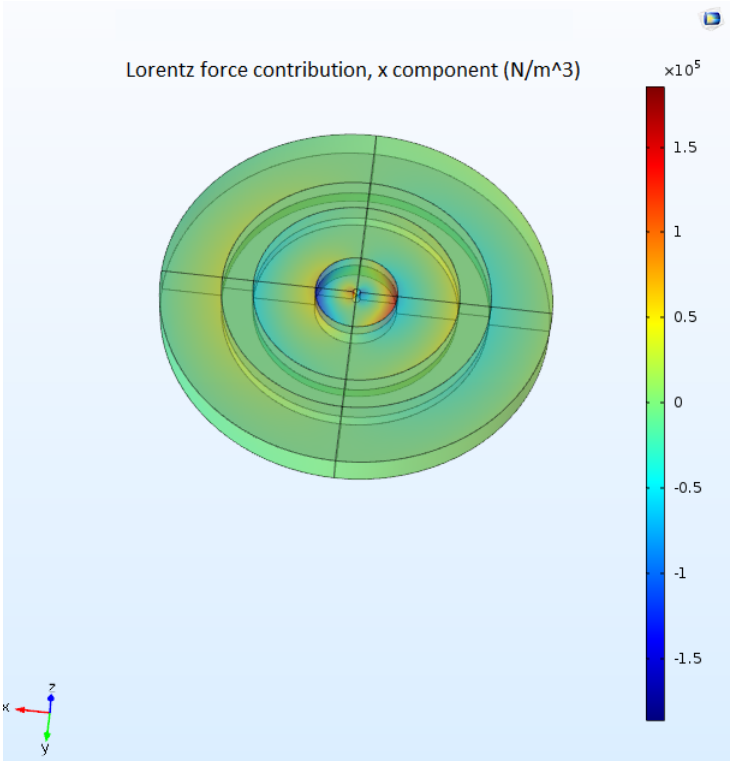

Figure 5.10: x component of the Lorentz force. The highest negative and positive values are visible at the boundary between the first and second coil (note that the currents flow in opposite directions in these two coils).

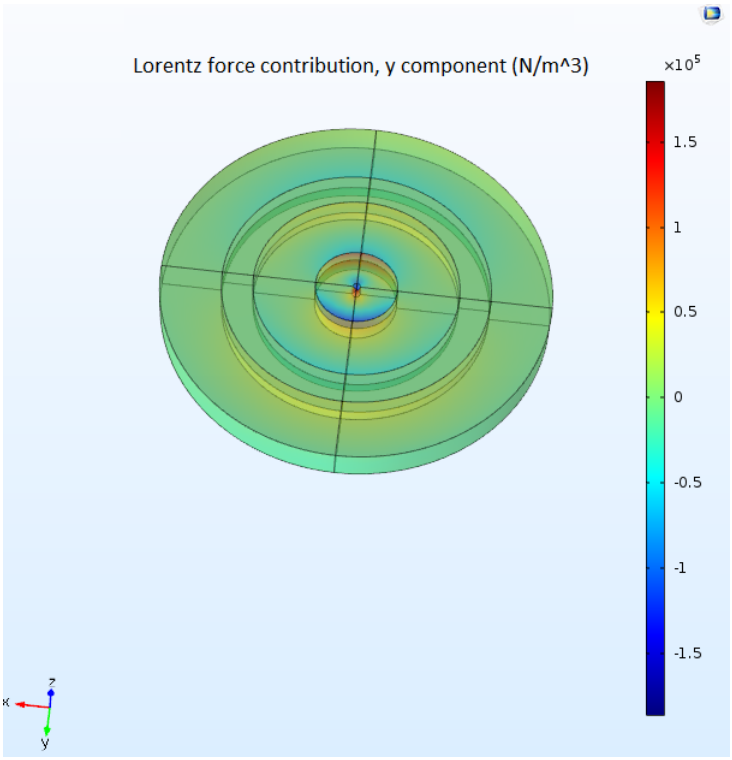

Figure 5.11: y component of the Lorentz force. The highest negative and positive values are visible at the boundary between the first and second coil (note that the currents flow in opposite directions in these two coils).

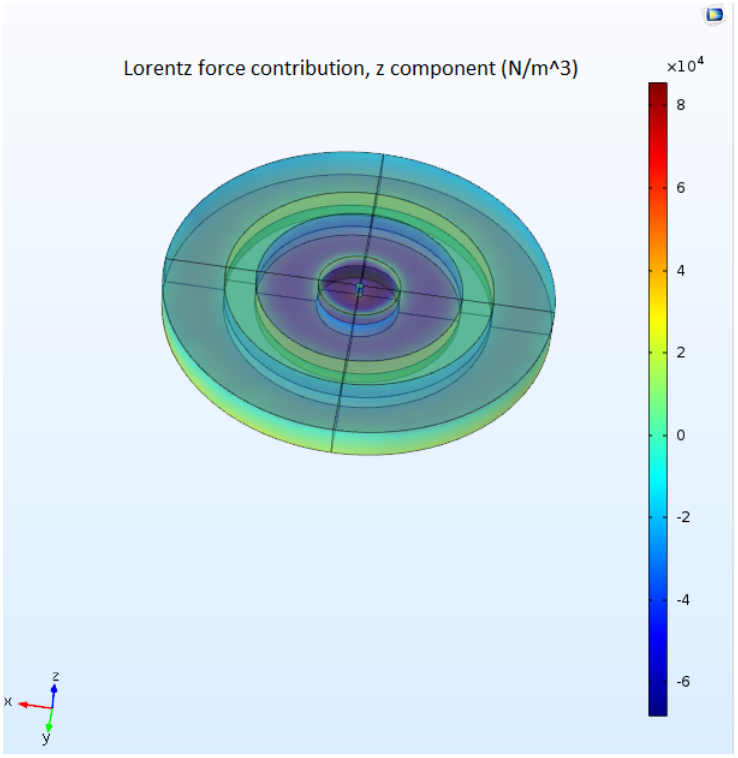

Figure 5.12: z component of the Lorentz force. The highest negative values are visible on the top surface of the inner coil. Increasing positive values are found moving along the z axis towards the bottom of the device.

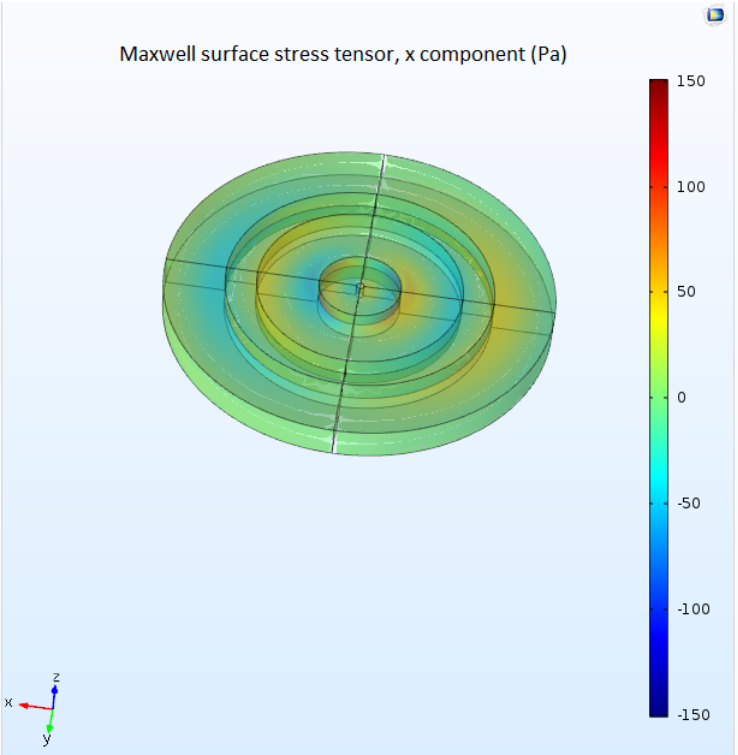

Figure 5.13: x component of the stress tensor measured in Pascal. The distribution of stress resembles the distribution of the x component of the Lorentz force with the negative and positive regions reversed. This is because of the convention chosen for the direction of the normal stress.

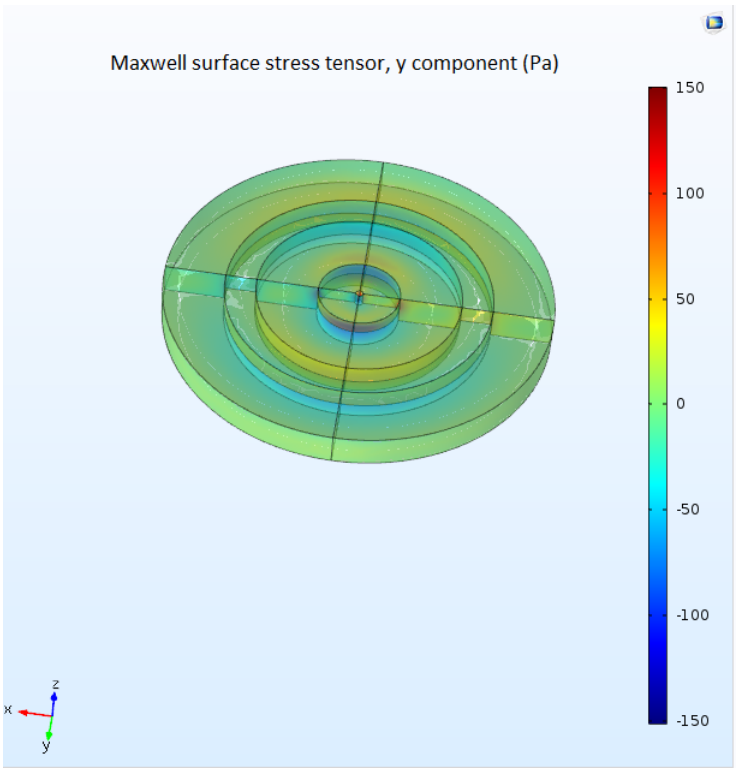

Figure 5.14: y component of the stress tensor measured in Pascal. The distribution of stress resembles the distribution of the y component of the Lorentz force with the negative and positive regions reversed. This is because of the convention chosen for the direction of the normal stress.

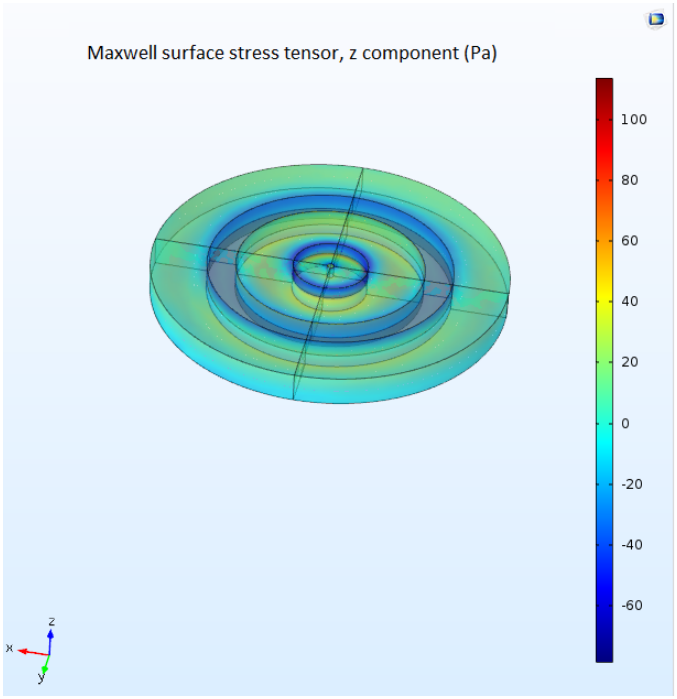

Figure 5.15: z component of the stress tensor measured in Pascal. The distribution of stress resembles the distribution of the z component of the Lorentz force with the negative and positive regions reversed. This is because of the convention chosen for the direction of the normal stress.

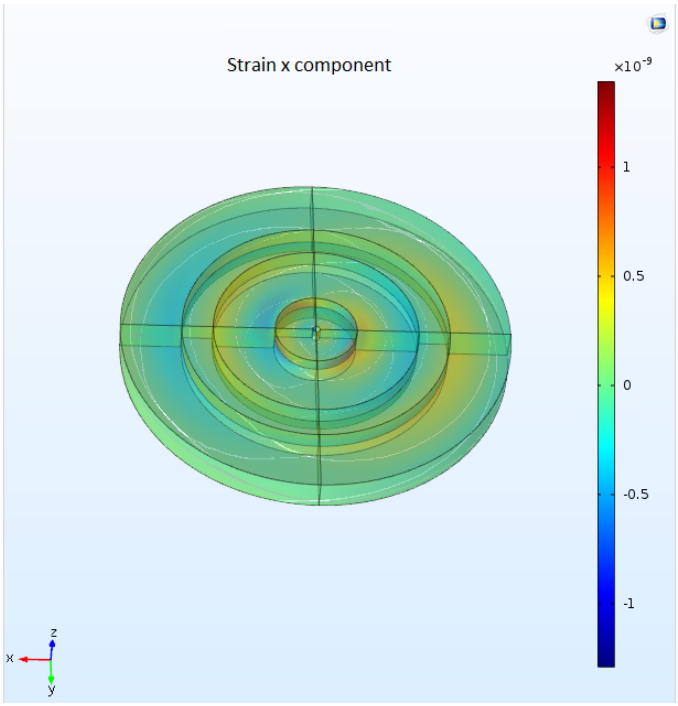

Figure 5.16: x component of the normal strain. The distribution of the strain resembles the distribution of the x component of the stress with regions of tension (positive stress, positive strain) and compression (negative stress, negative strain). All the values are of the order of 10^{-9}, therefore negligible.

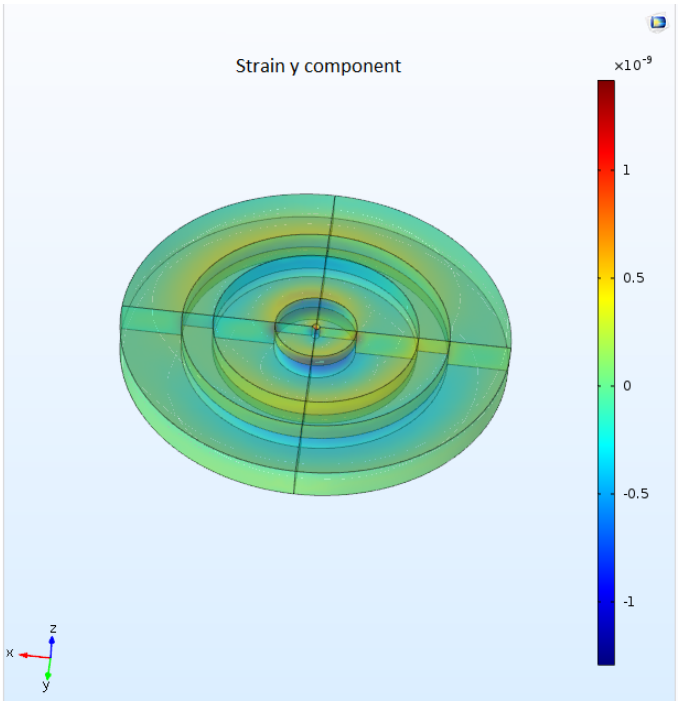

Figure 5.17: y component of the normal strain.The distribution of the strain resembles the distribution of the y component of the stress with regions of tension (positive stress, positive strain) and compression (negative stress, negative strain). All the values are of the order of 10^{-9}, therefore negligible.

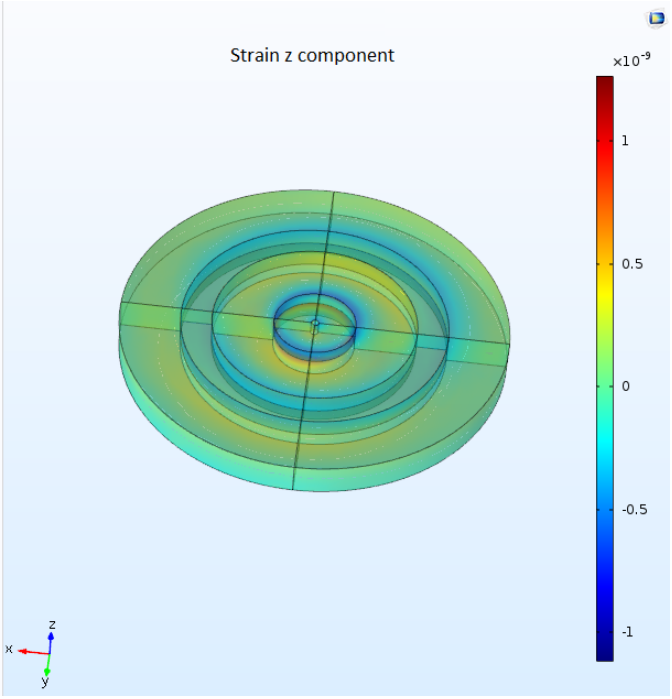

Figure 5.18: z component of the normal strain.The distribution of the strain resembles the distribution of the z component of the stress with regions of tension (positive stress, positive strain) and compression (negative stress, negative strain). All the values are of the order of 10^{-9}, therefore negligible.

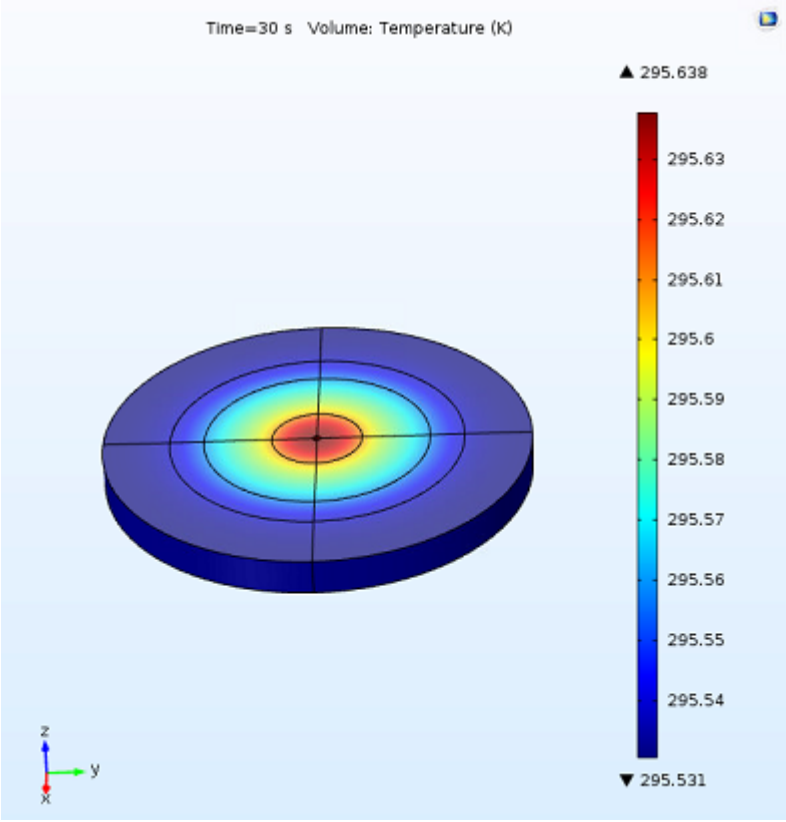

Figure 5.19: Temperature of the device. The device reaches a maximum temperature of 295.63 K in the inner coil. after 30 s of operation.

5.4 Results and future perspectives

Through the Comsol simulations of the concentric coil device it has been possible to validate the magnetic field profile obtained with the optimisation method (showing that there is agreement between the magnetic fields obtained with the two differents methods) and to obtain additional information about temperature, heating, stress and strain which were not available using the analytical model used for the optimisation. In particular, this numerical study has been important for manufacturing a protoype of this device with similar dimensions, currents and number of turns showing that, in future, this could be used as a reliable magnetic trap.

The interest is, currently, in integrating such a magnetic trap with optical and UHV components so as to make a full magneto optical trap. For this reason, a simulation of the dynamics of atoms in a magneto optical trap was performed and will be presented in the next chapter.

5.5 Summary

This chapter has described:

- The optimisation method that has provided the parameters for the design of the concentric coil device, together with the model implemented using the Comsol multiphysics software.
- The comparison of the magnetic field obtained from Comsol and that obtained with closed analytical formulations.
- A study of the heating, stress and temperature profile produced by the device.
- The future perspectives of this work.

These sections describe the different phases of the study of a concetric coil device with an optical access, that could be potentially used as a magneto optical trap. In addition to the description of the the optimisation method developed by Dr. Nathan Welch at the University of Nottingham that provided the geometry of the device and the current densities in each coil, it has been shown how the model of the device was implemented in the Comsol multiphysics software. In particular, it is described how the use of Comsol was essential to study and to compare the magnetic field and the heating, stress, strain and temperature profile produced by such a device.

Chapter 6

Numerical modeling of a 3D MOT

The work done with the Comsol multiphysics software discussed in the previous chapter has shown that it is possible to obtain a quadrupole magnetic field with a device that is optimised for specific dimensions and the power consumption constraints. Moreover, the geometry of the device has been specifically chosen to allow optical access and, therefore, the eventual construction of a 3D MOT.

Since the optimisation method, used to obtain the optimal magnetic trap, has proved to be efficient and reliable, the objective is to adopt the same approach for the study of 3D MOTs, possibly adding further terms in the objective function to minimise. In order to do this, a more realistic description of a magneto-optical trap needs to be considered to allow more parameters to vary in the optimisation process. This is a necessary initial step for the development of this kind of technique. Therefore, this chapter presents an analysis of the MOT forces when multiple level atoms and other effects, such as the profile of the laser beams, are taken into account. It also shows how the resulting atomic dynamics can be implemented in a numerical model of a 3D MOT for ^{87}Rb atoms.

6.1 Forces for multi-level atoms in MOT

In Chapter 4, the total force acting on an atom in MOT was described, treating the atom as a two-level system. In reality, atoms are multi-level systems. Therefore, in a complete simulation of a 3D MOT, all the possible transitions between the sublevels should be considered. Moreover, for an exhaustive approach, also the Gaussian profiles of the laser beams and the angle between the direction of the magnetic field and the direction of the light also need to be taken into account [39].

The first to propose this approach were *Lindquist et al.* [40] who introduced an expression for the total slowing force in one dimension resulting from summation over all the possible forces produced by each transition. This expression can be easily generalized to a 3D configuration and different possible trap geometries, as shown by *Chough et al.* [41] for an axiconic MOT.

If a generic $F_g \rightarrow F_e$ transition, a $\sigma_+ - \sigma_-$ laser light polarization, and a quadrupole magnetic field, $\mathbf{B(r)}$, are considered, the Zeeman shift of the atom's energy, at a

position $\mathbf{r} = (x, y, z)$, is:

$$\delta_{mF_g}^{\Delta m} = \frac{\mu_B |\mathbf{B}(\mathbf{r})|}{\hbar}[(mF_g + \Delta m)g_e - mF_g g_g], \tag{6.1}$$

where μ_B is the Bohr magneton as defined in Chapter 4, and g_g and g_e are the Lande g factors of the particular transition. Moreover, given that the magnetic field profile and the direction of the light propagation are not parallel at all points, the angular momenta of the circularly polarized lasers are locally rotated in the basis of the quantization axis (the direction of the magnetic field at each position $\mathbf{r}$). Therefore, the transitions $\Delta m = -1, 0, 1$ are all driven by a fraction of the light given by [41, 42, 43]:

$$\begin{aligned} P_{\sigma\pm}^{\Delta m=\pm 1} &= (\frac{1 \pm \Delta m cos\theta}{2})^2 \\ P_{\sigma\pm}^{\Delta m=0} &= \frac{sin^2\theta}{2}, \end{aligned} \tag{6.2}$$

where the angle θ is defined by the local magnetic field direction and the wavevector $\mathbf{k}$ of the light as

$$cos\theta = \frac{\mathbf{B}(\mathbf{r}) \cdot \mathbf{k}}{|\mathbf{B}(\mathbf{r})|k}. \tag{6.3}$$

If the probability for each transition is given by the square of the Clebsch- Gordan coefficients $C_{mF_g}^{\Delta m}$, $I(\mathbf{r})$ is the light intensity spatial variation, and I_S is the saturation intensity of the transition, the total scattering force acting on each atom in a 3D MOT with six laser beams can be expressed as

$$\begin{aligned} \mathbf{F}^S = \sum_{i=1}^{6} \frac{\hbar \mathbf{k} \gamma}{2} \sum_{m_f=-F_g}^{F_g} \sum_{\Delta m=-1}^{\Delta m=+1} P_{\sigma\pm}^{\Delta m=0,\pm 1} |C_{mf}^{\Delta m}|^2 \frac{I(\mathbf{r})}{I_S} \\ \times (\frac{1}{1 + I(\mathbf{r})/I_S + [2(\delta - \delta_{mF_g}^{\Delta m} \mp \mathbf{k} \cdot \mathbf{v})/\gamma]^2}, \end{aligned} \tag{6.4}$$

where γ is the natural linewidth, δ is the laser detuning and $\mathbf{v}$ is the velocity of the atom.

In this expression of the force, all the elements of interest are included: the multiple level description of the atoms, the spatial dependance of the intensity of the laser beams, $I(\mathbf{r})$, which allows the inclusion of their Gaussian profiles, and the angle defined in eq. 6.3.

6.2 Implementation of the model for a ^{87}Rb 3D MOT

Once a realistic expression for the force in MOT was obtained, a numerical model to calculate this force was developed in MATLAB. The basic idea was to study atomic motion within a 3D MOT of ^{87}Rb atoms, where the latter are exposed to the force discussed in the previous section.

The cooling transition used is $5^2S_{1/2}, F_g = 2 \rightarrow 5^2P_{3/2}, F_e = 3$ and all the parameters for this transition can be found in Appendix A. A six laser beam geometry has been simulated with the conventional $\sigma_+ - \sigma_-$ light polarization (fig.6.1) and a magnetic field gradient of $10\frac{\mathrm{G}}{\mathrm{cm}}$. As already mentioned,the beams can be described by a Gaussian profile and, if a beam waist radius, r_w, of a few cm is considered, it is possible to define the capture velocity $v_c = \sqrt{\frac{2\hbar k\gamma r_w}{M}}$. This capture velocity is the maximum velocity at which the atoms can be trapped in the MOT.

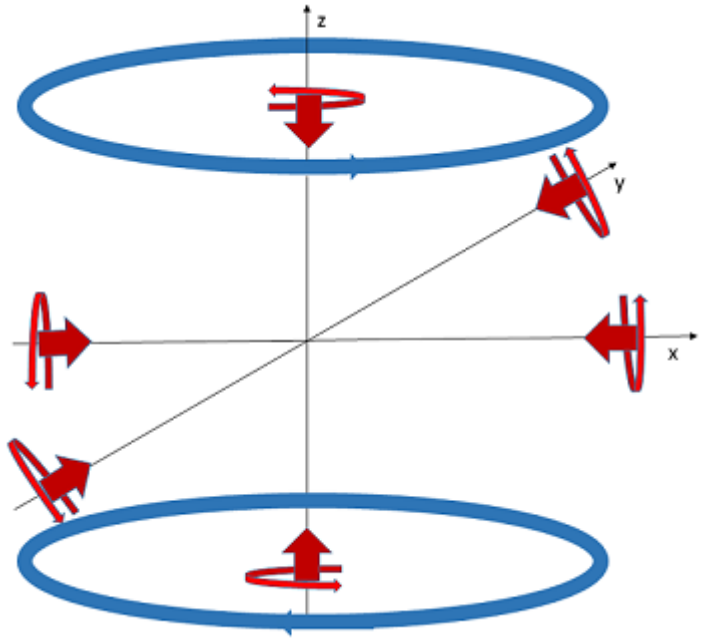

Figure 6.1: Typical geometry of a six laser beam MOT using two coils of opposite currents to generate the magnetic field. The propagation direction and circular polarization of each beam are indicated by the wide and narrow red arrows respectively.

The non-uniform intensity distributions of the laser beams field components are

given by:

$$
\begin{aligned}
I_x(y,z) &= I_0 \exp\left(-\frac{y^2+z^2}{r_w^2}\right) \\
I_y(x,z) &= I_0 \exp\left(-\frac{x^2+z^2}{r_w^2}\right) \\
I_z(x,y) &= I_0 \exp\left(-\frac{x^2+y^2}{r_w^2}\right)
\end{aligned}
\qquad (6.5)
$$

,

where I_0 is the peak intensity. In order to take into account the realistic cut-off of the laser beams, a cut-off radius was set to $r_t = 0.01$m and the Gaussian intensity profiles of the laser beams were implemented in the simulation in the following way:

$$
\begin{aligned}
I_x(y,z) &= \begin{cases} I_0 \exp\left(-\frac{y^2+z^2}{r_w^2}\right) & \text{for } y^2+z^2 < r_t \\ 0 & \text{for } y^2+z^2 \geq r_t \end{cases} \\
I_y(x,z) &= \begin{cases} I_0 \exp\left(-\frac{x^2+z^2}{r_w^2}\right) & \text{for } x^2+z^2 < r_t \\ 0 & \text{for } x^2+z^2 \geq r_t \end{cases} \\
I_z(x,y) &= \begin{cases} I_0 \exp\left(-\frac{x^2+y^2}{r_w^2}\right) & \text{for } x^2+y^2 < r_t \\ 0 & \text{for } x^2+y^2 \geq r_t \end{cases}
\end{aligned}
\qquad (6.6)
$$

,

and the capture velocity was modified accordingly, replacing r_w with r_t and obtaining a value of $v_c = 67\text{ms}^{-1}$.

A Runge Kutta method of the $4^{th} - 5^{th}$ order [44] has been used in order to solve the differential equations of motion for atoms having a range of initial conditions. The calculation is performed in three dimensions considering the scattering forces in the x,y and z directions. The initial coordinates in position space varied around the trapping volume of interesection of the 3 pairs of laser beams, while for the velocity space, the initial values were chosen according to the Maxwell-Boltzmann velocity distribution.

In this simulation, only the scattering force has so far been implemented and other effects such as the diffusion and loss and load processes have not been considered yet. Some examples of the results obtained from the simulations are presented in the next section.

6.3 Comparison of the results obtained for atoms with different initial conditions

Once the force and the atoms' initial velocity and position conditions are determined, the simulation allows the time evolution of the three components of the velocity and position to be determined for each atom.

It is interesting to compare the results for atoms with different initial conditions in phase space. In particular, in order to understand the physical meaning of the results, we will consider three different plots for each atom. The first of these plots shows the ratio between the radial velocity of the atom $v_r = \sqrt{v_x^2 + v_y^2 + v_z^2}$ and the capture velocity, v_c, as a function of time. From the previous section, this plot should show that, if $v_r/v_c < 1$ the atom can be captured, while if $v_r/v_c > 1$ it can't be trapped. The second kind of plot shows the ratio between the radial position of the atom, $r_r = \sqrt{x^2 + y^2 + z^2}$, and the initial position, $r_0 = \sqrt{x_0^2 + y_0^2 + z_0^2}$, as a function of time. Such plots reveal if the specific atom is trapped at the end of the simulation, in which case r_r/r_0 decreases to zero. In the last plot type, the different trajectories of the atom in the $x - y$, $x - z$ and $y - z$ planes are shown.

Figures 6.2, 6.3 and 6.4 correspond to an atom having an initial radial velocity smaller than the capture velocity. In Fig 6.2 this ratio, starts from a value < 1, oscillates and then decreases towards zero. This behaviour shows that the atom is cooled by the lasers. Note, however, that since the diffusion effect is not simulated, the atoms can be slowed down to zero velocity. This is not the case if the diffusion term is added and the Doppler temperature limit is taken into account. Figure 6.3 shows that in addition to being cooled, the atom is also trapped because $r_r/r_0 \to 0$ as t increases. The approach to trapping can be seen directly from the projection of the atom orbits shown in fig. 6.4.

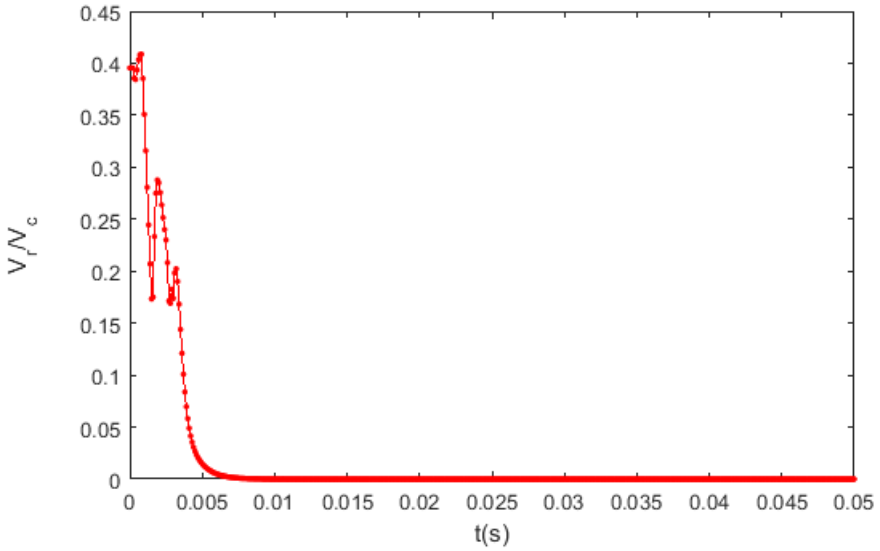

Figure 6.2: Ratio between the radial velocity v_r and the capture velocity v_c calculated as a function of time. The atom starts its motion with a velocity smaller than the capture velocity and is further slowed down.

The second example considered is an atom that starts with an initial radial velocity greater than the capture velocity. Fig. (6.5) shows that, at the end of the simulation, the atom is not slowed down below the capture velocity. Moreover, the atom is not trapped (Fig. 6.7) and leaves the MOT region with a constant velocity (Fig. 6.8).

Figures 6.8, 6.9, 6.10 show results for an atom whose initial radial velocity equals the capture velocity. Although this atom is slowed down, the ratio v_r/v_c does not approach zero, and so the atom is not trapped.

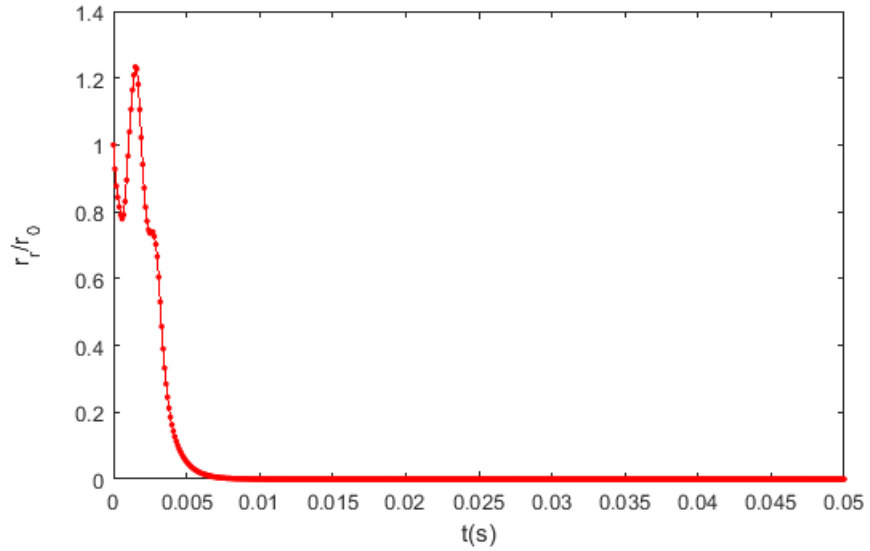

Figure 6.3: Ratio between the radial position r_r and the initial radial position r_0 calculated versus t. The atom is trapped because $r_r/r_0 \to 0$ as t increases..

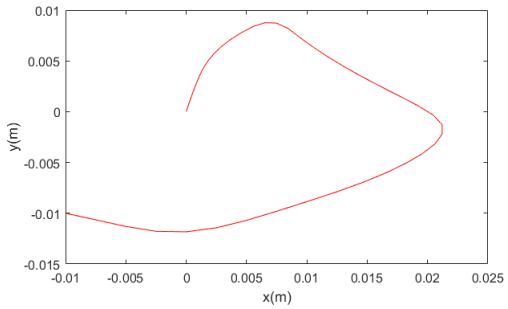

(a) Trajectory of the atom in the x-y plane

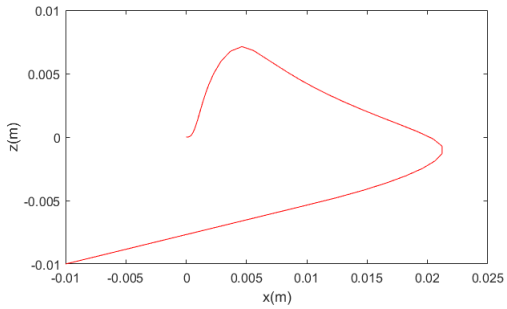

(b) Trajectory of the atom in the x-z plane

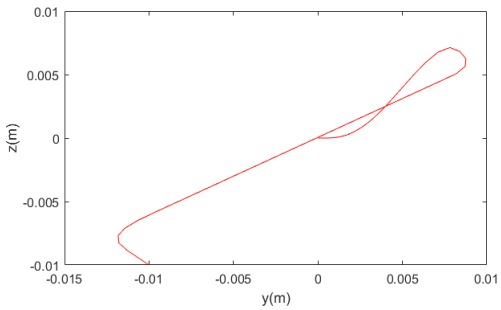

(c) Trajectory of the atom in the y-z plane

Figure 6.4: Trajectories of the atom in three orthogonal planes.

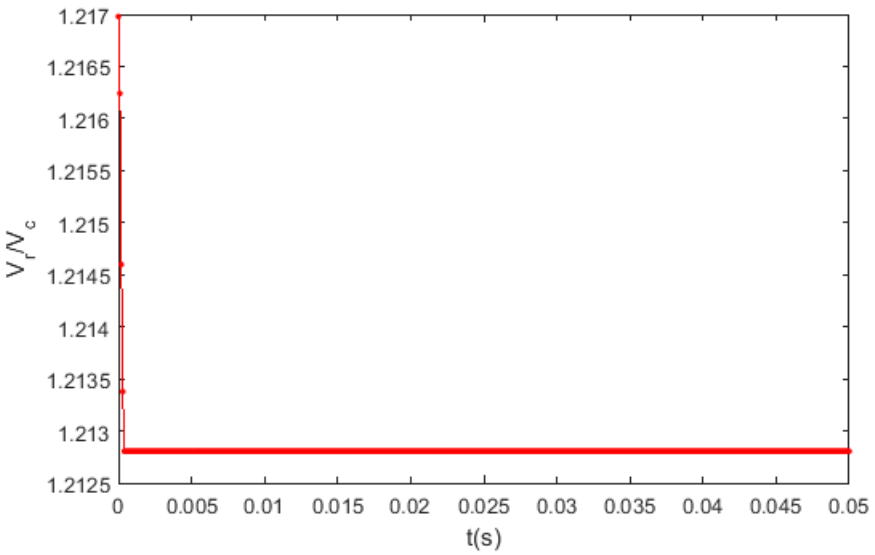

Figure 6.5: Ratio between the radial velocity v_r and the capture velocity v_c calculated as a function of time. The atom starts its motion with a velocity greater than the capture velocity and it is not slowed down at the end of the simulation.

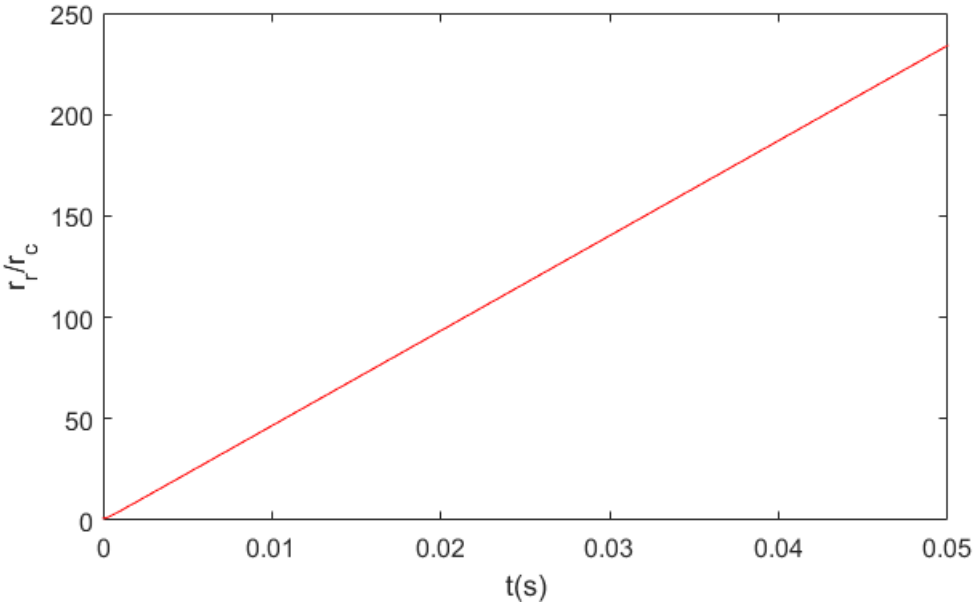

Figure 6.6: Ratio between the radial position r_r and the initial radial position r_0 calculated versus t. The atom is not trapped because r_r/r_0 does not approaches zero as t increases.

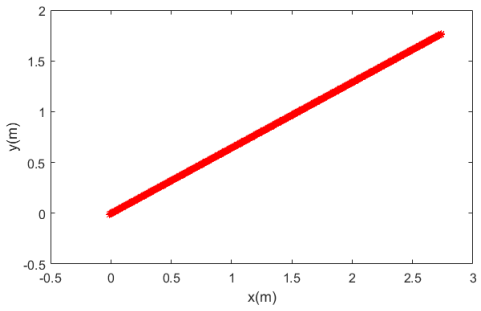

(a) Trajectory of the atom in the x-y plane

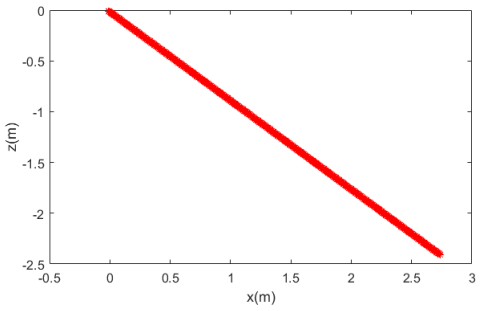

(b) Trajectory of the atom in the x-z plane

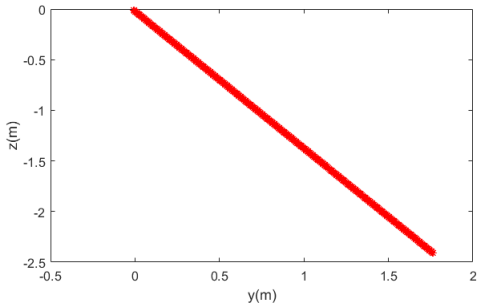

(c) Trajectory of the atom in the y-z plane

Figure 6.7: Trajectories of the atom in three orthogonal planes.

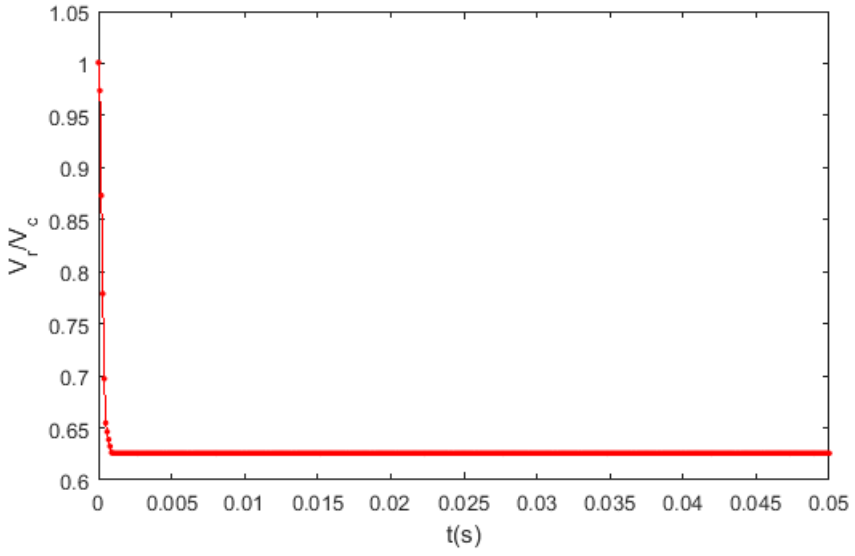

Figure 6.8: Ratio between the radial velocity v_r and the capture velocity v_c calculated as a function of time. The atom starts its motion with a velocity equals the capture velocity and it is slowed down without approaching zero at the end of the simulation.

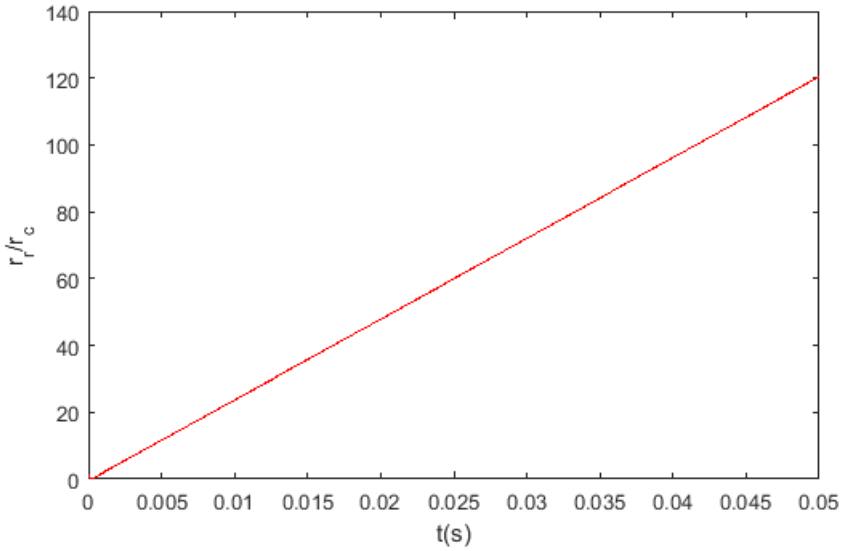

Figure 6.9: Ratio between the radial position r_r and the initial radial position r_0 calculated versus t. The atom is not trapped.

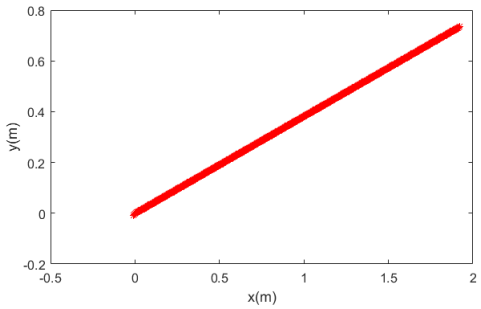

(a) Trajectory of the atom in the x-y plane

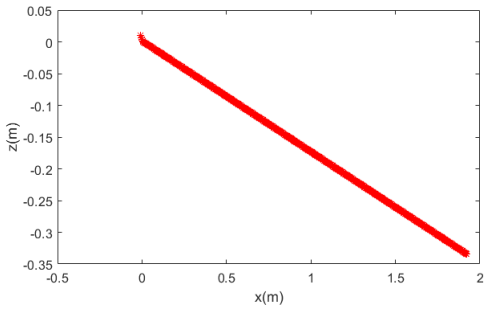

(b) Trajectory of the atom in the x-z plane

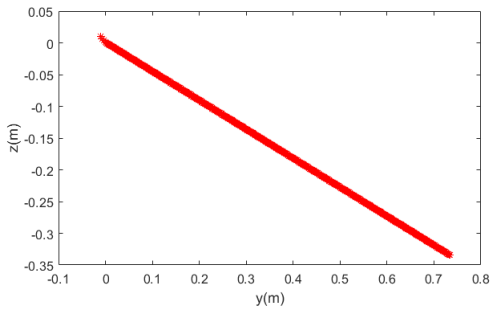

(c) Trajectory of the atom in the y-z plane

Figure 6.10: Trajectories of the atom in three othogonal planes.

The above examples of some of the results obtained with this simulation, show that the expression for the force on each atom, used to model the atomic dynamic within the MOT, properly represents typical dynamics of the atoms. Moreover, some important parameters are included in the force that can be modified into more realistic simulations. The next steps, therefore, would be dedicated not only to the integration of other effects in the simulation (dipole force, diffusion, atom loading and loss), but also to the formulation of an objective function that can describe the performance of the MOT. The objective function will allow the definition of optimal parameters such as the laser beam sizes, positioning, detunings and magnetic field gradients. This, together with the optimisation method for the magnetic trap described in the previous chapter, would represent a powerful tool for the optimisation and miniaturisation of magneto-optical traps.

6.4 Summary

This chapter has described:

- The expression of the total force acting on a multi-level atom in a tridimensional MOT.
- The implementation of the model to solve the equations of motion of Rubidium atoms in a 3D MOT.
- The results obtained for three atoms having different initial velocities and positions.

The first section was necessary to introduce a version of the force, used in the simulation, that treats the atoms as multi-level systems and considers other realistic effects, such as the Gaussian profile of the laser beams and the angle between the direction of the magnetic field and the direction of the light. Great importance is given to the discussion of some results obtained by the Matlab simulations to highlight that the use of this expression of the force provides the expected behaviours for the motion of the atoms in the 3D MOT. Therefore, it is described how this analysis could be extended and result, in the future, in the definition of an objective function to optimise the performances of the MOT.

Chapter 7

Conclusion and outlook

This study has shown that optimisation methods can be useful not only for miniaturising components of a new generation of quantum sensors, but also for more effective gravity data collection acquisition schemes that could exploit the inherent stability of a quantum gravimeter.

In particular, in the first part of the thesis, a novel acquisition scheme, based on the content of the horizontal gravity gradients, has been proposed. This "optimised grid" of 397 points has been proved to provide a better resolution than a regular grid having a higher number of measurement points (441 points). The better performance has been verified through the analysis and comparison of the model resolution matrices. Moreover, two different methods of construction of the resolution matrix have been presented and compared for the particular inversion performed. This simulation study, although applicable in conjunction with any kind of gravity sensor, opens the possibility for future implementations of "on-field" optimised grids if used with quantum gravimeters and quantum gradiometers that won't require drift corrections. This will become possible when techniques for an "on-field" terrain corrections are addressed.

In the second part of the thesis the research focused on the optimisation of components of quantum sensors: the magnetic trap and the magneto-optical trap. In particular, Chapter 5 presents the work done with the Comsol multiphysics software on the design of a multi-coil magnetic trap. The geometrical parameters used for the design and the analysis of the currents flowing in each coil, have been inferred from an optimisation method based on the minimisation of an objective function. The use of Comsol has allowed verification of the accuracy of the magnetic profile obtained through the inversion method and, at the same time, provided an insight into the temperature, heating, and stress response of the device. In particular, these latest results have shown coil-based devices can be safely manufactured and used in magnetic traps.

Given the interest in integrating such a magnetic trap with optical access, in order to obtain a magneto-optical trap to simultaneously trap and cool atoms, the last part of the study has focused on the numerical simulation of a 3D MOT. In particular, in Chapter 6, it was shown that a more complicated expression for the force acting on an atom in an MOT (which takes into account the multiple level of the atoms and the Gaussian profile of the beams) can be used correctly to predict the dynamic

of atoms in magneto-optical traps. Three examples of atom orbits were shown and their radial velocities, positions and trajectories on different planes were analysed. The force on the atoms is not only useful to more realistically describe what is happening to atoms in a 3D MOT, but also includes some parameters that can be used in future for optimisation of 3D MOTs. In particular, a new objective function including the angle of the lasers, and the profile of the laser beams, can be defined to optimise the entire magneto-optical trap. Therefore, the future perspectives are to integrate in the simulation other realistic effects such as: diffusion, atom loss and loading processes and defining an objective function for the optimisation of the whole 3D MOT.

Appendix A

Rubidium 87 D2 line data

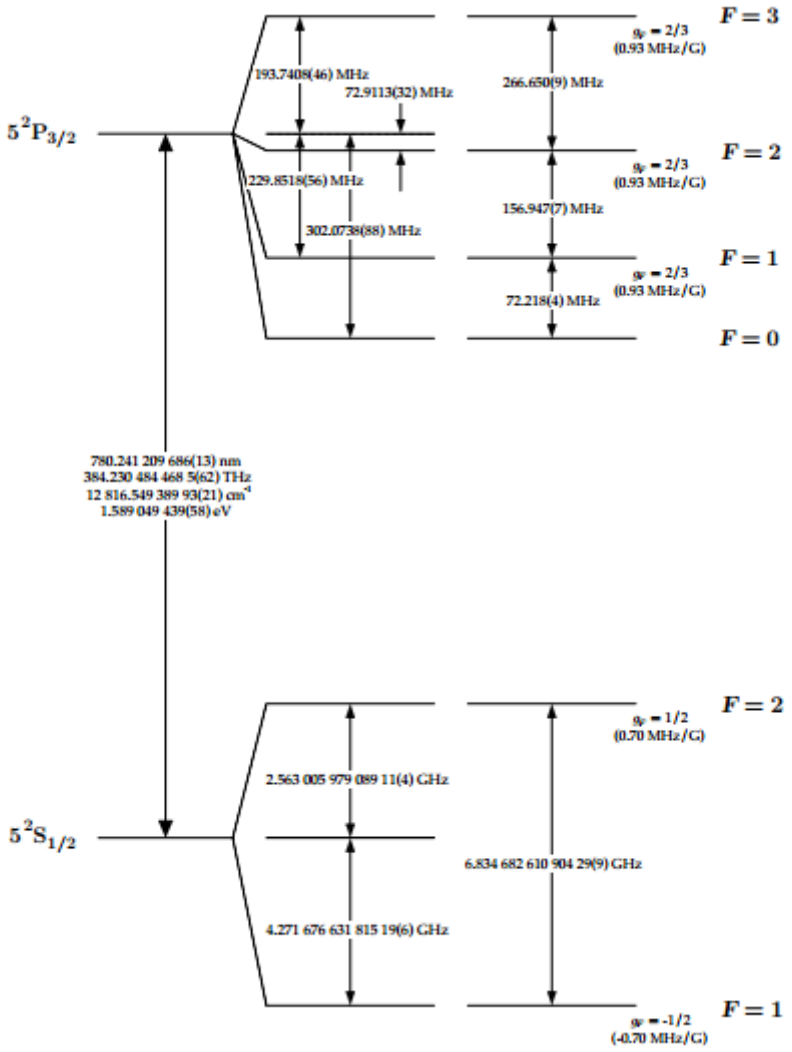

Figure 7.1: ^{87}Rb D2 transition hyperfine structure, with frequency splittings between the hyperfine energy levels. The approximate Lande g_F -factors for each level are also given, with the corresponding Zeeman splittings between adjacent magnetic sublevels [45]

.

^{87}Rb Data and other parameters	
Speed of light (m/s)	2.997 924 58 $\times 10^{8}$
Planck's constant $\hbar(J \cdot s)$	1.054 571 596(82) $\times 10^{-34}$
Bohr magneton μ_B (J/T)	9.274 008 99(37) $\times 10^{-24}$
Boltzmann's constant k_B (J/K)	1.380 650 3(24) $\times 10^{-23}$
Atomic mass (Kg)	1.443 160 60(11) $\times 10^{-25}$
Natural line width γ (MHz)	$2\pi \cdot 6.065(9)$
Detuning δ (MHz)	$-3 \cdot \gamma$
Doppler temperature (μK)	146
Saturation intensity (D_2 line, π-polarized light) (mW/cm^2)	2.503(3)
Saturation intensity ($\sigma^{\pm}$-polarized light)(mW/cm^2)	1.669(2)

Table 7.1: ^{87}Rb Data and other parameters used in the simulation(from [45])

Bibliography

[1] A.S. Murray and R.M. Tracey. *Best practice in gravity surveying*. 2001.

[2] C.D.F. Rogers N. Metje D.N. Chapman and K. Bongs. "Seeing through the ground: the potential of gravity gradient as a complementary technology". In: *Advances in civil engineering* 2011.1 (2011), p. 9.

[3] Richard J. Blakely. *Potential theory in Gravity and Magnetic applications*. 1995.

[4] M.N. Nabighian et al. "Historical development of the gravity method in exploration". In: *GEOPHYSICS* 70.6 (2005), 63ND–89ND.

[5] D. Kaputa D. Di Francesco A. Grierson and T. Meyer. "Gravity gradiometer systems- advances and challenges". In: *Geophysical Prospecting [Proceeding Paper]* 57.4 (2009), pp. 615–623.

[6] C. Huygens. *Horologium oscillatorium sivae de motu pendulorum ad horologia aptato demonstationes geometricae*. 1673.

[7] H. Kater. "An account of experiments for determining the length of the pendulum vibrating seconds in the latitude of London". In: *Philosophical transactions of the Royal Society of London* 108.? (1818), pp. 33–102.

[8] Micro g LaCoste. *FG5 Absolute gravimeter user's manual*. 2006.

[9] K. Y. Chung A. Peters and S. Chu. "High-precision gravity measurements using atom interferometry". In: *Metrologia* 38.1 (2001), p. 25.

[10] M. Kasevich and S. Chu. "Atomic interferometry using stimulated Raman transitions". In: *Phys. Rev. Lett* 67 (1991), pp. 181–184.

[11] M. Kasevich K. Moler D.S. Weiss and S. Chu. "Theoretical analysis of velocity-selective Raman tranisitions". In: *Phys. Rev. A* 45 (1992), pp. 342–348.

[12] B.C. Young D.S. Weiss and S. Chu. "Precision measurment of $\hbar/mc_s$ based on photon recoil using laser-cooled atoms and atomic interferometry". In: *Appl. Phys. B* 59 (1994), pp. 217–256.

[13] K. Y. Chung A. Peters and S. Chu. "Measurement of gravitational acceleration by dropping atoms". In: *Nature* 400.6747 (2005), pp. 849–852.

[14] D.A.G. Nowell. "Gravity terrain corrections-an overview". In: *Journal of Applied Geophysics* 42 (1999), pp. 117–134.

[15] I.M. Longman. "Formulas for computing the tidal accelerations due to the moon and the sun". In: *Journal of Geophysical research* 64 (1959), pp. 2351–2355.

[16] D.T. Thompson. "EULDPH – a new technique for making computer-assisted depth estimates from magnetic data". In: *Geophysics* 47 (1982), pp. 31–37.

[17] H. Granser A.J. Millet A. Reid J.M. Allsop and I.W. Somerton. "Magnetic interpretation in three dimensions using Euler deconvolution". In: *Geophysics* 55 (1990), pp. 80–91.

[18] William Menke. *Geophysical data analysis: discrete inverse theory*. 1984.

[19] D.W. Oldenburg and Y.Li. *Inversion for applied geophysics: a tutorial*.

[20] J.E. Chambers O.Kuras P.B. Wilkinson P.I. Meldrum and R.D. Ogilvy. "Improved strategies for the automatic selection of optimized sets of Electrical Resistivity Tomography measurement configurations". In: *Geophysics Journal Internetional* 167 (2006), pp. 1119–1126.

[21] G.A. Oldenborger and P.S. Routh. "The point-spread function measure of resolution for the 3-D electrical resistivity experiment". In: *Geophysics Journal International* 176 (2007), pp. 405–414.

[22] M. Roach. "Optimised gravity survey design". In: *Melbourne convention and exhibition centre; GSA 18th Australian*. 2006, pp. 1–3.

[23] A.B. Reid. "Aeromagnetic survey design". In: *Geophysics* 63 (1980), pp. 109–119.

[24] R.A. Krahenbuhl K. Davis M.A. Kass and Y. Li. "Survey design and model appraisal based on resolution analysis for 4D gravity monitoring". In: *SEG Technical Program Expanded Abstract* (2008), pp. 731–735.

[25] *GA program library for forward modelling and inversion of gravity data over 3D structures version 5.0*. 2008.

[26] G. Papp D. Nagy and J. Benedek. "The gravitational potential and its derivatives for the prism". In: *Journal of Geodesy* 74 (2000), pp. 552–560.

[27] Y. Li and D.W. Oldenburg. "3-D inversion of magnetic data". In: *Geophysics* 2 (1996), pp. 394–408.

[28] P.H. Calamai and J.J More. "Projected gradient methods for linearly constrained problems". In: *Journal mathematical programming* 39 (1987), pp. 93–116.

[29] B. Kirkendall. "Nonlinear model appraisal in gravity gradiometry imaging, properties and modeling of the resolution matix". PhD thesis. University of British Columbia, 2007.

[30] C.J. Pethick and H.Smith. *Bose-Einstein condensation in dilute gases*. 2002.

[31] Christopher J. Foot. *Atomic Physics*. 2005.

[32] L. Vichi and S. Stringari. "Colletive oscillations of an interacting trapped Fermi gas". In: *Physical Review* 6 (1999), pp. 4734–4737.

[33] H. J. Metcalf and P. van der Straten. *Laser cooling and trapping*. 1999.

[34] W. Mussel. "Characterization of a two-dimensional MOT for 39 K". Diploma thesis. University of Heidelberg, 2011.

[35] S.L. Rolston C.E. Tanner R.N. Watts P.D. Lett W.D. Phillips and C.I. Westbrook. "Optical molasses". In: *Journal of the optical society of America B-Optical Physics* 6 (1989), pp. 2084–2107.

[36] A. Ashkin and J.P. Gordon. “Stability of radiation-pressure particle traps: an optical Earnshaw theorem”. In: *Opt. Letter* 10 (1983), pp. 511–513.

[37] A. Cable S. Chu E.L. Raab M.Prentiss and D.E. Pritchard. “Trapping of neutral sodium atoms with radiation pressure”. In: *Phys. Rev. Lett.* 59 (1987), pp. 2631–2634.

[38] C. Immer J. Simpson J. Lane and R. Youngquist. *Simple analytic expressions for the magnetic field of a circular current loop*. Tech. rep. NASA technical documents, 2001.

[39] F. Ramires-Martinez. “Integration of optical components and magnetic field sources in atom chips”. PhD thesis. Imperial College London, 2008.

[40] M. Stephens K. Lindquist and C. Wieman. “Experimental and theoretical study of the vapor-cell Zeeman optical trap”. In: *Physical review* 46.7 (1992), pp. 4082–4090.

[41] YT. Chough and W. Jhe. “A computational analysis of an axiconic magneto-optical trap”. In: *Journal of the Physical society of Japan* 69.5 (2000), pp. 1366–1373.

[42] M. Chowdhury A.M. Steane and C.J. Foot. “Radiation force in the magneto-optical trap”. In: *Journal of the optical society of America B-Optical Physics* 9.12 (1992), pp. 2142–2158.

[43] H.R. Noh W. Jhe J.A. Kim K.I. Lee and M. Ohtsu. “Atom trap in an axicon mirror”. In: *Optics letters* 22 (1997), pp. 117–119.

[44] E. Fehlberg. *Low-order classical Runge Kutta formulas with stepsize control and their application to some heat transfer problems*. Tech. rep. NASA technical reports, 1969.

[45] D.A. Steck. *Rubidium 87 D Line Data*. 2003.